Micromechanical Testing of Irradiated Tungsten for Fusion



Bethany Jim

Linacre College

University of Oxford

Supervisors: Prof David Armstrong, Prof Angus Wilkinson,
Prof Ed Tarleton and Dr Chris Hardie

A thesis submitted for the degree of
Doctor of Philosophy
Michaelmas 2023

Abstract

Tungsten is a leading candidate for plasma-facing components (PFCs) in fusion reactors owing to its excellent thermomechanical properties. During operation, PFCs are subjected to neutron irradiation, high temperatures and high strain rates, causing changes to material performance. This study investigated the effect of strain rate (SR) and radiation damage through micromechanical testing of [001]-orientated unirradiated single crystal W and single crystal W irradiated to 1.67 dpa at 900 °C.

Constant strain rate spherical nanoindentation experiments using 5 µm and 10 µm radius tips were executed at $3.2x10^{-3}$ s^{-1}, $3.2x10^{-4}$ s^{-1} and $3.2x10^{-5}$ s^{-1} to produce indentation stress-strain curves. The unirradiated sample showed an absence of work hardening and large pop-ins due to the lack of defects present. An increase in hardening and yield stress was seen after irradiation; the irradiated sample also exhibited significant work hardening behaviour, which can be attributed to radiation-induced microstructural barriers to dislocation motion such as Re-Os precipitates, dislocations and voids. Work hardening behaviour remained consistent across the strain rates.

Characterisation of the pile-up, strain localisation and density of geometrically necessary dislocations around the nanoindents revealed an increase in pile-up height after irradiation and indicated the presence of a constrained plastic zone due to radiation-induced defects, causing increased material flow towards the surface. Due to challenges in the rate-controlled nanoindentation method, total indenter displacement, and thus total strain, unintentionally increased with SR. Pile-up height normalised by residual indentation depth was found to increase with SR, but further refinement of the method would allow a more reliable method of characterising deformation behaviour.

Crystal plasticity finite element modelling using a set of parameters fitted to the experimental results successfully captured the radiation-induced increase in pile-up height and constraint of the plastic zone with remarkable agreement, and provided clarity on the subtle rate effects exhibited.

This work reinforces the ability to study material performance in a fusion environment through micromechanical testing methods. Furthermore, consistency in the radiation-induced hardening and deformation behaviour observed in this study and self-ion irradiated W gives credence to ion irradiation in emulating neutron-irradiation effects, despite producing different damage mechanisms.

Acknowledgements

The research in this thesis was conducted at the University of Oxford as part of the Fusion CDT programme (EPSRC Centre for Doctoral Training in the Science and Technology of Fusion Energy).

Part of the experiments were performed at UKAEA's Materials Research Facility, which has been funded by and is part of the UK's National Nuclear User Facility and Henry Royce Institute for Advanced Materials.

***

Firstly, I would like to thank my supervisors Dave Armstrong, Angus Wilkinson, Ed Tarleton and Chris Hardie for their continued support, guidance and insights over the course of this project.

I would also like to thank Suchandrima Das, Eralp Demir, Jack Haley, Phani Karamched, Anna Kareer, Matthew Lloyd, Bo-Shiuan Li, and the team at CCFE for their respective contributions and support to my training, experiments, and computational modelling.

I am also sincerely thankful to my friends at Walton Street, Linacre College, and the Department of Materials for providing me with a rich and memorable experience at Oxford.

Last but not least, I would like to extend a special thank you to Arutyun for his endless support and understanding in my attempt to find balance between writing and work. I am also deeply grateful to my parents, Timmy, Lydia, my wider family, and my friends for their unwavering support and encouragement throughout this journey.

Glossary of Abbreviations

AFM	Atomic force microscopy
BCC	Body-centred cubic
CPFE	Crystal plasticity finite element
CRSS	Critical resolved shear stress
DPA	Displacement per atom
EBSD	Electron backscatter diffraction
FEM	Finite element modelling
GNDs	Geometrically necessary dislocations
HR-EBSD	High resolution electron backscatter diffraction
ISE	Indentation size effect
ISS	Indentation stress-strain
PFC	Plasma-facing component
SEM	Scanning electron microscopy
SRS	Strain rate sensitivity
SSDs	Statistically stored dislocations
YS	Yield stress

Contents

1 Introduction 13

2 Literature Review 15

2.1 Nuclear Fusion 15

2.1.1 The D-T Fusion Reaction 15

2.1.2 Reactor Design 15

2.2 Materials for Nuclear Fusion 17

2.2.1 Materials Selection 17

2.2.2 Tungsten for Fusion 17

2.2.3 Radiation Damage Effects in Tungsten 19

2.2.3.1 Transmutation 19

2.2.3.2 Cascades 20

2.2.3.3 Microstructural Defects 21

2.2.4 Irradiation Experiments 21

2.2.5 The Role of Micromechanical Testing 22

2.3 Nanoindentation 23

2.3.1 Developments in Nanoindentation 24

2.3.2 Pile-Up and Sink-In 26

2.3.3 Berkovich Indentation 27

2.3.4 Spherical Indentation 28

2.4 Strain Rate Sensitivity 30

2.4.1 Deformation of Body-Centred Cubic Materials 30

2.4.2 Strain Rate Sensitivity and Activation Volume 31

2.4.3 Nanoindentation Strain-Rate Jump Tests 33

2.4.4 Constant Strain Rate Tests using Spherical Nanoindentation 34

2.4.5 Effect of Composition and Radiation on Strain Rate Sensitivity 35

2.5 Studying Indentation using Computational Modelling 36

2.5.1 Crystal Plasticity Finite Element Modelling 36

2.5.2 Studying Deformation Behaviour 36

2.6 Summary and Aims 39

3 Experimental Methods 41

3.1 Materials and Sample Preparation 41

3.2 Neutron Irradiation 41
3.3 Berkovich Nanoindentation 42
3.3.1 Background Theory 42
3.3.2 Nanoindentation Procedure 43
3.4 Spherical Nanoindentation 44
3.4.1 Background Theory 44
3.4.2 Nanoindentation Procedure 46
3.5 Atomic Force Microscopy 46
3.6 Scanning Electron Microscopy 49
3.7 High Resolution Electron Backscatter Diffraction 49
4 Investigating Strain Rate Effects in Neutron-Irradiated Tungsten 52
4.1 Berkovich Nanoindentation 52
4.2 Spherical Nanoindentation 56
4.2.1 Tip Calibration 56
4.2.2 Zero Point Correction 56
4.2.3 5 µm Tip 57
4.2.4 10 µm Tip 65
4.3 Discussion 70
4.3.1 Effect of Strain Rate 73
4.3.2 Effect of Irradiation 77
4.3.3 Effect of Tip Size 83
4.4 Summary 86
5 Characterising Deformation Behaviour in Neutron-Irradiated Tungsten 89
5.1 Indentation Morphology 89
5.1.1 5 µm Indent Surface Profiles 90
5.1.2 10 µm Indent Surface Profiles 95
5.1.3 Pile-up Volume 98
5.2 Characterisation of Deformation Structures 102
5.2.1 SEM 102
5.2.2 HR-EBSD 102
5.3 Discussion 106

5.3.1 Pile-up Morphology 106
5.3.2 Effect of Irradiation and Strain Rate 107
5.4 Summary 111
6 CPFE Modelling of Irradiation Effects in Tungsten 113
6.1 CPFE Modelling 114
6.1.1 Simulation Set-up 114
6.1.2 CPFE Model 116
6.1.3 Mesh Convergence 121
6.2 Nanoindentation Method Pile-Up Artifact 121
6.3 CPFE Results 123
6.3.1 Load-Displacement Curves 123
6.3.2 Indentation Surface Morphology 125
6.3.3 Elastic Strain Fields 127
6.3.4 GND Density 128
6.4 Discussion 131
6.5 Summary 134
7 Summary, Conclusions and Future Work 136
7.1 Spherical Indentation Stress-Strain Behaviour 136
7.2 Deformation Mechanisms 139
7.3 Validation of Results by CPFE Modelling 142
7.4 Conclusions 144
7.5 Future Work 145
References 147

List of Figures

Figure 2.1: Poloidal cross-section of a tokamak showing plasma-facing components in the vacuum vessel of ITER.[13] 16

Figure 2.2: Evolution of a displacement cascade in tungsten from a 200 keV PKA up to 300 fs after collision (left), showing recoils with E_{kin} >10 eV, and after 40 ps (right), showing remaining vacancies and interstitials.[27] 20

Figure 2.3: Schematic of load versus displacement data for an indentation experiment.[34] The quantities shown are P_{max}: the peak indentation load; h_{max}: the indenter displacement at peak load; h_f: the final depth of the contact impression after unloading; and S: the initial unloading stiffness. . 24

Figure 2.4: Schematic drawing of pile-up and sink-in reproduced from McCann & Corcoran.[136] The top half of the figure illustrates the cross-section of the indenter at maximum load. The bottom half shows the projected area of contact based upon displacement is overestimated in the sink-in case, and underestimated for the pile-up case. 27

Figure 2.5: Nanoindentation strain-rate jump test with three different applied strain rates. Graph shows the applied indentation strain rate ($\dot{P}/P$) and corresponding strain rate versus indentation depth.[74] 34

Figure 3.1: Schematic drawing of G200 nanoindenter. 44

Figure 3.2: Example of the background removed through a polynomial fit in the Gwyddion.[92] 48

Figure 3.3: Example of a typical AFM micrograph for an indent, showing asymmetry in the four lobes surrounding the indenter pit. Lines 1 and 2 denote the two directions in which line profiles were extracted from. 48

Figure 3.4: Line profiles corresponding to the directions shown in Figure 3.3. 49

Figure 3.5: A schematic of a typical EBSD setup with detector and sample. 51

Figure 4.1: Average load versus displacement into surface curves for Berkovich indentation in SX and NISX. Error bars show ± 1 standard deviation. 54

Figure 4.2: Typical load–displacement data for SX and NISX; the black arrow indicates the pop-in event which took place in the unirradiated sample. 54

Figure 4.3: Average hardness–displacement curves for SX and NISX. Error bars show ± 1 standard deviation. 55

Figure 4.4: Average modulus–displacement curves for SX and NISX. Error bars show ± 1 standard deviation. 55

Figure 4.5: (a) Typical load-displacement curves for unirradiated and neutron-irradiated single crystal tungsten at a strain rate of 3.2×10^{-4} s^{-1}. The graph in (b) shows a magnified view of the initial data. 58

Figure 4.6: Graph of contact radius (CSM signal) vs displacement in both samples at 3.2 x 10^{-4} s^{-1}. ..59

Figure 4.7: Spherical indentation stress-strain curves with a 5 µm radius indenter in unirradiated single crystal tungsten (a, c, e) and neutron-irradiated single crystal tungsten (b, d, f) at strain rates of 3.2 x 10^{-3} s^{-1}, 3.2 x 10^{-4} s^{-1} and 3.2 x 10^{-5} s^{-1} respectively. Graphs (g) and (h) show a comparison of typical stress-strain curves at varying strain rates in both materials. 62

Figure 4.8: Average yield stresses from Table 4.2 extracted from the ISS curves in Figure 4.6 using the three yield stress analysis methods. Average values were calculated from between 4 – 9 successful indents as shown in Figure 4.7. Error bars show ± 1 standard deviation. 63

Figure 4.9: (a) Typical load-displacement curves for unirradiated single crystal tungsten and neutron-irradiated single crystal tungsten at a strain rate of 3.2 x 10^{-4} s^{-1}. The graph in (b) shows a magnified view; in the unirradiated sample, a large pop-in followed by small pop-in events, whilst an artifact in machine control can be observed in the irradiated sample prior to a series of small pop-ins. 65

Figure 4.10: Spherical indentation stress-strain curves with a 10 µm radius indenter in unirradiated single crystal tungsten (a, c, e) and neutron-irradiated single crystal tungsten (b, d, f) at strain rates of of 3.2 x 10^{-3} s^{-1}, 3.2 x 10^{-4} s^{-1} and 3.2 x 10^{-5} s^{-1} respectively. Graphs (g) and (h) show a comparison of typical stress-strain curves at varying strain rates in both materials. 68

Figure 4.11: Average yield stresses from Table 4.3 (extracted from the ISS curves in Figure 4.10 using the three yield stress analysis methods detailed in Section 4.2.3). Average values were calculated from between 4 – 7 successful indents as shown in Figure 4.10. Error bars show ± 1 standard deviation. 69

Figure 4.12: Graph of hardness vs indentation strain rate (on a log scale) for both 5 µm and 10 µm radius spherical indents in unirradiated single crystal tungsten (SX) and neutron-irradiated single crystal tungsten (NISX) at 3.2 x 10^{-3} s^{-1}, 3.2 x 10^{-4} s^{-1} and 3.2 x 10^{-5} s^{-1}. Hardness values were calculated at 0.08 strain for comparison with the constant strain of ~ 8 % during Berkovich nanoindentation. Average values were calculated from between 4 – 9 successful indents as shown in Figure 4.7 and Figure 4.10. Error bars show ± 1 standard deviation. 76

Figure 4.13: Graph of log hardness vs log strain for 5 µm and 10 µm radius spherical tip indents in SX and NISX at strain rates of 3.2 x 10^{-3} s^{-1}, 3.2 x 10^{-4} s^{-1} and 3.2 x 10^{-5} s^{-1}. m is the strain-rate sensitivity. 76

Figure 4.14: Spherical stress-strain curves for unirradiated single crystal tungsten and neutron-irradiated single crystal tungsten tested with 5 µm tip and 10 µm tips at strain rates of 3.2 x 10^{-4} s^{-1}. 80

Figure 4.15: Re and Os atom maps from APT reconstructions of the neutron-irradiated tungsten sample, showing Re atoms as red spheres of radius 0.1 nm and Os atoms as green spheres of 0.1 nm.[96] 82

Figure 4.16: Stress-strain curves from four cantilever beams tested in another neutron-irradiated tungsten sample from the same Extremat-II campaign, calculated using simple beam theory. Beams 2B and 3A fractured (marked with an X) whilst the other two tests were stopped early (marked with an O). The curves for the fractured beams show a significant degree of plastic deformation before fracture occurred.[97] 82

Figure 4.17: Graph of contact radius (CSM signal) vs indentation strain for 5 μm and 10 μm tips in SX and NISX at a strain rate of 3.2 x 10^{-4} s^{-1}. 85

Figure 5.1: AFM micrographs of spherical indents performed with a 5 μm radius indenter in unirradiated single crystal tungsten **(a, c, e)** and neutron-irradiated tungsten **(b, d, f)** at strain rates of 3.2 x 10^{-3} s^{-1}, 3.2 x 10^{-4} s^{-1} and 3.2 x 10^{-5} s^{-1} respectively. The arrow on **(a)** shows the direction of the line profile extraction. 93

Figure 5.2: (a) AFM line profiles of spherical indents performed with a 5 μm radius indenter in SX and NISX at strain rates of 3.2 x 10^{-3} s^{-1}, 3.2 x 10^{-4} s^{-1} and 3.2 x 10^{-5} s^{-1} respectively. **(b)** Magnified view of the pile-up region in the line profiles. **(c)** Normalised AFM height as a percentage of maximum residual indentation depth. **(d)** Magnified view of the pile-up region of the normalised height profiles. 94

Figure 5.3: AFM micrographs of an indent measured at 3.2 x 10^{-3} s^{-1} in **(a)** unirradiated single crystal tungsten and **(b)** and neutron-irradiated single crystal tungsten. 95

Figure 5.4: AFM micrographs of spherical indents performed with a 10 μm radius indenter in unirradiated single crystal tungsten **(a, c, e)** and neutron-irradiated single crystal tungsten **(b, d, f)** at strain rates of 3.2 x 10^{-3} s^{-1}, 3.2 x 10^{-4} s^{-1} and 3.2 x 10^{-5} s^{-1} respectively. Both samples were indented in the [001] orientation..... 96

Figure 5.5: (a) AFM line profiles of spherical indents performed with a 10 μm radius indenter in SX and NISX at strain rates of 3.2 x 10^{-3} s^{-1}, 3.2 x 10^{-4} s^{-1} and 3.2 x 10^{-5} s^{-1} respectively. **(b)** Magnified view of the pile-up region in the line profiles. **(c)** Normalised AFM height as a percentage of maximum residual indentation depth. **(d)** Magnified view of the pile-up region of the normalised height profiles. 97

Figure 5.6: Example of the 3D visual output produced by the script for calculating the volume above and below the surface, representing the volume of the pile-up and indenter trough respectively. The inner and outer boundaries of the pile-up zone denote the area in which pile-up is assumed to occur. In this example, the outer boundary of the pile-up zone is defined as the point at which the volume decreases by 2 % of the volume measured at the inner boundary. The data used for all volume calculations is contained within the radius of the black circle. 99

Figure 5.7: Example of the increased pile-up zone when the outer boundary of the pile-up zone is defined as the point at which the volume decreases by 12 % of the volume measured at the inner boundary instead of 2 %. 100

Figure 5.8: Graph showing the ratio of the volume above the surface to the volume below the surface as a consistent means of comparing the quantity of pile-up with respect to indentation depth for each strain rate in both the SX and NISX samples..... 100

Figure 5.9: SEM micrographs of 5 μm spherical indents at 3.2 x 10^{-4} s^{-1} in **(a)** SX and **(b)** NISX, where the black arrows indicate the presence of slip bands..... 102

Figure 5.10: Total GND density (ρ) maps in the XY plane for indents performed with a 5 μm tip in **(a, c, e)** SX and **(b, d)** NISX. Colour scale units are in logρ with ρ in m^{-2}. Scale bars correspond to 5 μm. 103

Figure 5.11: ωxy lattice rotation fields about [001] for 5 μm tip indents in **(a, c, e)** SX and **(b, d)** NISX at varying strain rates. Lattice rotations are plotted in radians and scale bars correspond to 5 μm. 103

Figure 5.12: Elastic strains maps for indents performed with a 5 μm tip in **(a, c, e)** SX and **(b, d, f)** NISX at varying strain rates. Both samples were indented in the [001] orientation. Scale bars correspond to 5 μm. 104

Figure 6.1: CPFE mesh representing one quarter of the model created in Abaqus to simulation spherical nanoindentation of a tungsten cube with a 3.7 μm radius spherical indenter. 115

Figure 6.2: CPFE predictions of height profile data for spherical indents performed in the [001] orientation with a nominally 5 μm radius indenter at (a) fast and (b) medium strain rates, to the same indentation depth of 430 nm. 122

Figure 6.3: Load-displacement curves predicted by CPFE simulations for spherical nanoindentation at fast and medium strain rates to the same indentation depth of 430 nm. 123

Figure 6.4: Load-displacement curves for SX and NISX samples obtained from spherical nanoindentation and CPFE simulations at fast and medium strain rates. 124

Figure 6.5: Surface profiles for spherical indents performed with a nominally 5 μm radius indenter at fast and medium strain rates alongside surface height predictions from CPFE calculations. AFM micrographs of indents at fast and medium strain rates are shown respectively for SX in (a) and (c), and for NISX in (b) and (d). CPFE predictions of surface height at fast and medium strain rates are shown respectively for SX in (e) and (g), and for NISX in (f) and (h). 126

Figure 6.6: εxy component of the residual deviatoric lattice strain in the XY plane (sample surface) determined by HR-EBSD for indents performed with a nominally 5 μm radius indenter at fast and medium strain for SX in (a) and (c), and for NISX in (b) and (d). Elastic strain predictions from CPFE calculations at fast and medium strain rates are shown respectively for SX in (e) and (g), and for NISX in (f) and (h). Both samples were indented in the [001] orientation. Scale bars correspond to 5 μm. 129

Figure 6.7: Total GND density (ρGND) maps determined by HR-EBSD in the XY plane for indents performed with a nominally 5 μm radius indenter at fast and medium strain rates respectively for SX in (a) and (c), and for NISX in (b) and (d). Predictions from CPFE calculations at fast and medium strain rates are shown respectively for SX in (e) and (g), and for NISX in (f) and (h). Colour scale units are in $\log\rho GND$ with ρGND in m^{-2}. Scale bars correspond to 5 μm. 130

List of Tables

Table 2.1: Elemental composition of tungsten after five years in ITER, where appm is atomic parts per million.[23] 19

Table 2.2: Advantages of micromechanical testing on neutron- and ion-irradiated fusion materials.[31] 22

Table 4.1: Hardness values for both SX and NISX at slow, medium and fast strain rates calculated at a strain of 8 % strain for comparison with Berkovich nanoindentation. 60

Table 4.2: Yield stress data from indentation stress-strain curves conducted with a 5 µm radius spherical tip at different strain rates, calculated using the three methods described in Section 4.2.3. 63

Table 4.3: Yield stress data from indentation stress-strain curves conducted with a 10 µm radius spherical tip at different strain rates, calculated using the three methods described in Section 4.2.3. 69

Table 4.4: Hardness values for both SX and NISX at slow, medium and fast strain rates calculated at a strain of 8 % strain for comparison with Berkovich nanoindentation. 70

Table 4.5: Spherical nanoindentation strain-rate sensitivity, m, and activation volume, V, calculated for both SX and NISX using 5 µm and 10 µm radius spherical tips for constant strain rate tests. The hardness for each material and tip condition was taken from the medium strain rate of 3.2×10^{-4} s^{-1}. 77

Table 4.6: Maximum indentation stress values from ISS curves for both 5 µm and 10 µm radius spherical tips at 3.2×10^{-4} s^{-1} in unirradiated and neutron-irradiated single crystal tungsten. 80

Table 5.1: AFM height profile data for indents conducted with a 5 µm spherical tip at different strain rates in unirradiated single crystal tungsten (SX) and neutron-irradiated single crystal tungsten (NISX) 92

Table 5.2: AFM height profile data for 10 µm indents at different strain rates in SX and NISX. 98

Table 5.3: Graph of the percentage difference in the ratio of volume above the surface to the volume below in the irradiated tungsten compared to unirradiated for all strain rates. This difference was calculated using the volume data for both tips displayed in Figure 5.8. 101

Table 6.1: Displacement depths from the load-displacement curves of the spherical nanoindentation experiments with a 5 µm radius tip at fast and medium strain rates in both SX and NISX. 116

Table 6.2: Mechanical properties for tungsten from literature and CRSS parameters used for fitting load-displacement, morphological and deformation data obtained from nanoindentation, AFM and HR-EBSD experiments. 119

Table 6.3: Comparison of peak load reached by spherical nanoindentation experiments and CPFE predictions with a 5 µm radius tip at fast and medium strain rates in SX and NISX. 125

Table 6.4: Comparison of maximum pile-up height around spherical indents measured by AFM and predicted by CPFE simulations at fast and medium strain rates in SX and NISX. 127

1 Introduction

Reliable, environmentally sustainable and clean energy is essential to achieve international economic stability and peace.[1] Fulfilling the electricity requirements for our ever-growing population is of particular importance in avoiding an energy crisis, particularly as the United Nations estimates growth from 7 billion people, at present, to 9.3 billion in 2050 and 10.1 billion in 2100.[2] To increase energy reliability and efficiency whilst reducing carbon emissions, it is essential that reliance on diminishing fossil fuels is reduced; the uptake of alternative sources such as nuclear and renewables can allow catastrophic climate change to be avoided.[1]

Nuclear power is an ideal baseload source of affordable, reliable and efficient energy in the decarbonisation of our electricity production, with nuclear fission energy currently accounting for 13% of energy production worldwide.[3,1] Whilst nuclear power in general is exceedingly more efficient than burning fossil fuels, fusion reactions produce a significantly greater energy per unit mass of fuel than fission ones; furthermore, there is no possibility of a meltdown scenario or an uncontrollable chain reaction, meaning evacuation of the surrounding area is not required in the event of an accident. Nuclear fusion can offer a safe, reliable and low-carbon source of energy with short-lived radioactive waste, which must be safely recycled or disposed of within 100 years.

Although nuclear fusion can potentially fulfil our energy demands, there is a need for materials capable of withstanding the extreme temperatures and radiation inside the core of a fusion reactor, particularly in a commercial one proposed for power production such as DEMO (DEMOnstration Power Station).[4] Neutron irradiation can cause damage to the plasma facing components (PFCs) by inducing defects and chemical change, causing a degradation in mechanical properties and a shorter component lifetime. It is important that changes in properties arising from the fusion environment are well understood to correctly predict a material's performance.

Tungsten is a likely candidate for the plasma-facing material in the divertor. Whilst the irradiation response of tungsten has been studied extensively, the transmutation of tungsten into other transition

elements following irradiation is likely to affect the mechanical properties of resulting alloys. The effect of transmutation elements on the strain rate sensitivity and deformation behaviour must therefore be considered. Furthermore, tungsten and its transmutation alloys must be tested at a range of strain rates, given that strain rates of up to 3 s^{-1} for disruptions are expected inside the reactor.[5] It is therefore crucial that the performance of candidate materials such as tungsten under reactor conditions are investigated to advance the adoption of nuclear fusion as an energy source.

2 Literature Review

2.1 Nuclear Fusion

2.1.1 The D-T Fusion Reaction

Nuclear fusion is the joining of two lighter nuclei to create a heavier and more stable nucleus, a process in which a substantial amount of energy is released. The most favourable reaction is the fusing of two hydrogen isotopes, deuterium (D, ^{2}H) and tritium (T, ^{3}H) – "D-T reaction" – because it has the lowest ignition temperature and is the easiest to heat and contain within a magnetic field. Deuterium occurs naturally in seawater, but tritium only exists in trace quantities and thus must be derived from lithium via "breeding" in the reactor blanket. This blanket must also absorb the kinetic energy of neutrons, allowing the heat to be recovered by a coolant (water, helium, PbLi or FLiBe) flowing through the blanket; [6,7] the resultant steam is then able to produce electricity conventionally using turbines and generators in a power plant. To achieve the fusion rates necessary for useful energy production, the fuel temperature must exceed 100 million degrees Celsius, forming a plasma which must be confined to a sufficient density (~ 2 x 10^{20} nuclei/m^3) for particles to collide.[8] A helium nucleus and high-energy neutrons (14.1 MeV) are produced, releasing 17.6 MeV of energy per reaction (Equation 2.1).[9]

$$ {}_{1}^{2}H + {}_{1}^{3}H \rightarrow {}_{2}^{4}He\ (3.5\ MeV) + {}_{0}^{1}n\ (14.1 MeV) \qquad (2.1) $$

Confining the plasma for a time in the order of seconds allows the temperature and density of the system to be maintained, and a net positive production of energy to occur.[10,9] High particle density can be achieved via inertial confinement fusion (ICF) machines, which make use of laser or ion beams, or magnetic confinement fusion (MCF) machines in which the plasma is confined by magnetic fields.[8]

2.1.2 Reactor Design

The most established MCF design is that of the tokamak: a torus-shaped vacuum vessel which uses a toroidal magnetic field and electric current to confine the plasma to the temperature and density

required. Fusion research has thus far focused on notable magnetic configurations, namely: JET (Joint European Torus), in England; ITER (International Thermonuclear Experimental Reactor) – which is currently being built in France; JT-60SA, successor to JT-60U (Japan Torus-60 Upgrade) and the world's largest operational reactor; ASDEX Upgrade and W7-X (Wendelstein 7-X, stellarator) in Germany.

Materials used for plasma facing components (PFCs) are subject to extreme operating conditions. Since they directly face the thermonuclear plasma, their surfaces are exposed to heat flux (5-10 MW/m^2), severe bombardment and intense brehmsstrahlung radiation from high-energy neutrons (14.1 MeV) and charged particles (fuel ions, previously ejected ions from chamber walls, alpha particles or "helium ash").[11,12] The PFCs in the ITER and DEMO vessels will include the divertor and the first wall on each blanket module (Figure 2.1).[13]

The first wall absorbs ejected neutrons from the plasma, allowing their kinetic energy to be transferred to the cooling system in the blanket, whereas the divertor extracts heat and ash waste from the plasma and protects the neighbouring walls. The presence of a divertor allows the formation of a scrape-off layer (SOL) which keeps the plasma away from the vessel walls. The plasma exhaust is extracted from the bulk confined plasma through the separatrix and is transported to the divertor via the SOL. The divertor is therefore subjected to the greatest heat loads in a fusion reactor.[14]

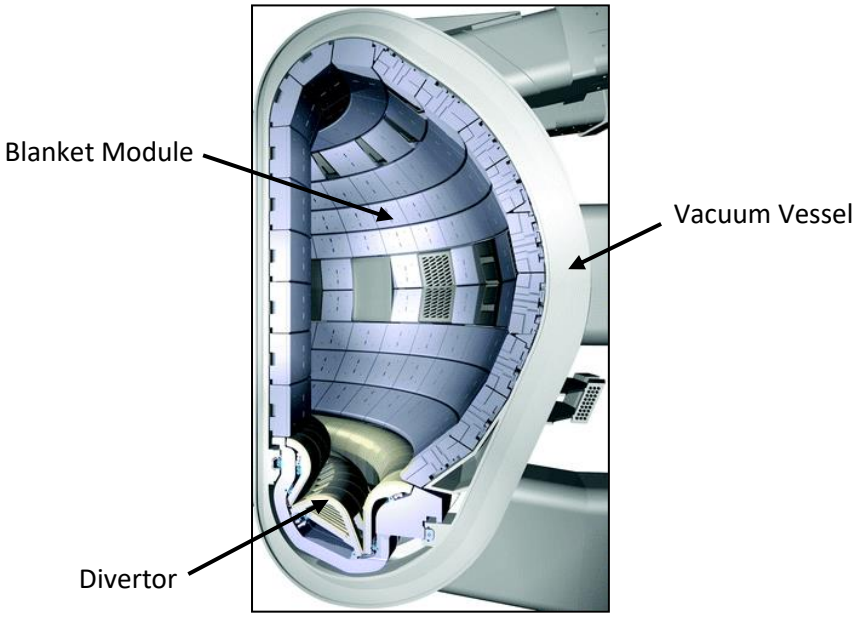


Figure 2.1: *Poloidal cross-section of a tokamak showing plasma-facing components in the vacuum vessel of ITER.*[13]

2.2 Materials for Nuclear Fusion

2.2.1 Materials Selection

The divertor is exposed to operating temperatures of ~1000°C, steady-state heat fluxes of 5-10 MW/m^2, or even greater temperatures during transient fluxes of greater than 20 MW/m^2.[9] Therefore, the divertor material must have a high melting point and high thermal conductivity. To avoid material degradation due to disruptions and heat load variation, PFCs should also be resistant to thermal shock and fatigue and retain high-temperature strength.[15]

Additionally, PFCs are bombarded by 3.5 MeV alpha particles and ejected plasma particles can cause erosion and sputtering. Sputtered particles re-entering the plasma lead to undesired cooling. Arguably, low-Z materials – where Z is atomic number – are preferable since they minimise plasma contamination, whereas the tolerable impurity concentration for high-Z materials in the plasma is much lower, demanding stricter purity control.[15] However, plasma-induced erosion of low-Z materials is much more severe than in their high-Z counterparts, adding another complication to materials selection.[12] Should a high-Z material be used, then it should have a high sputtering energy threshold.[16]

Furthermore, irradiation by 14.1 MeV neutrons can result in radiation-induced precipitation in addition to causing displacement damage and transmutation of the exposed material. These changes can significantly alter the mechanical properties of a component. Thus a low-activation, radiation-resistant material is required.[15]

2.2.2 Tungsten for Fusion

Highly conductive, low-Z carbon fibre composites were tested as a divertor material in JET,[15] but they proved unsuitable owing to chemical erosion under neutron irradiation and high tritium retention, which poses a higher risk in the event of an accident. Contrastingly, tungsten has a high sputtering resistance (E_{th} = 200 eV), low fuel retention, and excellent thermal properties: a high melting

temperature of 3422 °C, exceptional high-temperature strength (~500 MPa at 1000 °C) and high thermal conductivity (~ 150 $Wm^{-1}K^{-1}$). [12]

Tungsten has been successfully used in ASDEX and JET, and has been proposed as the ideal candidate for the divertor in ITER.[17] However, its low fracture toughness (~5 $MPa.m^{0.5}$ at room temperature) and high brittle-to-ductile transition temperature (BDTT)[18] are serious drawbacks which make fabrication of tungsten components challenging. Moreover, neutron irradiation causes the BDTT in tungsten to shift even higher, which is detrimental to the operating temperature window of tungsten.[19] An upper limit is imposed by its recrystallisation temperature (~1300 °C), above which embrittlement occurs.

In the divertor region, tungsten will be subjected to moderately high heat loads (<10 MW/m^2) during steady state operation. However, an increase in heat flux can occur during transient heating events; this includes fluxes of up to 1 GW/m^2 during edge-localised modes (ELMs), lasting for < 1 ms, or up to 3 GW/m^2 for 1 – 10 ms in the event of plasma disruptions, changing the regime of loading to high cycle thermal fatigue.[20,21] These transient plasma events may cause extensive temperature rises and thermal expansion, leading to high strain rates (up to 3 s^{-1} for disruptions and 8 s^{-1} for ELMs). The thermal shock may be severe enough to initiate crack formation and result in failure.[5]

However, tungsten's excellent thermomechanical properties and erosion resistance render it the leading material for both the first wall and divertor in DEMO. A further advantage is its sufficiently low activation, allowing irradiated tungsten to be classed as a complex recycling material within 100 years. It is clear that a greater understanding of the mechanisms controlling the BDTT is needed, in addition to the effect of strain rate on mechanical properties.

One issue with the use of tungsten in a plasma-facing role arises due to the effect of neutron irradiation. Irradiation can cause the chemistry of pure tungsten to change over its lifetime inside the reactor in a phenomenon known as 'transmutation' (described in 2.2.3.1). Furthermore, the thermal

and mechanical properties of the material will also change with irradiation, highlighting the need to study the effect of transmutation on the strain rate sensitivity of tungsten.

2.2.3 Radiation Damage Effects in Tungsten

80% of the fusion energy released by D-T reactions in the plasma is transferred by the 14.1 MeV neutrons (Equation 2.1) to the inner structure of the reactor; when the fluxes of charged and neutral particles impact the PFCs, plasma-material interactions can occur and induce surface and bulk damage.[22,11] Neutrons can cause transmutation of plasma-facing materials in addition to damage cascades which leave the material defect-riddled. These radiation effects can serve to limit the life of PFCs through radiation hardening, creep, void swelling, high-temperature embrittlement, in addition to causing plasma contamination.

Table 2.1: *Elemental composition of tungsten after five years in ITER, where appm is atomic parts per million.*[23]

Element	Concentration (at.%)
Tungsten	94.0
Rhenium	3.8
Osmium	1.4
Tantalum	0.8
Helium	34 appm

2.2.3.1 Transmutation

Transmutation is observed when neutrons are captured by materials in the PFCs, creating transmutation products and leading to helium, hydrogen and other impurities being produced in the bulk of the material.[24,22] Inventory burn up calculations have shown that the main chemical changes in tungsten arise from transmutation into predominantly rhenium, osmium, and tantalum, in addition to producing hydrogen and helium. The transmutation products of 100 at. % tungsten after 5 years in ITER, an experimental device, are shown in Table 2.1, with pure tungsten decreasing to 94 at.% tungsten by the end of the period.[23] These inventory changes were predicted by the FISPACT code,

which uses nuclear reaction data, radioactive decay data and fission yield data from nuclear data libraries; ~10 % of the data is from experiment only, with the remaining data being generated from theoretical models.[25] Verification of these calculations by experimental results from neutron-irradiated tungsten would be desirable for predicting transmutation in DEMO, or future power-plant reactor.

2.2.3.2 Cascades

Displacement cascades occur when a neutron collides with an atom in the material and displaces it from its lattice site. The displaced atom – or "primary knock-on atom" (PKA) – can both ionise and collide with other atoms, with the latter causing a transfer of energy to other KAs so that, over time, a series of "displacement cascades" is generated through the material, leaving clusters of defects such as interstitials and vacancies.[26,8,4] This sort of damage can be described in terms of displacements per atom (dpa), i.e. the number of times each atom in the lattice is displaced from its site; the use of dpa has become the international convention for quantifying displacement damage.[26] Collision cascades occur over tens of picoseconds, a time scale which is suited to modelling by molecular dynamics. Simulations show that localised, compact cores of interstitials and vacancies formed in the early stages of the cascade, before the majority of them annihilate each other shortly afterwards (Figure 2.2).[27]

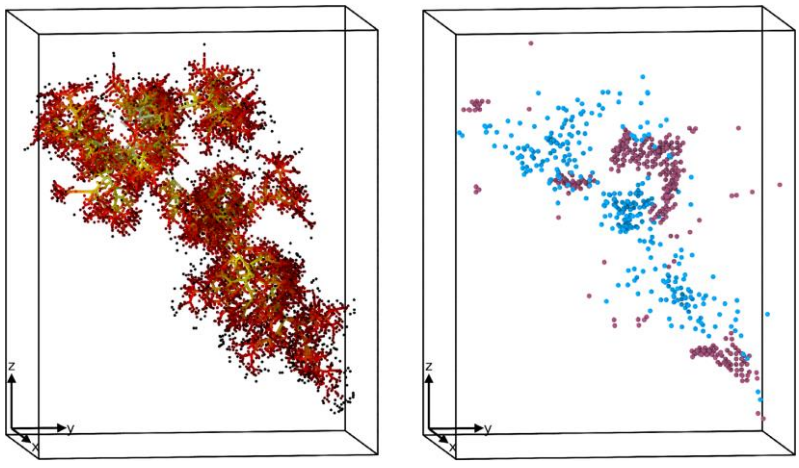


Figure 2.2: *Evolution of a displacement cascade in tungsten from a 200 keV PKA up to 300 fs after collision (left), showing recoils with E_{kin} >10 eV, and after 40 ps (right), showing remaining vacancies and interstitials.*[27]

2.2.3.3 Microstructural Defects

The small fraction of defects that survive the cascades can accumulate to leave a microstructure populated with vacancy and interstitial clusters and dislocation loops, all of which act as barriers to dislocations. These radiation-induced defects act to harden the material and reduce its fracture toughness in a process known as low-temperature embrittlement (i.e. up to $0.35T_M$, where T_M is the melting temperature of the plasma-facing material).

At intermediate temperatures where vacancy mobility increases (between $0.35T_M$ and $0.5T_M$) irradiation creep and void swelling becomes a concern and may lead to dimensional instability.[4,22] Body-centred cubic (bcc) materials such as tungsten have been found to demonstrate significantly less swelling than their face-centred cubic (fcc) counterparts, due to the formation of more finely dispersed point defects and smaller defect clusters in BCC metals;[4] a finer defect distribution allows for efficient defect recombination in the event of structural changes.[8]

Moreover, at high temperatures ($> 0.5T_M$) the trapping of He (produced by the D-T reaction and decay of transmutation elements) can lead to bubbles at the grain boundaries, causing a loss of ductility and high-temperature embrittlement.[24] Phenomena such as embrittlement and swelling can be classed as bulk radiation damage.[11] Radiation may also induce segregation in alloys, resulting in cluster formation and leading to variations in properties and performance.[22]

2.2.4 Irradiation Experiments

Neutron irradiation campaigns are expensive and time-intensive. Studies of the neutron irradiation response of fusion reactor materials are limited due to the lack of materials test reactors available. Nuclear fission reactors are used to generate a flux of fast neutrons (of up to 2 MeV); although the neutron spectra produced do not match those of 14 MeV D-T fusion neutrons, the primary damage state created by fusion and fission neutrons is comparable, meaning that the use of the international dpa parameter is acceptable.[4] However, the divertor in a tokamak is expected to experience damage

levels of up 20–30 dpa/year,[28] meaning that obtaining sufficiently high radiation doses using fission reactors could take many years. The storage and testing of neutron-irradiated materials also requires hot cells for several years due to activation, creating additional complications and expenses.

Ion irradiation can be used to mimic the effect of neutrons by creating displacement damage. This method is advantageous because samples are not radioactive after irradiation, and high damage levels may be achieved more quickly.[28,29] Dual and triple ion beam configurations are also used to simulate the fusion environment by combining hydrogen and helium beams. However, microstructures produced by ion beams contain much fewer voids than those produced by neutrons,[30] thus damage mechanisms are not directly comparable. A further disadvantage of ion irradiation is the shallow damage depth produced; the damage layer is less than several microns due to electronic stopping of the charged particles. Transmission electron microscopy (TEM) allows probing of the irradiation damage, particularly dislocation structures, whilst atom probe tomography (APT) may be used to observe chemical changes. However, conventional bulk mechanical tests cannot be used to probe the thin irradiated layer, so micromechanical testing (based upon nanoindentation) must be used to obtain results which are scalable to bulk properties.

2.2.5 The Role of Micromechanical Testing

Micromechanical testing can benefit the characterisation of materials irradiated by both neutrons and ion beams. The size scale of testing typically ranges from tens of nanometres to tens of micrometres. Table 2.2 summarises the advantages of micromechanical testing for both neutron- and ion-irradiated samples for fusion applications.

Table 2.2: *Advantages of micromechanical testing on neutron- and ion-irradiated fusion materials.*[31]

Neutron-irradiated samples	Ion-irradiated samples
Reduces the amount of active material which needs to be handled	Obtaining mechanical properties from accelerated radiations
Large number of tests improves statistics	Large number of tests improves statistics
Re-testing of old archived samples	Measures the entire dose profile

Testing localised areas	Control measurement possible for each specimen
Fundamental quantitative defect-dislocation interaction studies possible	Fundamental quantitative defect-dislocation interaction studies possible

Employing indentation-based techniques (such as nanoindentation) to characterise mechanical property changes after irradiation is well-established within the nuclear industry. However, novel methods are currently being explored to test fracture on the microscale, particularly on features of interest. These methods employ geometries such as micro-pillars and micro-cantilevers.[32]

2.3 Nanoindentation

Micromechanical testing refers to testing on the lower end of the mesoscale spectrum, with a size scale ranging from nanometres to micrometres. Small scale testing is beneficial to samples irradiated by both neutrons and ions; it can reduce the volume of radioactive material required for testing in addition to maximising the mechanical data that can be generated from the limited damage volumes created by ion irradiation. This project will focus on nanoindentation to probe strain rate sensitivity in tungsten and neutron-irradiated tungsten.

Following its introduction in the 1970s, nanoindentation is the most developed micromechanical testing method to characterise changes in mechanical properties such as hardness as after irradiation.[33] During nanoindentation, a diamond indenter tip is pushed into the surface of a material with an applied load and measured displacement. Nanoindentation is relatively simple to perform and requires minimal sample volume and preparation, with the benefit of quickly producing accurate mechanical property data, such as elastic modulus and hardness, from even shallow ion-irradiated layers. While nanoindentation is a useful method for testing ion-irradiated layers or thin films, the influence of the underlying substrate may need to be taken into account, as it may cause the indentation plastic zone to be enhanced or inhibited.

Basic nanoindentation uses the 'static' load-unload method: during a loading cycle, force and penetration depth are recorded, allowing the contact area, and thus hardness, to be determined from the load-displacement curve. A typical load versus indenter displacement curve is shown in Figure 2.3. Development of the Oliver–Pharr method[34] allowed extraction of the elastic modulus from the unloading curve.

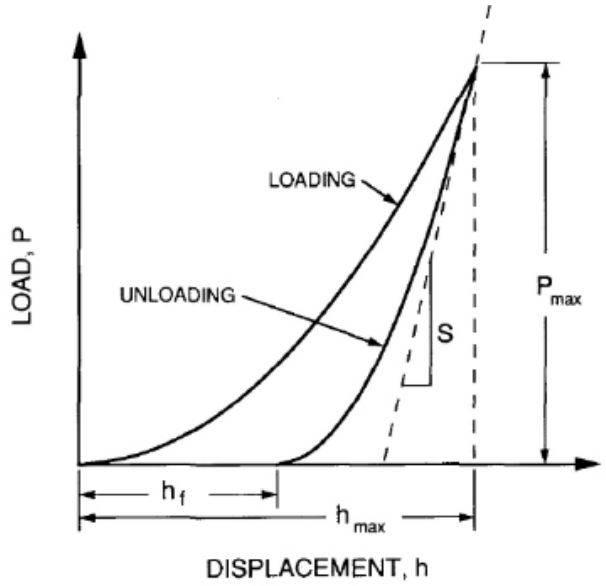


Figure 2.3: *Schematic of load versus displacement data for an indentation experiment.*[34] *The quantities shown are P_{max}: the peak indentation load; h_{max}: the indenter displacement at peak load; h_f: the final depth of the contact impression after unloading; and S: the initial unloading stiffness.*

2.3.1 Developments in Nanoindentation

Recent advancements in testing have originated from incorporating the continuous stiffness measurement (CSM) method.[34,35] The technique, also referred to as 'dynamic nanoindentation', allows the contact stiffness (and contact area) of the sample to be measured continuously, and not just at the point of unloading, by imposing a small but high-frequency oscillation (>40Hz) on the indenter tip.[36] This enables constant evaluation of the Young's modulus and hardness throughout the depth of the indentation, with measurements possible at very small depths, which is ideal for probing property changes in ion-irradiated material. Furthermore, CSM enables creep, fatigue, and strain rate

sensitivity to be determined with little sensitivity to thermal drift due to the high oscillation frequency.[31,36] The method has become a standard feature on modern nanoindenters.

Another technique to measure hardness and modulus as a function of depth is the load/partial-unload method,[37] also known as 'quasi-static indentation', in which multiple load/partial-unload sequences of increasing maximum load occur over the total indentation depth. The sample is first loaded to a specified load (P_{max}) which is held for a defined time, before partial unloading to a fraction of P_{max}. This process is then repeated with a higher P_{max} for each successive cycle, with a holding period between each one.

There is debate over whether the resulting hardness measured is affected by the indentation technique used, although both methods are used extensively in literature. Differences in hardness values have been reported for CSM tests due to the superimposed oscillating force, particularly at low indentation depths (< 200 nm).[38,39] Cordill *et al*. attributed the decreased hardness of nickel to a phenomenon coined the 'Nano-Jackhammer Effect', in which the indenter acts as a jackhammer and increases dislocation nucleation during dynamic indents than quasi-static indents.[38] The effect of softening is most pronounced in ductile materials and thin films.

Leitner *et al*. studied a range of materials using both methods and found that CSM hardness measurements were higher than static measurements at greater strain rates, but results were comparable for lower strain rates. However, the hardness difference was observed across displacements larger than 200 nm. It was concluded that the deviations in hardness measurements arose from strain-rate changes during the dwell segments of the quasi-static tests; these differing strain rates were used to determine hardness.[40] The magnitude of the discrepancy thus depends on the strain rate sensitivity of the material, as opposed to the technique used. It is therefore recommended that the physical indentation strain rate is obtained from the load-displacement data for each hold segment[40] – the approximate indentation strain rate is defined as loading rate divided by load for sharp indenters.[41] It is also particularly important to consider whether a material shows a

dependence on loading history when looking at strain rate sensitive metals using (quasi-)static testing.[42] However, both the partial unloading and dynamic indentation methods record the elastic recovery of material, allowing determination of the transition from elastic to plastic behaviour using spherical tips.[43]

2.3.2 Pile-Up and Sink-In

During nanoindentation, material around the indenter tip may deform upwards or downwards in the z-axis (demonstrated in Figure 2.4), respectively causing pile-up or sink-in under elastic/plastic conditions.[44] The extent of pile-up or sink-in is related to the proximity of the plastic deformation to the indenter.[45] Materials exhibiting a low ratio of yield stress to elastic modulus, or little to no work hardening behaviour (e.g. if heavily pre-strained), tend to pile-up upon indentation; conversely, materials with a high work hardening potential (e.g. post-annealing) undergo sink-in.[34,46] Unfortunately these surface deformation modes can influence the actual contact area, which is underestimated and overestimated for pile-up and sink-in respectively (Figure 2.4); this can cause errors or artifacts in mechanical properties calculated from the assumed contact area using measured displacements and the calibrated tip area function.[45] For example, the underestimated contact area in the pile-up condition can lead to overestimations of the hardness and elastic modulus, with a greater error over increasing indentation depth.[36]

Furthermore, pile-up or sink-in can be more pronounced in tests which involve indentation of a thin coating on an underlying substrate. As a result, the material underneath the thin damage layers produced by ion irradiation can affect the surface deformation behaviour during indentation. Differences in the extent of pile-up or sink-in between irradiated and unirradiated materials may therefore affect the measurement of radiation-induced changes in mechanical properties.[45] Since pile-up can introduce a greater apparent irradiation hardening due to restricted growth of the plastic one in the damage layer, corrections are needed to account for irradiation-induced pile-up when examining property changes.

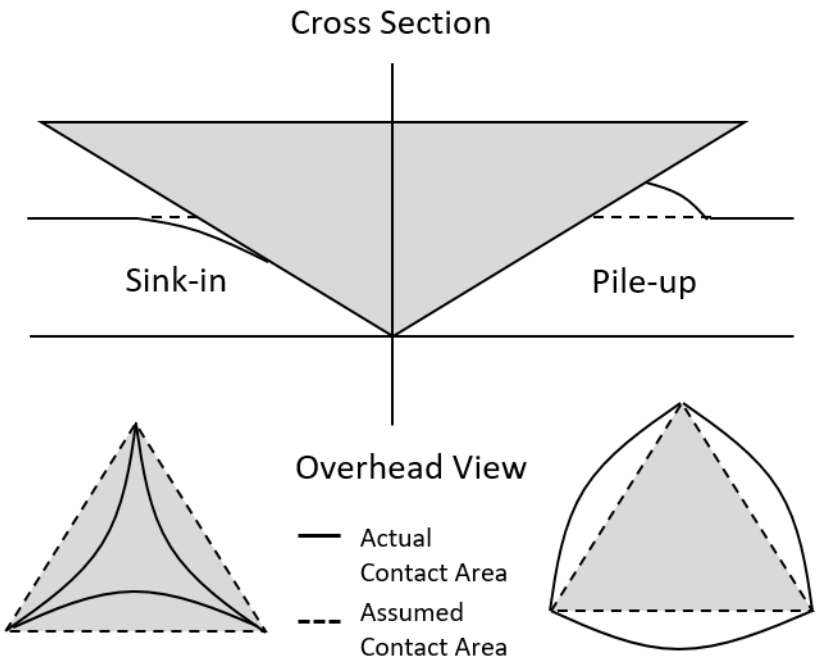


Figure 2.4: *Schematic drawing of pile-up and sink-in reproduced from McCann & Corcoran.*[136] *The top half of the figure illustrates the cross-section of the indenter at maximum load. The bottom half shows the projected area of contact based upon displacement is overestimated in the sink-in case, and underestimated for the pile-up case.*

2.3.3 Berkovich Indentation

Pyramidal indenters (three-sided Berkovich and four-sided Vickers) are commonly used in nanoindentation, although the Berkovich tip is preferred for smaller scales since it is more easily ground to a sharp point. Berkovich tips are also self-similar in geometry, meaning that they produce a constant plastic strain, typically of 7 – 8 %.

For fracture toughness evaluation, the cube corner indenter, also three-sided, may be used as it can displace a larger volume of material at the same load, thereby producing much greater stresses and strains in whilst reducing the amount of cracking.[36] The cube corner tip also results in the smallest plastic zone and can be beneficial for thin surface layers; however, Hardie *et al*. found that pile-up differences between an irradiated and unirradiated Fe-Cr alloy produced significant errors in the perceived irradiation hardening if the area function, as opposed to the direct contact area measurement, is used.[45] The Berkovich tip thus proved a useful compromise, exhibiting moderate pile-up but with a small plastic zone size.

One challenge in the interpretation of nanoindentation data is the depth dependence of the hardness measured. An indentation size effect (ISE) can be observed in a range of materials indented by Berkovich tips, whereby hardness appears to increase with decreasing indentation depth. A model for this size effect was produced by Nix and Gao[47] in 1998 using the Taylor dislocation model. It is assumed that the indenter is accommodated by circular loops of geometrically necessary dislocations (GNDs) with Burgers vectors in the direction normal to the sample surface, with GND density being proportional to the inverse of indentation depth.

2.3.4 Spherical Indentation

Unlike pyramidal indenters which produce a constant strain, the geometry of the sphere causes the strain to vary with penetration depth, and increase from zero in a manner analogous to conventional tensile testing. A spherical tip initiates elastic contact and yielding before causing elastic–plastic contact at higher loads, and is thus well suited to examine yielding and work hardening characteristics using either the partial unloading or CSM techniques.[32,43]

Spherical indentation originated in 1900 when the Brinell hardness test was developed, based on the residual indentation surface area.[48] In 1908, Meyer defined hardness as the maximum load applied by a spherical indenter divided by the projected area of indentation;[49] this definition was widely considered as a more suitable approach than that of using the residual indent. In 1951, Tabor found that an indentation stress-strain curve can be produced by relating hardness to uniaxial stress without the need for a large volume of test material.[50] Stress was defined as $P_m/2.8$ and indentation strain as $0.2a/R$ where P_m *i*s mean indenter pressure, a is the contact radius and R is the indenter tip radius.[50]

Many advances have been made in the data analysis of spherical indentation, largely built upon Hertzian contact mechanics between two isotropic elastic solids[51] and Sneddon's theory for elastic displacements,[52] allowing hardness and modulus to be extracted throughout an indent.[37] However, tip calibration is crucial for accurate determination of materials properties as the radius of the tip is not constant, and the shape may deviate from a spherical one. Since elastic deformation may vary

with the area in contact, an effective radius R_{eff} can be used;[53,54] Bushby and Jennett developed methods to calibrate R_{eff} from reference materials using Hertzian contact mechanics.[53] More recently, Kalidindi and Pathak observed that due to the difficulties in determining R_{eff} for each point in the loading segment, the majority of studies instead used the indenter radius to calculate a/R indentation strain. They proposed a new definition of indentation strain:[55]

$$\varepsilon_i = \frac{4h}{3\pi a_c} \tag{2.2}$$

with h as the total displacement and a_c as the contact radius derived from Hertz's law. This definition has been widely regarded as more meaningful and reliable in used successfully to investigate the indentation stress-strain response of numerous materials.[56,57,58]

However, their approach required back-calculating the contact area from the stiffness signal of isotropic samples, since the reduced modulus is constant. Leitner *et al*.[58] developed a novel method to calibrate spherical tips which accounts for imperfections without prior knowledge of the reduced modulus; successful determination of accurate contact areas in turn enabled them to extend their calibration to the elastic-plastic regime and perform strain-rate controlled tests. Furthermore, Zhu *et al*.[43] observed a relationship between yield strength, indenter radius and contact radius, concluding that there is an inverse square-root dependence of yield strength on the contact radius, demonstrating the need for a comprehensive tip calibration. The transition from the elastic regime often occurs at a low strain for metals, thus determining the yield point may be a complicated process. The authors proposed a method whereby the yield point can be inferred from extrapolating the data in the plastic flow region back to the point of intersection with the elastic line.[43]

One of the drawbacks of spherical indentation is the indentation size effect (ISE). Lim *et al*.[59] and Durst *et al*.[60] showed that the ISE for spherical indenters depends on tip radius, whereby indentations with a small tip radius yield a greater deformation resistance, and thus increased hardness, from the material. This is in contrast to self-similar indenters for which the ISE is manifested through

indentation depth. Swadener *et al*.[61] further related spherical indentation to conical indentation and modified Nix and Gao's ISE model for Berkovich indentation, but whilst their experimental and model results are in reasonable agreement for larger indenter tips, the predictions deviate from macroscopic behaviour for indenter sizes of less than 100 μm. Importantly, Pharr, Herbert and Gao[62] noted that hardness increases with depth of penetration, which results from the fact that spherical indenters are not geometrically self-similar, causing the induced strain to increase with depth, with a greater increase if the material work hardens.

A further issue with spherical indentation is the accurate determination of the zero point – the point at which the indenter first makes contact with the surface. Most methods of locating the zero point are based on deviations in the measured stiffness signal at the point of contact, requiring a finite penetration depth and thus introducing uncertainty in determining the exact location.[55,56]

Nonetheless, spherical indentation has been demonstrated to effectively characterise a range of materials, including shallow ion-irradiated layers.[63,45,57,64,65] A comprehensive study by Bushby *et al*.[64] used spherical indenters with radii between 5 to 20 μm to determine the evolution of plastic deformation, in addition to measuring the initial yield pressure and elastic modulus of Fe-Cr alloys, in the irradiated and unirradiated form.

A further benefit is that the use of a spherical tip removes the complexity of the in-plane indenter orientation relative to the crystal when examining the effect of orientation in a material – as is the case for non-rotationally symmetric tips like the Berkovich.[65] Correspondingly, spherical indenters also allow for simplification of the modelling process.

2.4 Strain Rate Sensitivity

2.4.1 Deformation of Body-Centred Cubic Materials

There has been great interest in the underlying deformation mechanisms of body-centred cubic (bcc) metals within the last few decades.[66,67,68,69] It is understood that the behaviour of single crystalline bcc

metals is different to that of face-centred cubic (fcc) metals, in that plastic deformation is influenced by temperature, strain rate, and orientation. At low homologous temperatures ($T < 0.3T_M$, where T_M is the melting temperature in K), deformation is primarily governed by the thermally-activated motion of screw dislocations which are not confined to one set of crystallographic planes.[70,71] Bcc metals also exhibit tension–compression asymmetry due to a breakdown in the Schmid's law, by which slip occurs on crystallographic planes rather than the one with the maximum resolved shear stress.[66]

Below a critical temperature T_c (800 K for tungsten),[72] the strength and deformation resistance of bcc metals is strain-rate sensitive, and screw dislocation mobility via the kink pair mechanism requires a thermally-activated stress component σ^*. This thermal stress component arises because thermal energy is small relative to the high Peierls potential. The Peierls potential is related to the intricate three-dimensional core structure of $a_0\langle 111\rangle/2$ screw dislocations, and results in high flow stresses for high T_c materials such as tungsten. For low ($T > 600$ K) and intermediate ($220\ K \leq T \leq 600$ K) stresses, kink-pair formation takes place on the {211} plane, whereas the process takes place on {110} glide planes for high stresses ($T \leq 220$ K).[72] Near T_c, the thermal stress component decreases, whilst the potential athermal stress component σ_a increases, and therefore dominates the mechanical behaviour. Above the athermal temperature T_a, the plastic behaviour of bcc metals becomes less rate-dependent and more similar to that of fcc metals.[68]

2.4.2 Strain Rate Sensitivity and Activation Volume

A number of techniques have been used to assess the thermodynamic and kinetic characteristics of plastic deformation in metals. In addition to using constant strain-rate tests, one of the most common methods is the strain-rate jump (SRJ) test at a constant temperature; whether under compression or tension, the rate at which the specimen is deformed is changed within the test. Lucas and Oliver proposed a $\dot{P}/P$ (loading rate divided by load) technique to control the loading rate, and thus indentation strain rate, using a Berkovich indenter.[41]

In uniaxial tensile or compression testing, the SRS is defined as the change in stress σ divided by the change in strain rate $\dot{\varepsilon}$ at constant temperature as follows:[73]

$$m_{uniaxial\ testing} = \frac{d\,(ln\,\sigma)}{d\,(ln\,\dot{\varepsilon})} \tag{2.4}$$

where *m* is the SRS exponent which describes the SRS behaviour of a material by assuming a constant microstructure. *m* can be determined by using either strain-rate jump tests during a single macroscopic test, or from several tests at different strain rates.

For nanoindentation SRS measurements, a variety of approaches have been reported in literature. Mayo and Nix[73] conducted micro-indentation tests at constant loading rates to determine a stress exponent; upon yielding consistent results, they concluded that, although indentation stresses and strains are not equivalent to uniaxial flow stresses or strain rates, they are still proportional to the uniaxial quantities (in general, uniaxial flow stresses tend to be 10-20% of the indentation stresses). Hence, the nanoindentation SRS can be defined by:

$$m_{nanoindentation} = \frac{d\,(ln\,H)}{d\,(ln\,\dot{\varepsilon})} \tag{2.5}$$

The Tabor relation can also be used (the yield stress σ_y of a metal is approximately one third of its nanoindentation hardness or microhardness; i.e., $H = 3.\sigma_y$ where yield stress is equivalent to flow stress σ_f at a specified strain for work-hardening materials).[50] As a result, the activation volume *V* (determined by the mechanism of plastic deformation) can be written as:

$$V = \frac{\sqrt{3}kT}{m.\sigma_f} \approx \frac{3\sqrt{3}kT}{m.H} \tag{2.6}$$

V is a measure of the volume of a material involved in overcoming a thermally activated barrier which is often given in terms of b^3, where *b* is the strength (or magnitude) of the Burgers vector of dislocations. *k* is the Boltzmann constant, and *T* is the absolute temperature.

2.4.3 Nanoindentation Strain-Rate Jump Tests

Wei *et al*.[68,69] postulated that ultra fine-grained (UFG) and nanocrystalline bcc metals would exhibit a reduced SRS compared to their coarse-grained counterparts, and successfully confirmed this by performing macroscale tensile tests with strain rate jumps to extract *m* and *V*. In 2011, Maier *et al*.[74] introduced a nanoindentation SRJ test using a Berkovich tip: a standard continuous stiffness measurement (CSM) method was adapted to change the applied strain rate at defined depths in a single indent – termed "strain-rate jumps" – allowing hardness measurements at different strain rates (demonstrated in Figure 2.5). It is assumed that the internal microstructure such as mobile dislocation density is unchanged by altering the plastic deformation rate, allowing a local determination of the strain rate sensitivity (SRS) unaffected by thermal drift and influences of long testing times at low strain rates.[69,74] This method was proposed as a more precise and reproducible testing procedure to determine the SRS, whilst enabling a depth-dependent resolution of the SRS.

Maier *et al*.[70] yielded similar results to Wei by using the nanoindentation SRJ tests, finding that single-crystalline tungsten (SX-tungsten) was more rate-sensitive than UFG tungsten (produced by severe plastic deformation using equal channel angular pressing, ECAP). The enhanced SRS of SX-tungsten arises from the high lattice friction of bcc metals at low temperatures, whereas the reduced SRS of the UFG tungsten is attributed to an enhanced athermal stress component σ_a due to the severe plastic deformation and grain boundary formation in fabrication. Whilst the thermally activated component σ^* is not reduced, it is likely that the Peierls potential is shifted to higher stress levels. Consequently, for grain sizes as small as 1 μm, it was concluded that interaction between screw dislocations and grain boundaries also play a role in the SRS, in addition to the screw dislocation motion which is dominant for SX-tungsten. A reduced SRS in the fusion environment would undoubtedly be preferable, and it is highly unlikely that SX-tungsten will be used. It is notable that the similarity in results demonstrates that the nanoindentation SRJ test is a useful tool when testing the SRS of small volumes.

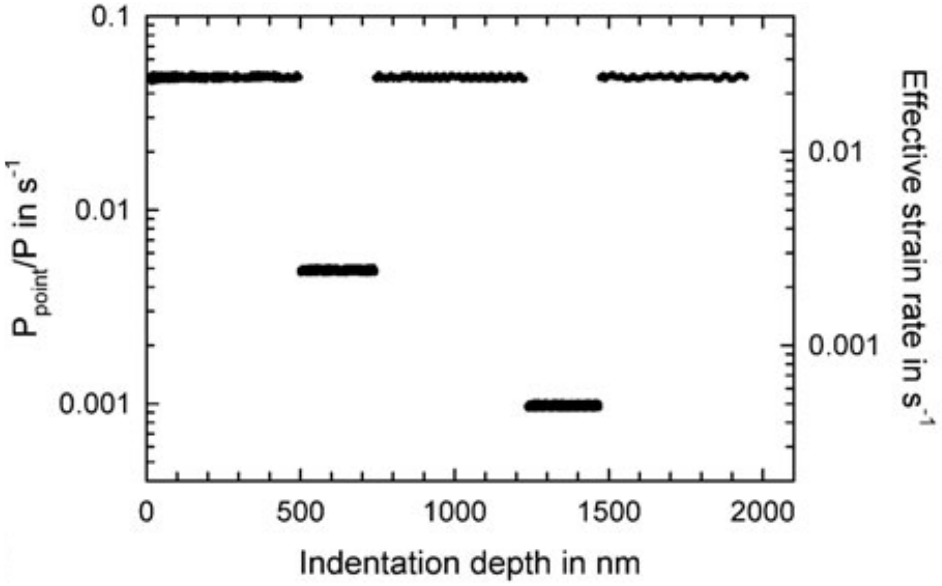


Figure 2.5: *Nanoindentation strain-rate jump test with three different applied strain rates. Graph shows the applied indentation strain rate ($\dot{P}/P$) and corresponding strain rate versus indentation depth.*[74]

2.4.4 Constant Strain Rate Tests using Spherical Nanoindentation

As discussed in 2.4.3, the geometry of spherical indenters offers the ability to determine material properties as a function of strain, unlike the Berkovich indenter, which only provides SRS at a plastic strain of approximately 8 %. Feldner *et al*.[75] initially addressed the challenge of varying strain rate during spherical indentation (using Kalidindi and Pathak's definition of strain) by assuming elastic contact, a perfect sphere, and a strain rate proportional to $\dot{P}/P^{2/3}$; the strain rate definition is similar to that of sharp indenters, which is proportional to $\dot{P}/P$, but can lead to an increase in strain rate over displacement in spherical indentation. Nonetheless, it was shown that SRJ tests can be implemented using spherical indenters.

As described in 2.3.4, Leitner *et al*.[58] used a novel method of tip calibration by calculating the area function of a sphere, thus accounting for imperfections and allowing a correct strain rate to be calculated. Furthermore, the authors tuned the proportional-integral-derivative (PID) parameters of the nanoindenter to achieve high strain rates. These strain-rate controlled tests were successfully used to measure the same value of SRS in a GaAs wafer using constant strain-rate spherical indentation and

Berkovich SRJ tests. SRJ tests were also performed with a spherical tip in an Al alloy, again yielding the same value of SRS.

It is important to note that work hardening behaviour must be obtained from a constant strain rate in spherical indentation, particularly in more rate-sensitive materials such as body centred cubic or nanocrystalline materials. The use of CSM indentation can facilitate this, whilst multiple unloading tests, in which the strain rate drops for each cycle, may produce misleading results in rate-sensitive materials.[40]

2.4.5 Effect of Composition and Radiation on Strain Rate Sensitivity

It is currently known that the SRS of tungsten reduces above its T_c of 800 K, and the SRS of tungsten has been investigated up to a strain rate of 0.05 s^{-1} by Maier *et al*.[70] (discussed in 2.4.3). Abernethy *et al*.[76] also used four-point bend tests to determine the activation energy of the BDTT in tungsten before (1.0 eV) and after neutron irradiation to 1.7 dpa (1.05 eV from irradiated tungsten composed of W-1.2%Re-0.1%Os). Neutron irradiation caused the BDTT to increase by 500 °C. However, using the nanoindentation SRJ test method, the activation volume for dislocation motion was measured as 4.6 b^3, which is very similar to that of unirradiated tungsten. Kink-pair formation is thus determined as the controlling mechanism for the BDTT before and after irradiation.

Although this may be the case for W-1.2%Re-0.1%Os at low strain rates of 3.5×10^{-7} to 2.5×10^{-5} s^{-1}, a composition of W-3.8%Re-1.4%Os-0.8%Ta is predicted after five years in DEMO (Table 2.1) and strain rates of up to 3 s^{-1} for disruptions and 8 s^{-1} for ELMs are expected. Thus, it is essential to investigate the effect of high strain rates and radiation damage on the performance of tungsten in a fusion reactor.

2.5 Studying Indentation using Computational Modelling

2.5.1 Crystal Plasticity Finite Element Modelling

Computational mechanics, and specifically, the finite element method (FEM), enables the study of plasticity. The origin of plasticity in crystalline materials such as metals is crystal slip. Reaching an approximate analytical solution to such complex problems requires that equilibrium, constitutive equations, boundary conditions and compatibility are satisfied.[77] The use of FEM allows the examined body to be discretised into a finite number and elements and nodes.

Plasticity can be modelled at the continuum scale, or at the microscale. In microplasticity modelling, slip is confined to specific directions dependent on the material's crystallography. Crystal plasticity modelling can be employed to obtain microstructural-level information such as lattice rotations and curvatures and geometrically necessary dislocation density,[78] allowing the determination of stress and plastic strain.[79] Crystal plasticity finite element (CPFE) modelling will be discussed more extensively in Chapter 6. This project will aim to use CPFE modelling to study the effect of strain rate on deformation behaviour by modelling spherical nanoindentation in unirradiated and neutron-irradiated tungsten and comparing with the results of characterisation experiments.

2.5.2 Studying Deformation Behaviour

A combination of ion-irradiation and nanoindentation is commonly used to gain insight into the radiation damage of materials. Interestingly, differences in pile-up morphology around nanoindents have been observed following irradiation in several materials, even for low damage levels. Das *et al*.[65] observed that several nanoindentation studies led to seemingly contradictory results. For example, Berkovich indents into 0.3 at.% helium-implanted W-1% Re resulted in a large amount of pile-up,[80] whilst pile-up suppression was observed around indents in W-5%Ta implanted with 2MeV W^+ ions to 0.07 dpa, despite significant pile-up observed in the unimplanted material.[81]

Pile-up is widely considered negligible in the determination of the contact area to calculate hardness and modulus values, but the extensive pile-up observed in ion-irradiated tungsten can lead to a substantially increased contact area. Pharr *et al*. also reported pile-up differences in materials with residual stresses – large compressive stresses were found to promote pile-up while tensile stresses caused a reduction.[82] Beck *et al*. proposed a correction method using independent measurements of the elastic modulus in irradiated material, allowing pile-up correction and accurate hardness measurements.[80] As mentioned in Section 2.3.2, pile-up and sink-in are generally associated with low and high strain-hardening potentials respectively. Although pile-up corrections are gaining popularity, the effect of crystallographic orientation is not usually considered in studies of ion-irradiated material and deformation behaviour.

Wang *et al*.[46] found pile-up patterns in copper to be strongly orientation dependent using both conical nanoindentation of (001) orientated copper single crystals and elastic-viscoplastic CPFE modelling. Kusenko *et al*.[83] further used a strain gradient CPFE simulation, validated with experiments, to reveal how the hardness anisotropy of beryllium arises from the anisotropy in the plastic deformation. Pile-up and sink-in behaviour dominated in “soft” and “hard” orientations respectively, further implying the standard Oliver-Pharr approach[34] must be combined with a consideration of pile-up or sink-in.

Similarly, Das *et al*.[65] found a strong dependence of pile-up on crystal orientation in tungsten, which clarifies the discrepancies in results reported for the material. Pile-up from nanoindentation was explored in a tungsten polycrystal in both the unimplanted and helium-implanted conditions, considering grains with ⟨001⟩, ⟨110⟩, and ⟨111⟩ out-of-plane orientations. Atomic force microscopy (AFM) of spherical indents in unimplanted tungsten showed little orientation dependence, whereas the implanted material exhibited larger and more localised pile-up in ⟨001⟩ grains compared to other orientations. Due to the orientation-dependent pile-up, the impression of the indenter is a defined square shape (with the sides of the square along the ⟨100⟩ direction). Thus, the crystal orientation

must be considered when investigating the pile-up morphology and deducing hardness values from nanoindentation.

Das *et al*. used a physically-based strain-gradient CPFE model – initially reported in 2018[84] and based on the (user element) UEL originally written by Dunne *et al*.[85,86] – to simulate nanoindentation in helium-implanted ⟨001⟩ single crystal tungsten. Although spherical nanoindentation was used for rotational symmetry, the authors noted that the AFM results showed tip imperfections. Nonetheless, by considering thermally-activated dislocation glide through helium-defect obstacles, the model correctly predicted the localised pile-up for each crystal orientation, and calculated lattice distortions and geometrically necessary dislocations (GNDs) in the deformation field beneath indents. The latter results were in strong agreement with previous microbeam Laue diffraction measurements of the plastic zone deformation in the helium-implanted sample.[87]

In another body of work, Das *et al*.[88] examined pile-up around spherical indents in ⟨001⟩ grains from self-ion implanted tungsten, with damage levels ranging from 0.01 to 1 dpa. AFM and high resolution electron backscatter diffraction (HR-EBSD) were used to quantify pile-up, lattice strains and GND density, and the CPFE model mentioned previously was used to predict the macroscopic deformation behaviour. The effect of damage level was explored in the model by varying the initial shear resistance of irradiation defects and softening rate to match the hardening and strain-softening observed in stress-strain curves. The model's predictions agreed well with corresponding measurements from AFM and HR-EBSD, highlighting the potential of CPFE modelling in designing fusion components and predicting their behaviour.

The same UEL written by Dunne *et al*.[85,86] was also used by Cackett *et al*.[63] to model the spherical indentation of single crystal copper in combination with results from AFM and EBSD, examining pile-up and plastic zone deformation. The authors highlighted the value of comparing model and experimental, providing an enhanced understanding of the underlying plasticity mechanisms in addition to validation of the model. It was found that the hardening law incorporating the evolution

of GNDs was insufficient to simulate the hardening effect observed from nanoindentation, suggesting other mechanisms were responsible.

Since pile-up can introduce inaccuracies in measuring the hardness and irradiation hardening of tungsten, it is important that the effect of strain rate on the pile-up observed is characterised using nanoindentation and CPFE modelling. Moreover, the use of AFM and HR-EBSD can support the examination of the indentation plastic zone and provide a means of validating indentation models.

2.6 Summary and Aims

Tungsten is the leading candidate for divertor applications in fusion reactors owing to its excellent thermomechanical properties. During operation, plasma-facing materials are subjected to temperatures of up to 1000°C (or greater during transient heat fluxes of 20 MW/m^2), high strain rates, and bombardment by neutrons; the latter can cause irradiation damage in addition to transmutation to other elements, ultimately changing the material's physical and mechanical properties. Furthermore, high strain rates in the event of a plasma disruption can cause premature cracking. Body-centred cubic materials such as tungsten are known to exhibit strain rate sensitivity, which is primarily governed by the thermally-activated motion of screw dislocations. As a result, considering the effect of strain rate on the mechanical properties neutron-irradiated tungsten for fusion is essential.

Although the damaging effects of neutron irradiation on tungsten have been studied previously, little characterisation of the strain rate sensitivity in irradiated tungsten has been performed; most tests have been performed at strain rates under 0.05 s^{-1} or at undisclosed values, despite the fact that values of 3 s^{-1} for plasma disruptions and 8 s^{-1} for ELMs are expected. Similarly, few studies have investigated the effect of strain rate on the hardening and stress-strain response of neutron-irradiation tungsten. As spherical nanoindentation experiments allow indentation stress-strain curves to be generated, this method enables the indentation yield strength and work hardening behaviour to be examined at different strain rates.

Interestingly, previous studies of the topography around spherical nanoindents have revealed the production of material pile-up in tungsten, which is further exacerbated by ion-irradiation. The pile-up condition is generally associated with materials exhibiting a low strain-hardening potential and can lead to a substantially increased nanoindentation contact area, causing artifacts in mechanical properties calculated from the assumed contact area, such as an overestimation of the hardness and elastic modulus.

This project will aim to explore the strain rate sensitivity of both unirradiated and neutron-irradiated single crystal tungsten through the investigation of mechanical and deformation behaviour. A combination of micromechanical testing and characterisation, in addition to CPFEM, can be used to conduct strain-rate testing, examine changes in pile-up morphology, and quantify the effects of deformation behaviour of neutron-irradiated tungsten through the analysis of the elastic strains, lattice rotations and geometrically necessary dislocations.

3 Experimental Methods

3.1 Materials and Sample Preparation

Two samples were examined in this work. The first was obtained from commercially pure single crystal tungsten (procured from Goodfellow). This had the form of a disc, 4mm thick and 7mm in diameter, with [001] out-of-plane orientation.

The second was a 1 x 1 x 12mm bar of commercially pure single crystal tungsten, sourced from Metal Crystals and Oxides Limited (Cambridge, UK), cut along the ⟨100⟩ directions with [001] out-of-plane orientation. This 'matchstick' sample was prepared for neutron irradiation and previously studied in multiple publications.[30,76,89]

Both samples were mechanically ground with coarse to fine SiC papers (800 to 2500 grit finish), before polishing with 6 μm, 3 μm and 1 μm diamond pastes. This was followed by polishing with colloidal silica suspension to achieve a stress-free surface. The disc and bar were further electropolished at room temperature in 1% and 0.5% NaOH aqueous solution respectively; this step was taken to remove any residual damage from mechanical grinding and polishing and ensure that a smooth surface was obtained for high resolution electron backscattered diffraction (HR-EBSD).

3.2 Neutron Irradiation

The single crystal tungsten bar characterised in this study was irradiated for 208 full power days in the High Flux Reactor (HFR), Petten at 1173 K as part of the Extremat-II campaign in 2008.[30,76,89] Single crystal matchsticks were irradiated in two positions, for 148 and 60 days in each position respectively. The neutron flux was 6.8 x 10^{18} m^{-2} s^{-1} (3.2 x 10^{18} m^{-2} s^{-1} E> 0.1 MeV) and 6.6 x 10^{18} m^{-2} s^{-1} (3.2 x 10^{18} m^{-2} s^{-1} E> 0.1 MeV) in each location respectively.[89] FISPACT-II simulations by Gilbert *et al*. calculated that a radiation damage of 1.67 dpa was produced at a dose rate of 9×10^{-8} dpa s^{-1}, using a displacement threshold energy of 55 eV.[76]

A composition of W - 1.4 at.% Re - 0.1 at.% Os - 0.02 at.% Ta was predicted, but the neutron energy spectrum of the sample was lowered by the presence of an adjacent specimen, in both locations, which strongly absorbed thermal neutrons, as described in previous works.[76] The post-irradiation composition measured using Energy Dispersive X-Ray Spectroscopy (EDX) and Atom Probe Tomography (APT) was W - 1.20 ± 0.11 at.% Re - 0.11 ± 0.05 at.% Os - 0.03 ± 0.01 at.% Ta.[30] Despite the reduction in thermal neutrons, the fission neutron energy spectrum was lower than one would expect in a fusion reactor, and the increased ratio of thermal neutrons led to a greater transmutation rate (~0.8 % Re dpa^{-1}) compared to that predicted for DEMO (0.1 % Re dpa^{-1}).[90] The 14.1 MeV neutrons in fusion reactors have a lower capture cross section than thermal neutrons.

3.3 Berkovich Nanoindentation

3.3.1 Background Theory

During nanoindentation, the Berkovich indenter tip is driven into the surface of a material using an applied load and the displacement measured. The hardness can be calculated using the indentation load divided by the projected area of contact.[50] The elastic modulus can be determined from the unloading portion of the load-displacement curve (shown in 2.3) using the contact stiffness at maximum load and the elastic contact area.

The unloading curve can be described by the power law in Equation 3.1: P is the load; $(h - h_f)$ is the elastic displacement (h and h_f are displacement into the surface and residual elastic displacement respectively); A and m are material fitting constants.[34]

$$P = A(h - h_f)^m \qquad (3.1)$$

Differentiating and solving Equation 3.2 at peak load and displacement allows the initial unloading slope to be determined, which is referred to as the stiffness:

$$S = \frac{dP}{dh} \qquad (3.2)$$

Contact depth h_c at peak load is obtained from h and the indenter geometric constant ϵ:

$$h_c = h - \epsilon \frac{P_{max}}{S} \tag{3.3}$$

which in turn can used to calculate the projected elastic contact area A_c.[34] For a Berkovich tip, the area function can be approximated as:

$$\mathrm{A_c} \approx 24.56\mathrm{h_c^2} \tag{3.4}$$

A more accurate value of A_c can be determined by fitting a polynomial equation to the tip calibration data from indents in fused silica, which has a known elastic modulus of 72 GPa:

$$A_c(h_c) = m_0 h_c^2 + m_1 h_c^1 + m_2 h_c^{1/2} + m_3 h_c^{1/4} + \cdots + m_n h_c^{1/2^{n-1}} \tag{3.5}$$

The reduced modulus $\mathrm{E_r}$, which accounts for elastic deformation in both the tip and specimen can thus be expressed as:

$$E_r = \frac{S\sqrt{\pi}}{2\sqrt{A_c}} \tag{3.6}$$

The elastic modulus of the specimen can finally be evaluated using the following equation:

$$\frac{1}{E_r} = \frac{1-v^2}{E} + \frac{1-v_i^2}{E_i} \tag{3.7}$$

where E and v are the Young's modulus and Poisson's ratio for the specimen and E_i and v_i denote the same parameters for the indenter. [34]

The indentation strain rate ($\dot{\varepsilon} = dh/h$) can be held constant by maintaining a loading rate divided by the load ($\dot{P}/P$).[41]

3.3.2 Nanoindentation Procedure

Nanoindentation was performed on both unirradiated and neutron-irradiated single crystal tungsten using an Agilent G200 Nanoindenter (now supported by KLA, USA) with a Berkovich diamond indenter calibrated against fused silica. A schematic representation of the G200 is shown in Figure 3.1. The

continuous stiffness measurement (CSM) mode was used, which allows the hardness, elastic modulus and stiffness to be determined as a function of depth by imposing small, high-frequency oscillation.[34] CSM was obtained at an amplitude of 2 nm at 45 Hz. Indents were made to 2000 nm final depth at a strain rate of 0.05 s^{-1}. Arrays of 9 indents were performed for each sample with a spacing of 50µm between indents.

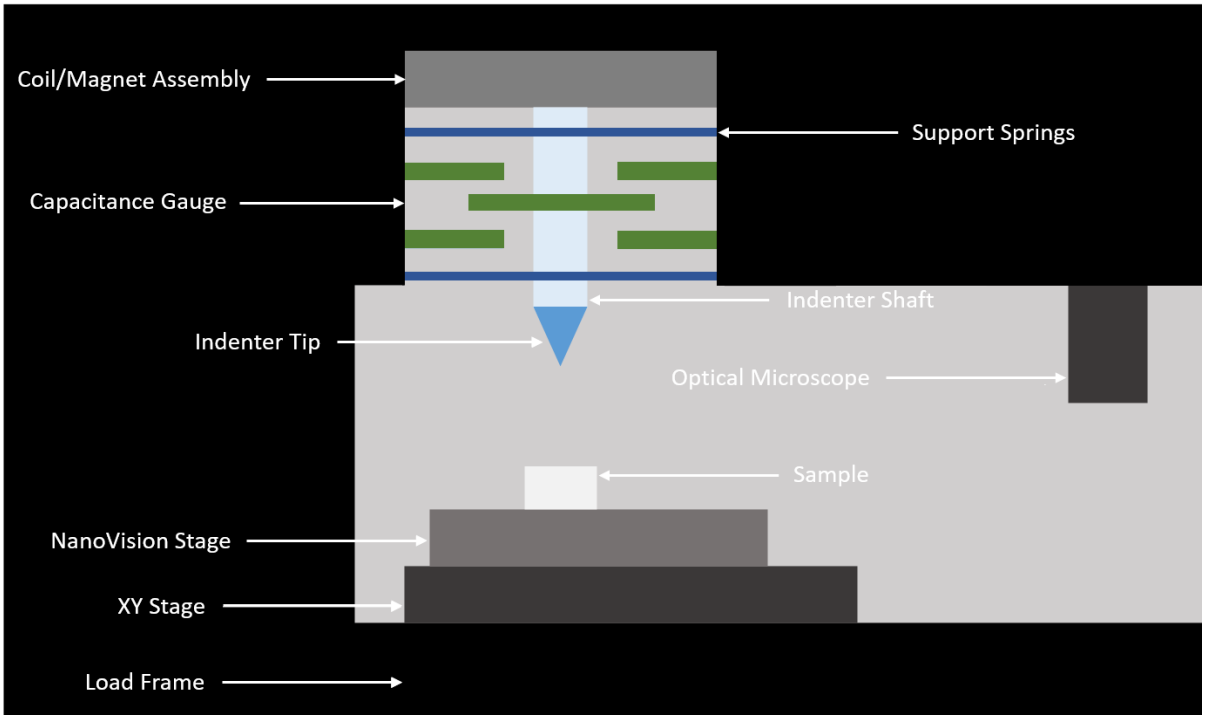


Figure 3.1: *Schematic drawing of G200 nanoindenter.*

3.4 Spherical Nanoindentation

3.4.1 Background Theory

Due to difficulties in manufacturing a perfect spherical tip, particularly with radii of less than 100 µm, it is favourable to use a geometry-based tip area function for calibration, which in turn can enable accurate calculations of strain rate. The tip contact area A_c was defined by Leitner *et al*.[58] as:

$$A_c(h_c) = B_0 {h_c}^{B_1} - B_2 h_c^2 \tag{3.8}$$

where h_c is the contact depth and B_0, B_1 and B_2 are geometric constants. For a perfect sphere, $B_0 = 2R$ (where R is the sphere radius), $B_1 = 1$ and $B_2 = \pi$. The contact radius a_c is therefore defined as:

$$a_c = \sqrt{\frac{A_c}{\pi}} \tag{3.9}$$

h_c is defined by:

$$h_c = h - \epsilon \frac{P}{S} \tag{3.10}$$

where h is the displacement into the surface, ϵ is the indenter geometric constant, P is the indenter load and S is the contact stiffness measured using the continuous stiffness method (CSM).[34]

Recent developments in obtaining stress-strain curves from spherical nanoindentation are discussed in 2.3.4. In this work, Kalidindi and Pathak's definition of indentation strain ε_i was used:[55]

$$\varepsilon_i = \frac{4h}{3\pi a_c} \tag{3.11}$$

Given that achievable strains and strain rates depend on the radius and area function of the sphere, the time derivative of the strain channel (calculated from Equation 3.11) can be used to control strain rate. The indentation stress or hardness can be calculated using P/A_c.

However, using the strain channel requires a finite penetration depth, meaning that the rate must initially be controlled using a pseudo displacement-controlled method using a constant displacement rate. This is possible when the nanoindenter is equipped with a proportional-integral-derivative (PID) control device.

Thus for this initial loading stage of the test, a_c can be defined using[34]:

$$a_c = \sqrt{2Rh_c - {h_c}^2} \tag{3.12}$$

as opposed to Equation 3.9, which is based on the calibrated A_c. h_c can be arranged as a function of ε_i calculated with the user provided nominal tip radius R:

$$h_c = \frac{18\pi^2\varepsilon^2 R}{16+9\pi^2\varepsilon^2} \tag{3.13}$$

and used to achieve a user-defined initial strain ε. Differentiating with respect to time (where $\varepsilon(t) = \dot{\varepsilon}t$) gives displacement rate $\dot{h_c}$ as a function of strain rate $\dot{\varepsilon}$:

$$\frac{dh_c}{dt} = \dot{h_c} = \frac{576\pi^2 R\varepsilon\dot{\varepsilon}}{(16+9\pi^2\varepsilon^2)^2} \quad (3.14)$$

Once the initial strain has been achieved by loading at a specified initial displacement rate, the indenter switches from displacement-controlled to strain-rate controlled (using Equation 3.11). The test finishes once a user-defined total strain is achieved. This method was written by Dr Chris Hardie and edited with Dr Anna Kareer.

3.4.2 Nanoindentation Procedure

Nanoindentation was performed on an Agilent G200 Nanoindenter (shown in Figure 3.1) in CSM mode with a displacement amplitude 2 nm at 45 Hz. Spherical diamond tips with nominal radii of 5 µm and 10 µm were calibrated against fused silica (according to Equation 3.8). An initial strain of 0.02 was achieved at an initial displacement rate of 0.5 nm s^{-1}, before loading at a user-defined strain rate until a total strain of 0.1.

The effect of strain rate on indentation stress-strain behaviour was investigated by performing indents at strain rates of 3.2 x 10^{-5} s^{-1}, 3.2 x 10^{-4} s^{-1} and 3.2 x 10^{-3} s^{-1} (slow, medium and fast respectively) in unirradiated and neutron-irradiated single crystal tungsten, corresponding to the mid-points between orders of magnitude on a log scale. PID parameters were tuned in order to achieve these strain rates; conditions at which the variation in strain rate was minimal during each test are: P=0.5, I=0.001 and D=0.015. 9 indents were performed for each sample.

3.5 Atomic Force Microscopy

Atomic force microscopy (AFM) is a high-resolution technique commonly used to produce a topographic image.[91] The basic principle involves rastering an AFM probe with a sharp silicon tip over the sample surface. The tip can be in direct contact with the material (contact mode) or hovering

slightly above it with a small oscillation up and down near its resonant frequency (tapping mode). The sample is mounted onto a piezoelectric scanning stage which controls the vertical and lateral movements of the probe. The tip is attached to a flexible cantilever; the deflection of the cantilever changes as the tip moves across features of different height, and is tracked by a laser reflected from the back of the cantilever in the direction of a photodetector. A feedback signal controls the stage in order to keep the cantilever at a near-constant position, and thus, near-constant interaction force. The coordinates of the scan are used to generate a 3D topographic map of the surface.

A Dimension 3100 (Nanoscope IV) AFM (Veeco/Bruker) was used in contact mode to determine the surface morphology around nanoindents in both the unirradiated and neutron-irradiated single crystal tungsten samples.[91] The nominal radius of the silicon tip used was 8 nm. The raw data was analysed using Gwyddion, an open-source software for scanning probe microscopy data, enabling a topography map to be produced.[92] At fields of view larger than 10 μm in diameter, the curvature produced by the AFM system's arc-like cantilever motion is superimposed on the topography in the image produced. This artifact can be corrected by using software to perform a quadratic fit or other mathematical function and remove the resulting background without affecting the topographical results; a typical background curvature is shown in Figure 3.2. The 'Align rows' and 'Polynomial background removal' functions if Gwyddion were used to correct the scanning shifts and superimposed background curvature respectively. Spots due to surface contamination were also removed. Throughout this standard correction process, care was taken not to modify the shape of the indent pit or its surrounding pile-up by applying a mask to the central region of the micrographs.

In addition, Figure 3.3 shows an example of a typical surface profile measured using AFM. It is evident that there is asymmetry in the lobes surrounding the indenter trough, which could be a result of asymmetry in the indenter tip. Line profiles can be extracted from lines 1 and 2 on the image. Figure 3.4 shows the differences between the shapes of the profiles, indicating that it is not appropriate to average lines 1 and 2. Given that the tip and sample remained in the same orientation during both

nanoindentation and AFM experiments respectively, the line profiles in this thesis will be compared using a consistent direction (i.e. line 1) to avoid losing the integrity of the data.

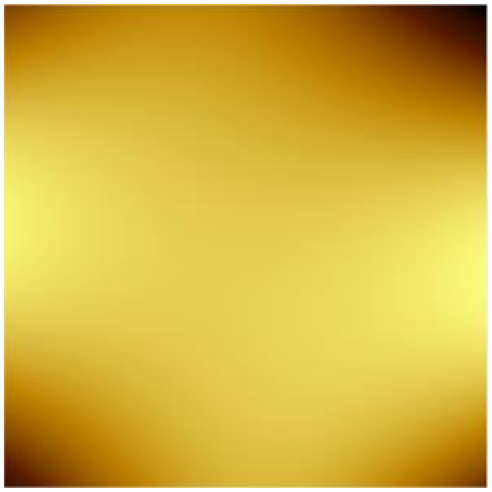


Figure 3.2: *Example of the background removed through a polynomial fit in the Gwyddion.*[92]

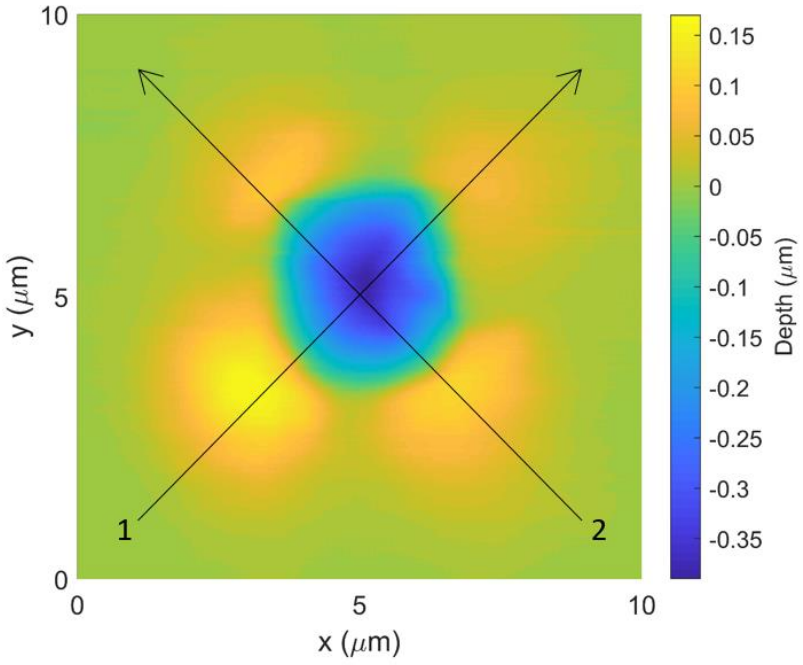


Figure 3.3: *Example of a typical AFM micrograph for an indent, showing asymmetry in the four lobes surrounding the indenter pit. Lines 1 and 2 denote the two directions in which line profiles were extracted from.*

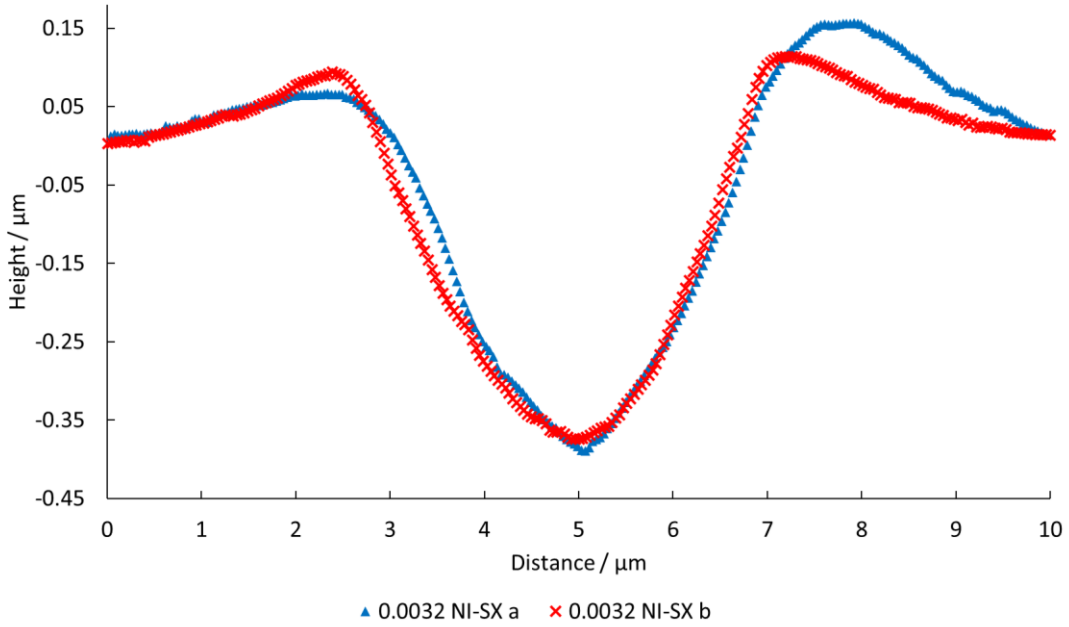


Figure 3.4: *Line profiles corresponding to the directions shown in Figure 3.3.*

3.6 Scanning Electron Microscopy

A scanning electron microscope (SEM) scans a focused beam of high-energy electrons over a surface to create an image. The electrons in the beam can interact with the sample at various depths, producing different signals that can be used to obtain information about the topography, chemical composition, and more with the combined use of advanced techniques such as electron backscatter diffraction (EBSD). Micrographs in this work were obtained using secondary electron (SE) imaging to capture topography and morphology in a Tescan MIRA3 XHM SEM.

3.7 High Resolution Electron Backscatter Diffraction

Electron backscatter diffraction (EBSD) is a powerful technique for analysing crystal structure and crystal orientation. The basic principle of EBSD inside a SEM involves rastering the electron beam across the surface of a highly-tilted (typically 70°) specimen, and scattered electrons which satisfy Bragg's law for a given crystal plane define two cones from the front and back surfaces of the plane. Dynamical diffraction leads to raised electron intensity in Kikuchi bands bounded the cones. The diffracted electrons are detected by a phosphor screen, and the resulting electron backscatter pattern

(EBSP) on the screen is comprised of Kikuchi bands corresponding to the family of crystal planes which caused the Bragg scattering. This pattern can be imaged using a charge-coupled device (CCD) camera and EBSD software can index the pattern for each point of interest and identify crystal orientation. A point-by-point series allows an orientation map to be created.

Recent developments in the analysis of EBSPs using image correlation methods have allowed the measurement of elastic strain with a sensitivity of ~ 10^{-4} rad.[93] This high resolution EBSD (HR-EBSD) technique involves measuring image shifts between a test EBSP and a reference pattern from a nominally strain-free region. These small shifts are related to elastic strains and lattice rotations through image processing based on cross-correlation analysis. Furthermore, lattice curvatures can be determined from the EBSD measurements, enabling the density of geometrically necessary dislocations (GNDs) to be determined. Measuring the distribution of GND density beneath indents can indicate the pattern of plastic deformation present. Figure 3.5 is an example of a typical EBSD setup. The backscattered electrons that impinge on the detector generate a diffraction pattern that consists of Kikuchi lines. Each point on the surface of the material gives rise to a unique pattern from which the orientation of the grain can be determined. A series of such measurements across the surface of the sample allows the creation of an EBSD orientation map.

A Tescan MIRA3 XHM SEM was used for this work. Initial experiments were conducted using a NordlysNano EBSD detector and AZtec 5.0 software (both Oxford Instruments, OI), before changing to an OI Symmetry S2 EBSD Detector (allowing for rapid indexing speeds and improved sensitivity) in combination with the same Aztec software. An accelerating voltage of 30 kV and beam current of 15 nA were used. EBSD maps were acquired using a 50 nm step size and 1x1 binning. Cross-correlation analysis was performed on data from HR-EBSD using the XEBSD code written by Britton and Wilkinson.[93,94,95] Although strains and rotations can be analysed successfully after a first pass, erroneously high strain calculations may be obtained beyond a misorientation of 2°; thus a second pass at cross-correlation was performed, providing robust solutions for rotations of up to 11°.

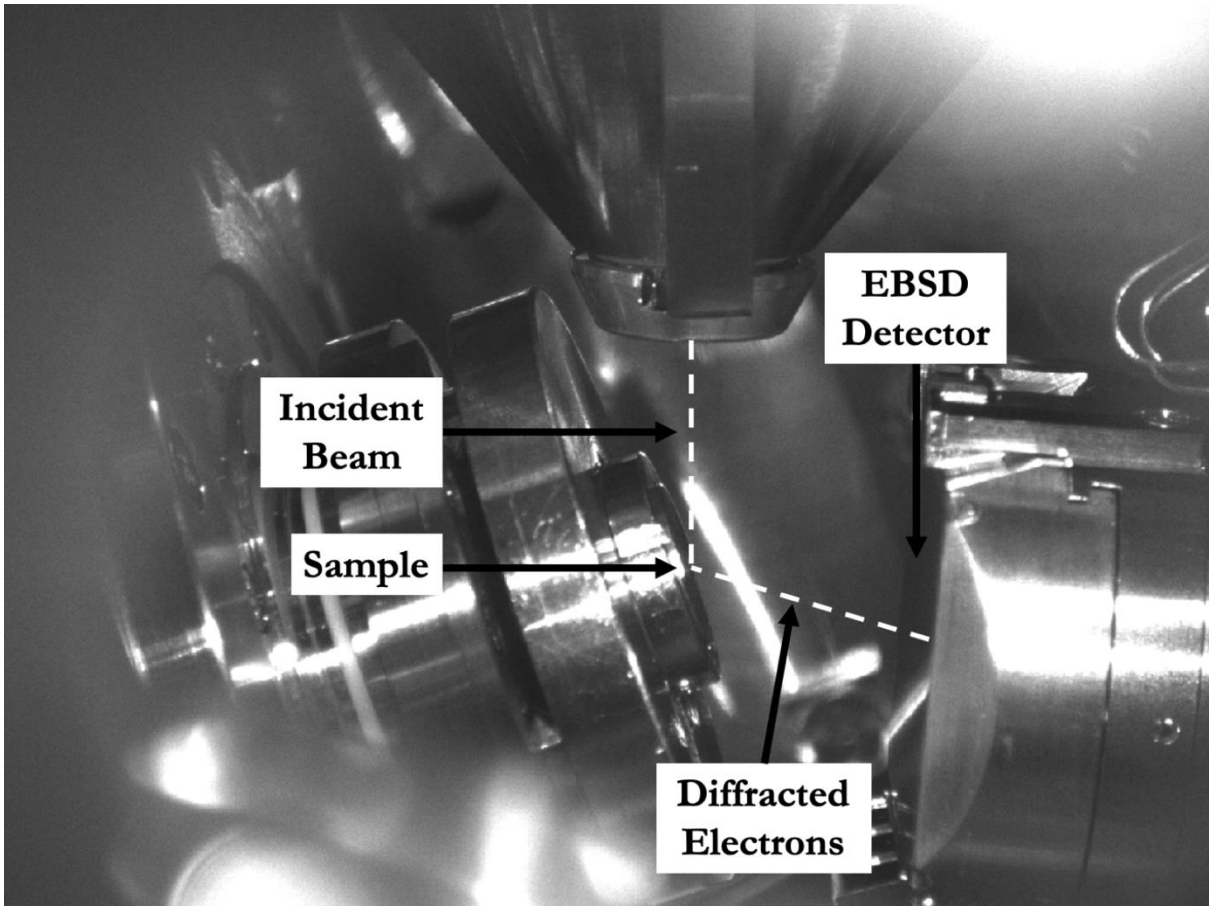


Figure 3.5: *A schematic of a typical EBSD setup with detector and sample.*

4 Investigating Strain Rate Effects in Neutron-Irradiated Tungsten

As discussed in the Literature Review, the deformation resistance of body-centred cubic (bcc) metals such as tungsten are strain-rate sensitive (Section 2.4). In this chapter, Berkovich and spherical nanoindentation experiments are reported for unirradiated single crystal tungsten (SX) and neutron-irradiated tungsten (NISX, with a final composition W - 1.20 ± 0.11 at.% Re - 0.11 ± 0.05 at.% Os - 0.03 ± 0.01 at.% Ta). The main aim is to determine the effect of neutron irradiation on the hardness and spherical indentation stress-strain response. In addition, the effect of strain rate and tip size on the resulting indentation stress strain (ISS) curves has been explored.

The nanoindentation results in this study can be interpreted alongside further mechanical and microstructural characterisation on the same irradiated sample as in this work, which has been performed by other authors from the Oxford Micromechanics Group. This includes nanoindentation strain-rate jump tests, microcantilever tests, four-point bend tests, Atom Probe Tomography (APT), Scanning Transmission Electron Microscopy (STEM), High Angle Annular Dark Field (HAADF) and High Resolution Transmission Electron Microscopy (HRTEM).[1,89,30,96,97]

The effect of strain rate and tip size on the resulting indentation plastic zone size in both samples is explored in Chapter 5 and discussed comprehensively alongside these ISS results in Chapter 7.

4.1 Berkovich Nanoindentation

Nanoindentation was performed with a Berkovich tip at a strain rate of 0.05 s^{-1} in unirradiated and neutron-irradiated single crystal tungsten. 9 tests were performed for each sample, and an average was taken across the results shown in this section. The total indentation depth for the tests was set to 2000 nm, which produced a maximum average load of 395 mN in the unirradiated sample and 575 mN in the irradiated sample, as shown in the average load-displacement curves in Figure 4.1. Figure 4.2 shows a magnified view of the load-displacement curves at smaller displacements than Figure 4.1,

but from single indents in the samples. There is a large pop-in at 50 nm displacement in the unirradiated sample, and ones of similar magnitude (~60 nm) can be observed in each test on this surface. The presence of pop-ins is often related to relieving the stress or elastic strain beneath the tip by nucleating or activating dislocations in the material, signifying the onset of plastic deformation.[98]

The indentation load at a given indentation depth was higher in the neutron-irradiated tungsten, thus producing a higher hardness measurement. The average hardness (from 250 – 500 nm) increased by 2.06 GPa following irradiation, from 6.04 ± 0.04 GPa in SX to 8.10 ± 0.15 GPa in NISX (Figure 4.3). The Berkovich indentation size effect (ISE), which exhibits as a decrease in hardness as indenter displacement increases, can be seen in both samples, although the depth dependence reduces at a depth of ~ 1 μm where the hardness reaches a stable value.[47] The hardness difference at 500 nm displacement (2.2 GPa) matches the differences of 2.2 GPa and 2.7 GPa previously reported by Abernethy *et al*.[1] and Lloyd *et al*.[96] respectively, using the same neutron-irradiated sample and a different unirradiated single crystal sample.

Figure 4.4 shows that the elastic modulus does not vary with depth, but appears to be higher in the irradiated material (441 ± 7.7 GPa vs 406 ± 2.2 GPa), although this is likely due to the increased pile-up following irradiation which was visible under the optical microscope, causing an underestimation of the projected contact area; this overestimation of the modulus (and hardness) can be accounted for by incorporating actual contact area measurements.

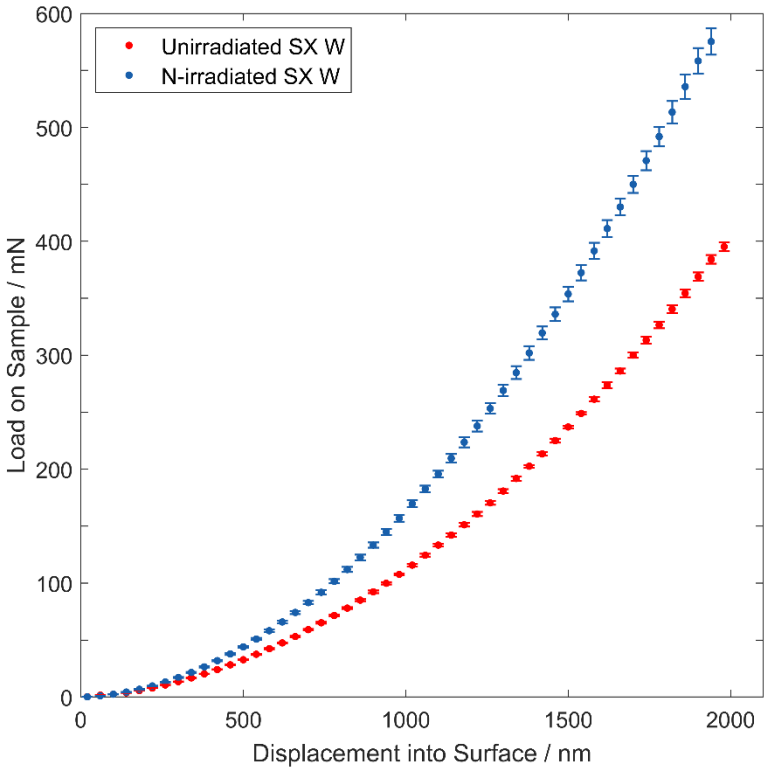


Figure 4.1: *Average load versus displacement into surface curves for Berkovich indentation in SX and NISX. Error bars show ± 1 standard deviation.*

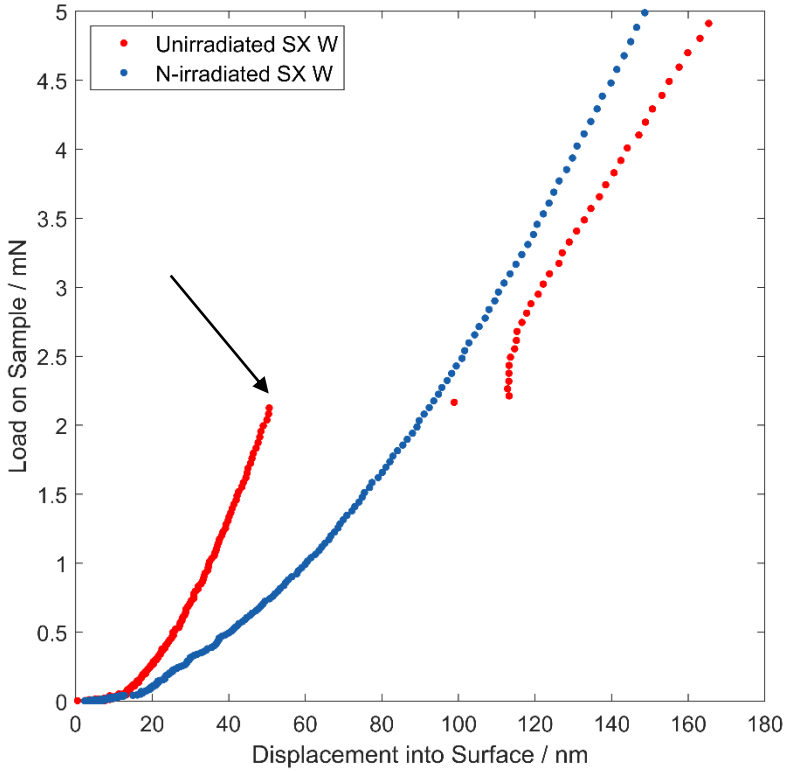


Figure 4.2: *Typical load–displacement data for SX and NISX; the black arrow indicates the pop-in event which took place in the unirradiated sample.*

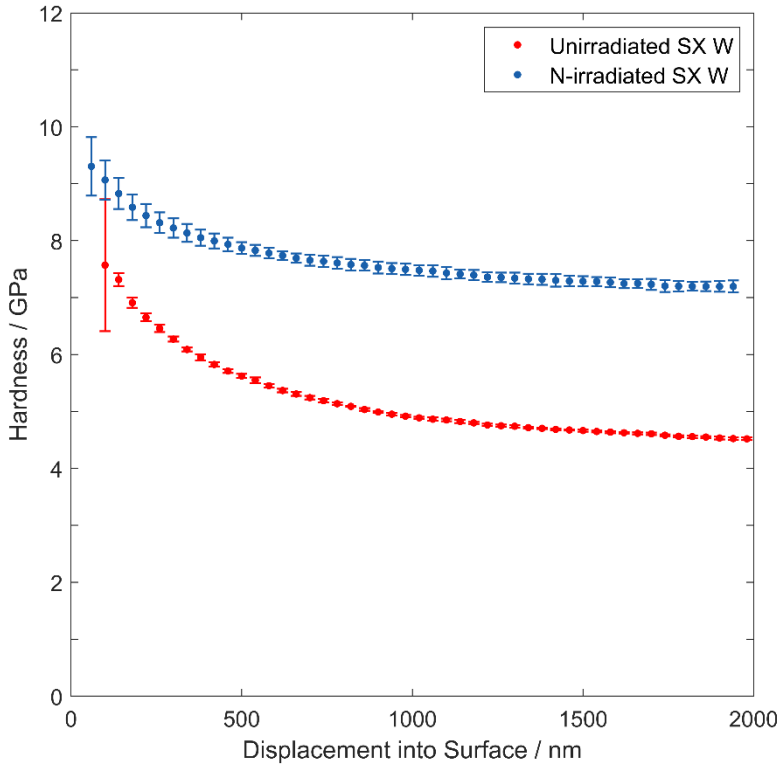


Figure 4.3: *Average hardness–displacement curves for SX and NISX. Error bars show ± 1 standard deviation.*

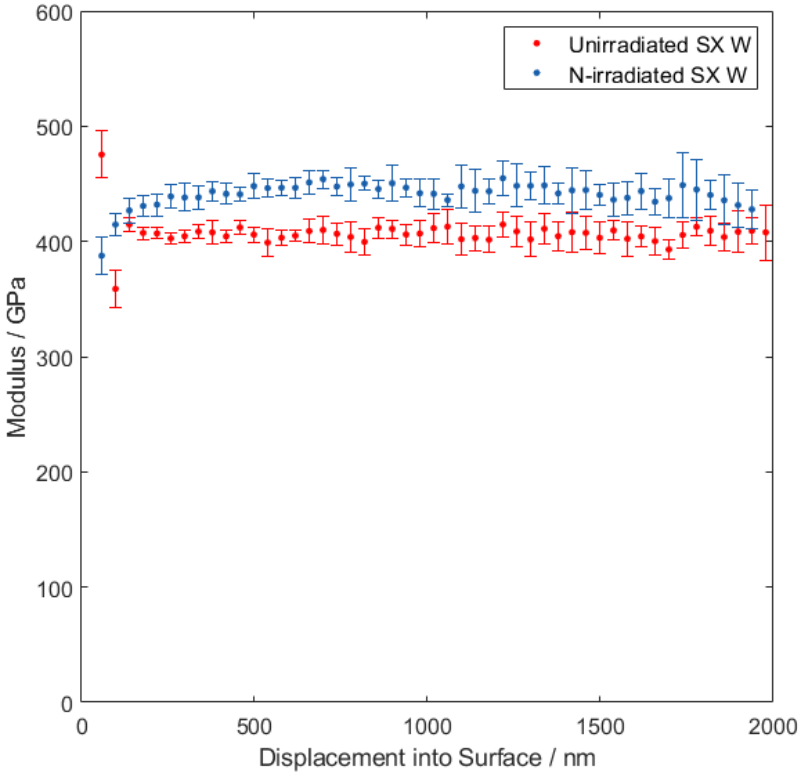


Figure 4.4: *Average modulus–displacement curves for SX and NISX. Error bars show ± 1 standard deviation.*

4.2 Spherical Nanoindentation

4.2.1 Tip Calibration

Two spherical tips with nominal radii of 5 µm and 10 µm were used to conduct the nanoindentation experiments reported in this thesis. Fabricating perfectly spherical tips using hard and stiff materials such as diamond is difficult due to their anisotropy. Although the deviations from a perfectly symmetrical sphere are usually small, they can cause a significant problem in reliably determining stress-strain curves from nanoindentation experiments.

As mentioned in 2.3.4, correct calibration of the tip shape is important in defining accurate contact areas to conduct constant strain-rate tests, particularly as the indentation strain is dependent on the displacement and contact radius according to the definition of used in this study (Equation 3.11, Section 3.4.1). Leitner *et al*.[58] used a novel method of tip calibration by calculating the area function of a sphere, allowing a constant strain rate to be calculated which accounts for imperfections. This is critical when producing indentation stress-strain curves since variations in strain rate can cause falsification of the work hardening behaviour observed in rate-sensitive materials such as bcc metals.

The tips in this study were calibrated by determining the geometric constants B_0, B_1 and B_2 in the tip area function defined in Equation 3.8,[58] enabling the change in radius with displacement to be calculated. These constants were varied and converged using a non-linear least square method (a Levenberg-Marquardt algorithm).[99,100] The nominal 5 µm and 10 µm tips were found to have radii of approximately 3.7 µm and 7.5 µm respectively, and the values of B_0, B_1 and B_2 were used for the strain-rate controlled segment of the experiment, as described in 3.4.1.

4.2.2 Zero Point Correction

The effective zero point of initial contact between the spherical indenter and sample surface can be determined by several methods when using a nanoindenter equipped with continuous stiffness measurement (CSM).[101,55] Using the default nanoindenter procedure, in which the point of initial contact is picked as the first data point after the stiffness signal exceeds a given value, can lead to poor

selection of the zero point, as shown in unrealistic looking stress-strain curves. This is because errors of even a few nanometres can have a major influence on the plots and calculations produced.

The method of zero-point correction used in this study was proposed by Moseson *et al*.,[101] whereby the indenter load and displacement are shifted to ensure a linear fit of the stiffness versus contact radius curve through the origin. This enables an effective zero point to be achieved had the surface been atomically flat and normal to the loading direction.

Establishing the zero point allows the production of reasonable looking nanoindentation stress-strain curves without spikes in the elastic loading portion of the curve which often arise from using the zero point calculated by the default procedures on the nanoindenter.

4.2.3 5 µm Tip

Spherical nanoindentation experiments were performed using a nominally 5 µm radius tip according to the method defined in Section 3.4.1 and 3.4.2 (using Equations 3.13 and 3.11). In this method, the nanoindenter switches from displacement-controlled (0.5 nm s^{-1}) to strain-controlled once a user-defined initial strain of 0.02 is reached. The test then continues by loading at a user-defined strain rate until a total strain of 0.1 is reached, allowing ISS curves to be produced.

The tests were performed on SX and NISX at slow, medium and fast strain rates (of 3.2 x 10^{-5} s^{-1}, 3.2 x 10^{-4} s^{-1} and 3.2 x 10^{-3} s^{-1} respectively) corresponding to the mid-points between orders of magnitude on a log scale.

In Figure 4.5 the load-displacement curves show the initiation of plasticity through displacement bursts in both materials, although the indentation load at a given indentation depth was higher in the neutron-irradiated sample following the large initial pop-ins in the unirradiated material. The maximum load was 53 mN in SX and 76 mN in NISX. Due to the presence of pop-ins in these 5 µm tests, the data presented for each sample are from single indents. The load-displacement curve for the unirradiated case shows a much larger pop-in (~ 50 nm) compared to the irradiated sample (~

10nm); both of these pop-ins are followed by a 'staircase' effect in the load, which is likely a result of the indenter control using the strain-rate controlled method.

There are small method artifacts in the magnified view of the graph in Figure 4.5 (b). In SX, there was a pop-in between the displacements of 62 – 116 nm. Prior to this, there was a slight increase in load at 13 nm relative to the near-linear region leading up to 62 nm. This region corresponds to the switch from displacement control to strain control (using Equation 3.11) at 0.02 strain, during which there was a drop in strain rate before returning to a near-linear increase of load with depth. There was also a minor artifact in the neutron-irradiated sample at ~ 15 nm, but in this case, the artifact immediately transitioned to a pop-in. These artifacts in the elastic deformation of the samples did not affect data after the pop-in.

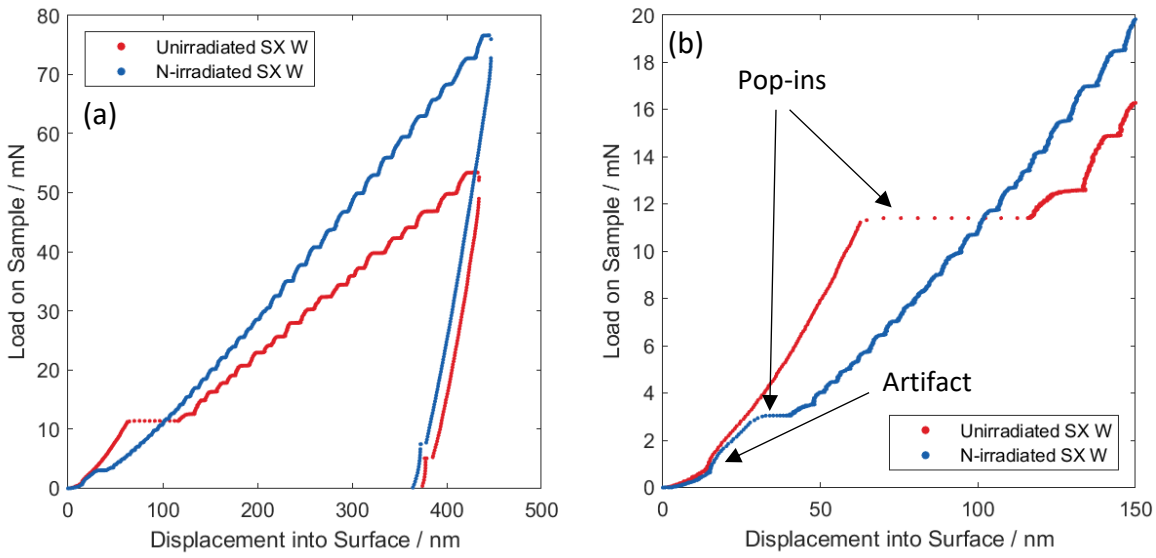


Figure 4.5: *(a) Typical load-displacement curves for unirradiated and neutron-irradiated single crystal tungsten at a strain rate of 3.2 x 10^{-4} s^{-1}. The graph in (b) shows a magnified view of the initial data.*

The contact radius increased in a near-linear manner during the pop-in as the test ran at the defined strain rate, followed by a segment in which the contact radius increased faster than the indentation depth after the pop-in, as previously reported by Pathak and Kalidindi.[56] This can be

correlated with a decrease in indentation stress and overall indentation strain (defined in Equation 3.11), producing the unloading segments of the graphs in Figure 4.6 following pop-ins.

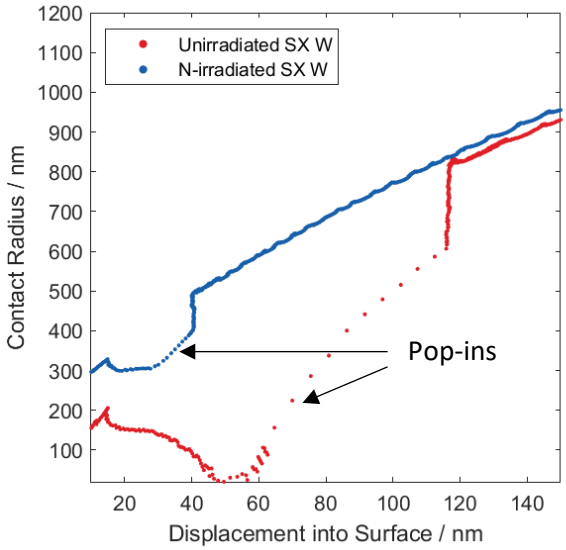


Figure 4.6: *Graph of contact radius (CSM signal) vs displacement in both samples at 3.2 x 10^{-4} s^{-1}.*

The ISS curves measured at decreasing strain rates in the unirradiated sample are shown across Figure 4.7 (a), (c), (e), with a representative curve from each strain rate shown in (g) due to the pop-in nature of spherical indents with small tips. The y-axis of the graphs in Figure 4.7 have been purposely selected to focus on the plastic flow behaviour rather than the peaks of the pop-ins, which are truncated in the plots. Each curve shows the presence of a pop-in, where a large increase in the elastic stress is observed, but there is no significant strain hardening behaviour following each pop-in.

The ISS curves calculated at different strain rates in the neutron-irradiated sample can be seen in Figure 4.7 (b), (d), (f), with a representative curve from each strain rate displayed in (h) for comparison. Across the three strain rates, there is slightly more scatter in the indentation stresses compared to the unirradiated sample, although pop-ins are more similar in size and smaller.

Although linear functions commonly used to examine strain hardening were not appropriate for the ISS curves presented, given the presence of pop-ins and non-uniform nature of the deformation, hardness values were determined from the ISS curves at 8 % strain (shown in Table 4.1) for direct comparison with the measurements made using a Berkovich tip in Section 4.1. The increase in

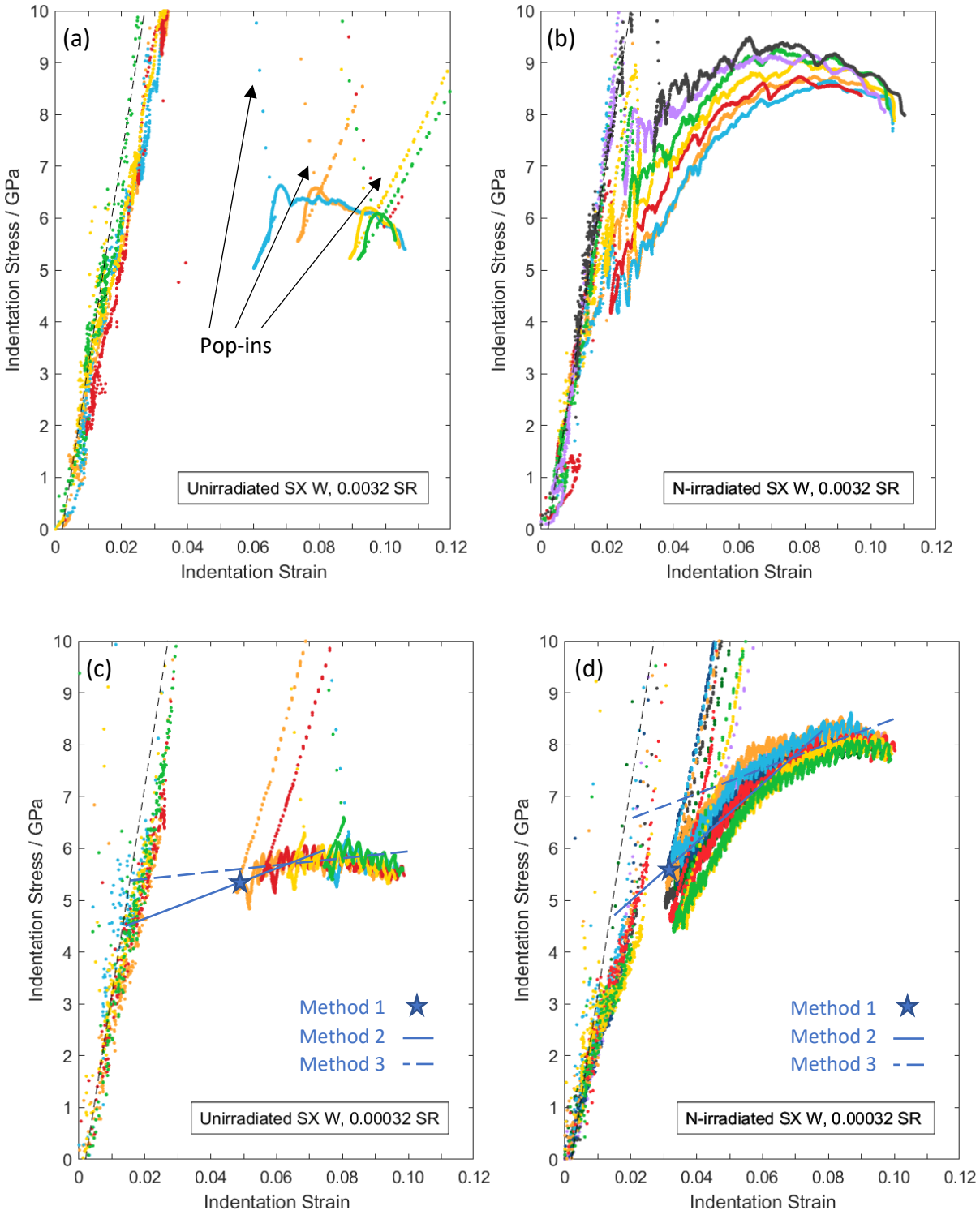
hardness after irradiation at the slow, medium and fast strain rates was 31 % (1.53 GPa), 33 % (1.99 GPa) and 40 % (2.44 GPa) respectively.

Table 4.1: *Hardness values for both SX and NISX at slow, medium and fast strain rates calculated at a strain of 8 % strain for comparison with Berkovich nanoindentation.*

Indentation strain rate / s^{-1}	Sample	Hardness / GPa	Standard deviation / GPa
3.2×10^{-5}	Unirradiated	4.92	0.057
3.2×10^{-4}	Unirradiated	5.97	0.259
3.2×10^{-3}	Unirradiated	6.13	0.099
3.2×10^{-5}	N-irradiated	6.45	0.216
3.2×10^{-4}	N-irradiated	7.96	0.270
3.2×10^{-3}	N-irradiated	8.57	0.273

The lack of plastic data until displacements after pop-ins did not allow the yield point to be inferred from the point at which the elastic Hertzian response intersects with a straight line through the flow portion of the curve, as described in the work of Zhu *et al*.[43] The yield stress (YS) of each nanoindentation curve was therefore extracted from the ISS curves using the following three methods, as denoted in Figure 4.7 (c) and (d):

- **Method 1:** YS from the first point after the pop-in
- **Method 2:** YS from the intersection of the 0.2% offset elastic Hertzian response with the line from linear back-extrapolation of the hardening portion of the flow curve (excluding softening), after the pop-in if present [56,57]
- **Method 3:** YS from intersection of the 0.2% offset elastic Hertzian response with a line of best fit straight line through the entire flow portion of the ISS curve [43]


(a)
Pop-ins
Unirradiated SX W, 0.0032 SR
Indentation Stress / GPa
Indentation Strain
(b)
N-irradiated SX W, 0.0032 SR
Indentation Stress / GPa
Indentation Strain
(c)
Method 1
Method 2
Method 3
Unirradiated SX W, 0.00032 SR
Indentation Stress / GPa
Indentation Strain
(d)
Method 1
Method 2
Method 3
N-irradiated SX W, 0.00032 SR
Indentation Stress / GPa
Indentation Strain

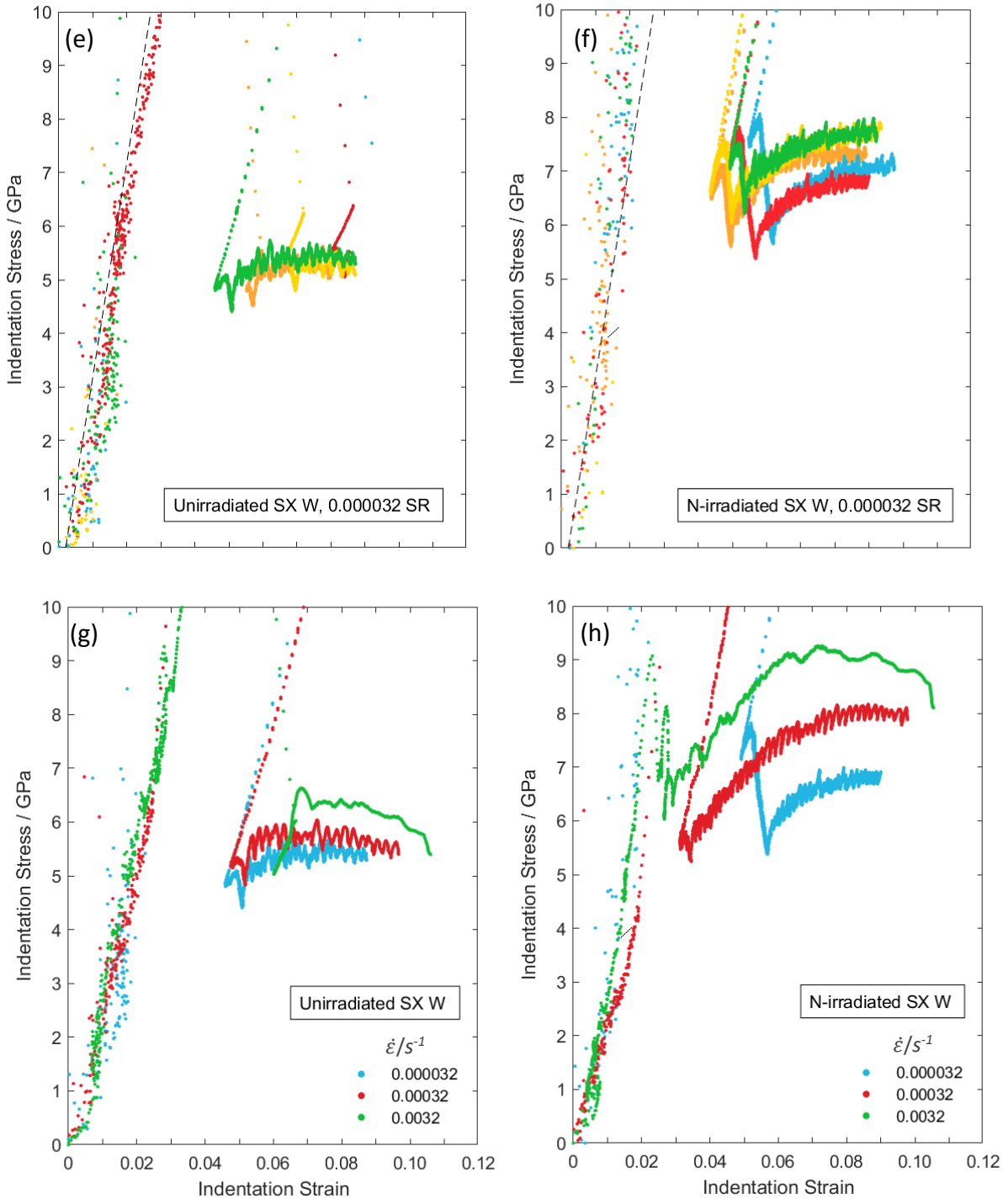


Figure 4.7: *Spherical indentation stress-strain curves with a 5 µm radius indenter in unirradiated single crystal tungsten (a, c, e) and neutron-irradiated single crystal tungsten (b, d, f) at strain rates of 3.2 x 10^{-3} s^{-1}, 3.2 x 10^{-4} s^{-1} and 3.2 x 10^{-5} s^{-1} respectively. Graphs (g) and (h) show a comparison of typical stress-strain curves at varying strain rates in both materials.*

Multiple analysis methods were used due to the difference in ISS curve shape for SX and NISX, as well as the presence of pop-ins in both materials, manifested as strain bursts followed by elastic unloading. The Hertzian elastic response is almost identical for data in both samples from all three strain rates. The YS values are shown in Table 4.2 and displayed graphically in Figure 4.8.

Table 4.2: *Yield stress data from indentation stress-strain curves conducted with a 5 µm radius spherical tip at different strain rates, calculated using the three methods described in Section 4.2.3.*

	Average yield stress (Method 1) / GPa	Average yield stress (Method 2) / GPa	Average yield stress (Method 3) / GPa
Unirradiated 3.2 x 10^{-3} s^{-1}	5.58 ± 0.17	5.64 ± 0.06	5.66 ± 0.06
Unirradiated 3.2 x 10^{-4} s^{-1}	5.20 ± 0.17	4.55 ± 0.07	5.32 ± 0.15
Unirradiated 3.2 x 10^{-5} s^{-1}	4.83 ± 0.20	4.22 ± 0.08	4.51 ± 0.16
N-irradiated 3.2 x 10^{-3} s^{-1}	6.02 ± 0.90	5.70 ± 0.91	8.23 ± 0.22
N-irradiated 3.2 x 10^{-4} s^{-1}	5.52 ± 0.53	4.75 ± 0.30	6.46 ± 0.28
N-irradiated 3.2 x 10^{-5} s^{-1}	5.84 ± 0.35	4.46 ± 0.17	5.74 ± 0.30

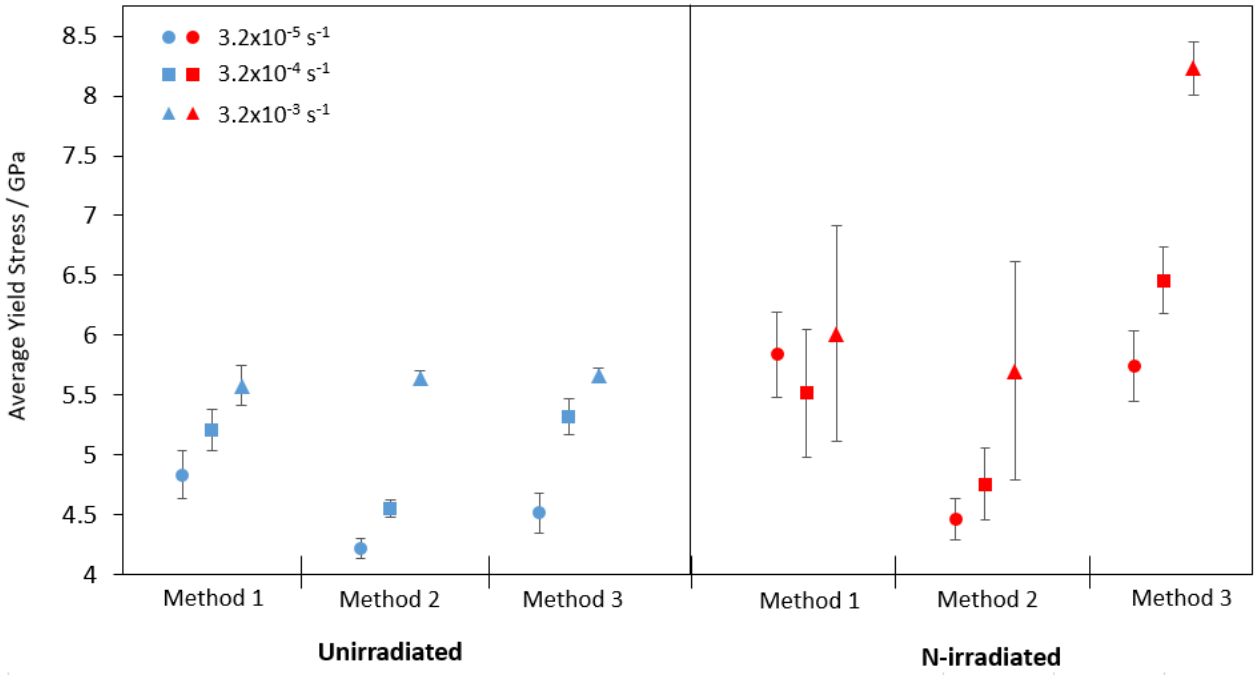


Figure 4.8: *Average yield stresses from Table 4.2 extracted from the ISS curves in Figure 4.6 using the three yield stress analysis methods. Average values were calculated from between 4 – 9 successful indents as shown in Figure 4.7. Error bars show ± 1 standard deviation.*

There is a decrease in the stresses measured in the flow portion of ISS response as the strain rate is decreased across the three figures respectively, and this is reflected in the average YS calculated using Method 3 (5.66 ± 0.06 GPa, 5.32 ± 0.15 and 4.51 ± 0.16 GPa) as displayed in Table 4.2 and Figure 4.8. For each strain rate, some of the curves exhibit larger pop-ins than others, resulting in minimal flow data succeeding the pop-in, particularly at the slowest strain rate of 3.2×10^{-5} s^{-1}.

As observed in the unirradiated sample, the YS results from NISX using all three methods of analysis clearly demonstrate that a higher YS is measured with increasing strain rate (shown in Figure 4.8). The ISS curves from the irradiated samples also showed much greater strain hardening than their unirradiated counterparts after pop-in, specifically between 0.02 and 0.07 strain, followed by saturation and a slight softening. The irradiated sample also yielded a higher average YS from Methods 1 and 2 than the unirradiated sample, with a significantly higher YS calculated using Method 3 due to the line of best fit being shifted to fit much higher indentation stress values in the irradiated sample.

The YS values from Methods 2 and 3 are comparable in the unirradiated sample where there is little strain hardening, whereas in the irradiated sample, the average YS from Method 3 is significantly higher than from Method 2, since the curves display great strain hardening.

4.2.4 10 µm Tip

Spherical nanoindentation tests were performed with a 10 µm tip using the method described in Section 3.4.1 and 3.4.2. Typical load-displacement curves for these tests are shown in Figure 4.9. In the unirradiated tungsten, a series of pop-ins starting at ~ 40 nm occurs. The 'staircase' effect in load due to machine control observed in Figure 4.5 in the 5 µm results is also present in the 10 µm data. The maximum loads for the two samples are 162 mN and 258 mN respectively.

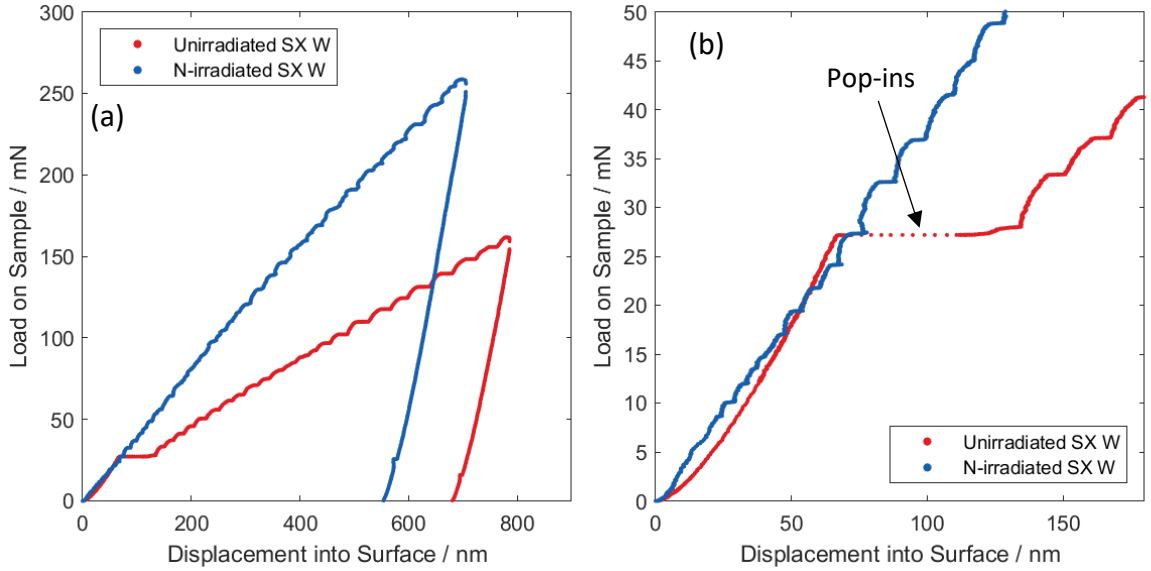


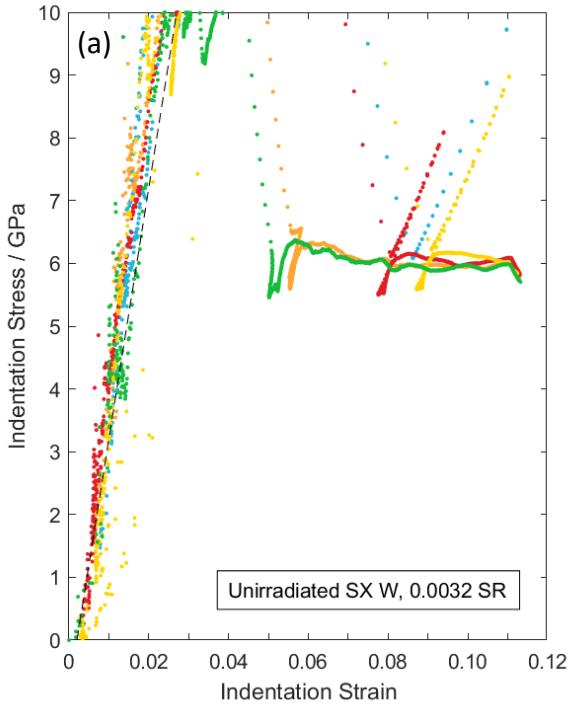
Figure 4.9: *(a) Typical load-displacement curves for unirradiated single crystal tungsten and neutron-irradiated single crystal tungsten at a strain rate of 3.2 x 10^{-4} s^{-1}. The graph in (b) shows a magnified view; in the unirradiated sample, a large pop-in followed by small pop-in events, whilst an artifact in machine control can be observed in the irradiated sample prior to a series of small pop-ins.*

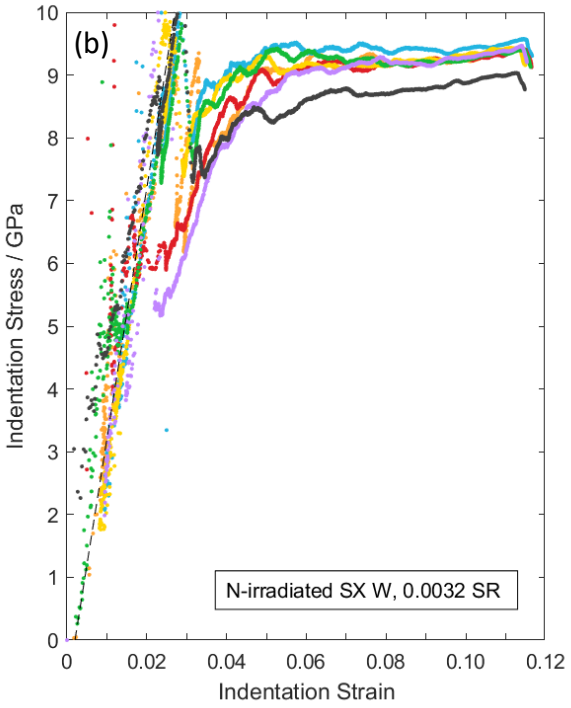
The three methods of YS analysis used for data from the 5 µm radius tip described in Section 4.2.3, and demonstrated in Figure 4.7 (c) and (d), were also used for this set of data because of the different stress-strain curves exhibited by the unirradiated and neutron-irradiated samples, in addition to the lack of plastic data preceding the pop-ins in the unirradiated sample. The YS data are shown in Table 4.3 and graphically in Figure 4.11.

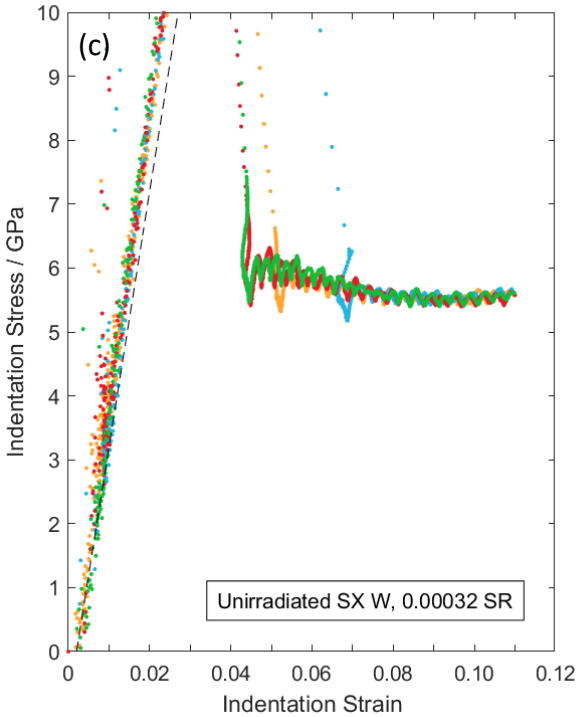
The indentation stress-strain (ISS) curves measured at decreasing strain rates in the unirradiated sample can be seen across Figure 4.10 (a), (c), (e), with a representative curve from each strain rate displayed in (g) due to the pop-in nature of spherical indents with small tips. Note that the y-axis of

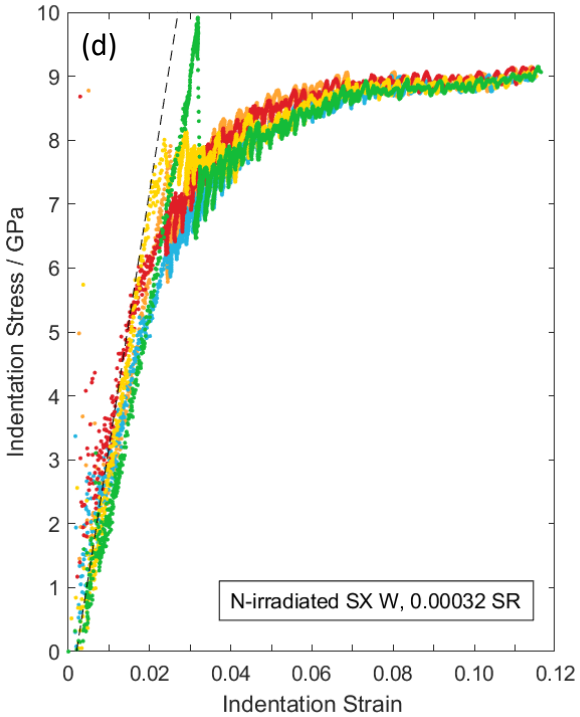
the graphs in Figure 4.10 have been chosen to emphasize the plastic flow behaviour instead of the peaks of the pop-ins. Each of the curves shows the presence of a pop-in, although there is variation in its size shown by curves measured at the same strain rate. No strain hardening behaviour is observed following each pop-in, yielding comparable YS values from Methods 2 and 3. The stress in the plastic flow region of the curves decreases with strain rate across the three figures respectively, as reflected in the average YS calculated using Method 3 (5.71 ± 0.23 GPa, 5.47 ± 0.16 and 4.85 ± 0.11 GPa).

The ISS curves calculated at different strain rates in the neutron-irradiated sample can be seen in Figure 4.10 (b), (d), (f), with a representative curve from each strain rate displayed in (h) for comparison. There is slightly more scatter in the indentation stresses compared to the unirradiated sample, although the size of the pop-ins are much smaller in the neutron-irradiated sample. The effect of pop-ins is barely visible in the ISS curve at the lowest strain rate. As demonstrated in the unirradiated sample, a higher YS is measured with increasing strain rate. The ISS curves from the irradiated sample show significant strain hardening between 0.02 and 0.05 strain, with an increase in indentation stress after the elastic region and/or pop-in, followed by a plateau region. The irradiated sample also yielded a slightly higher average YS from Methods 1 and 2 than the unirradiated sample (0.3 – 1 GPa). This difference increases to 2 – 3 GPa using Method 3, which is likely a result of the increased flow stress in the irradiated sample. The increase in YS measured using Method 2 can be attributed to the large gradient in stress at early strains where there is limited to no data for the unirradiated material. Generally, a greater YS difference is observed between the two samples with an increase in strain rate.


(a)
Indentation Stress / GPa
Indentation Strain
Unirradiated SX W, 0.0032 SR


(b)
Indentation Stress / GPa
Indentation Strain
N-irradiated SX W, 0.0032 SR


(c)
Indentation Stress / GPa
Indentation Strain
Unirradiated SX W, 0.00032 SR


(d)
Indentation Stress / GPa
Indentation Strain
N-irradiated SX W, 0.00032 SR

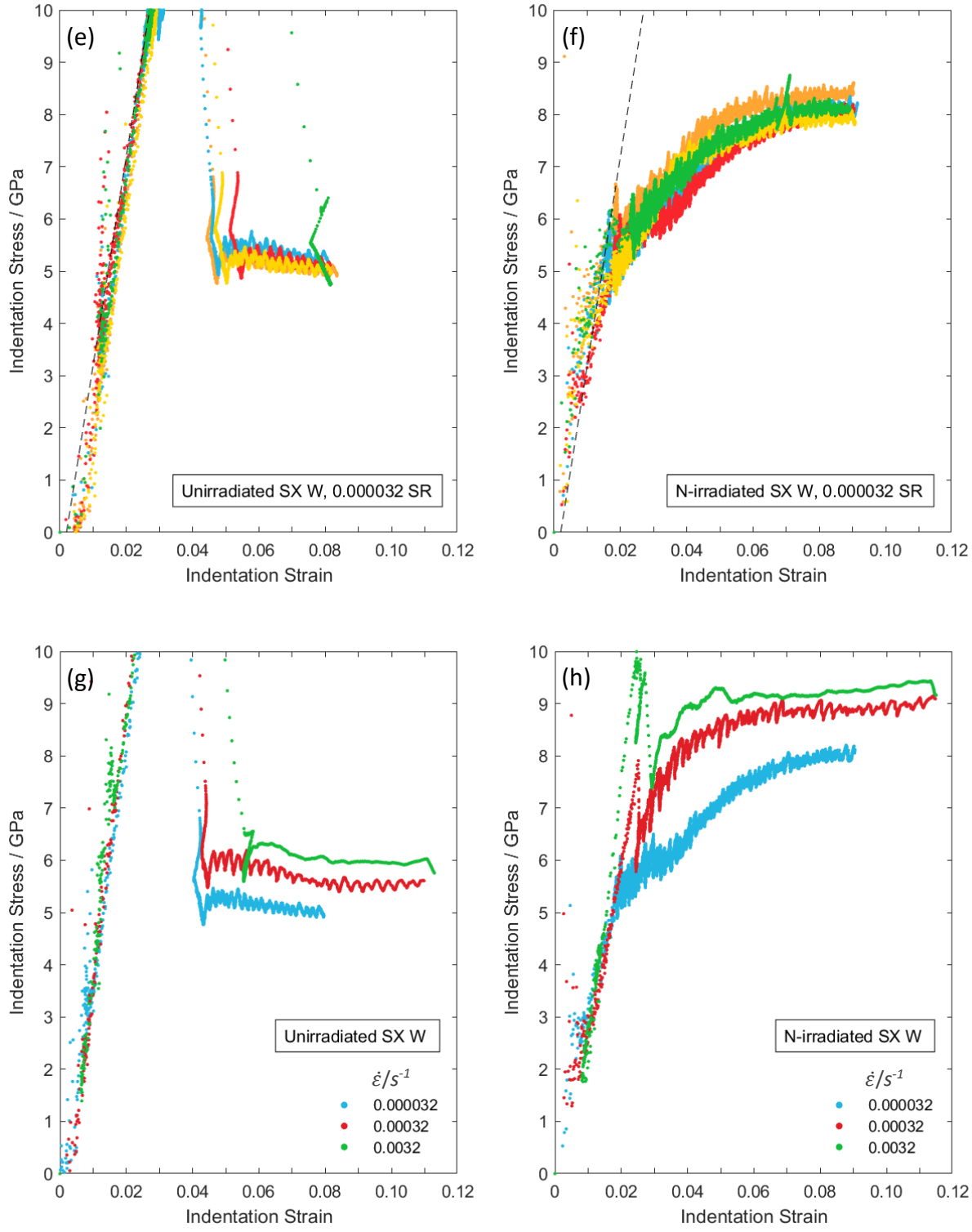


Figure 4.10: *Spherical indentation stress-strain curves with a 10 µm radius indenter in unirradiated single crystal tungsten (a, c, e) and neutron-irradiated single crystal tungsten (b, d, f) at strain rates of of 3.2 x 10^{-3} s^{-1}, 3.2 x 10^{-4} s^{-1} and 3.2 x 10^{-5} s^{-1} respectively. Graphs (g) and (h) show a comparison of typical stress-strain curves at varying strain rates in both materials.*

Table 4.3: *Yield stress data from indentation stress-strain curves conducted with a 10 µm radius spherical tip at different strain rates, calculated using the three methods described in Section 4.2.3.*

	Average yield stress (Method 1) / GPa	Average yield stress (Method 2) / GPa	Average yield stress (Method 3) / GPa
Unirradiated 3.2 x 10^{-3} s^{-1}	5.71 ± 0.23	5.84 ± 0.15	5.99 ± 0.09
Unirradiated 3.2 x 10^{-4} s^{-1}	5.47 ± 0.16	5.51 ± 0.09	5.51 ± 0.09
Unirradiated 3.2 x 10^{-5} s^{-1}	4.85 ± 0.11	4.90 ± 0.05	5.02 ± 0.13
N-irradiated 3.2 x 10^{-3} s^{-1}	6.86 ± 0.62	6.75 ± 0.58	9.14 ± 0.22
N-irradiated 3.2 x 10^{-4} s^{-1}	6.18 ± 0.36	6.41 ± 0.36	8.75 ± 0.11
N-irradiated 3.2 x 10^{-5} s^{-1}	5.17 ± 0.28	5.22 ± 0.26	8.11 ± 0.16

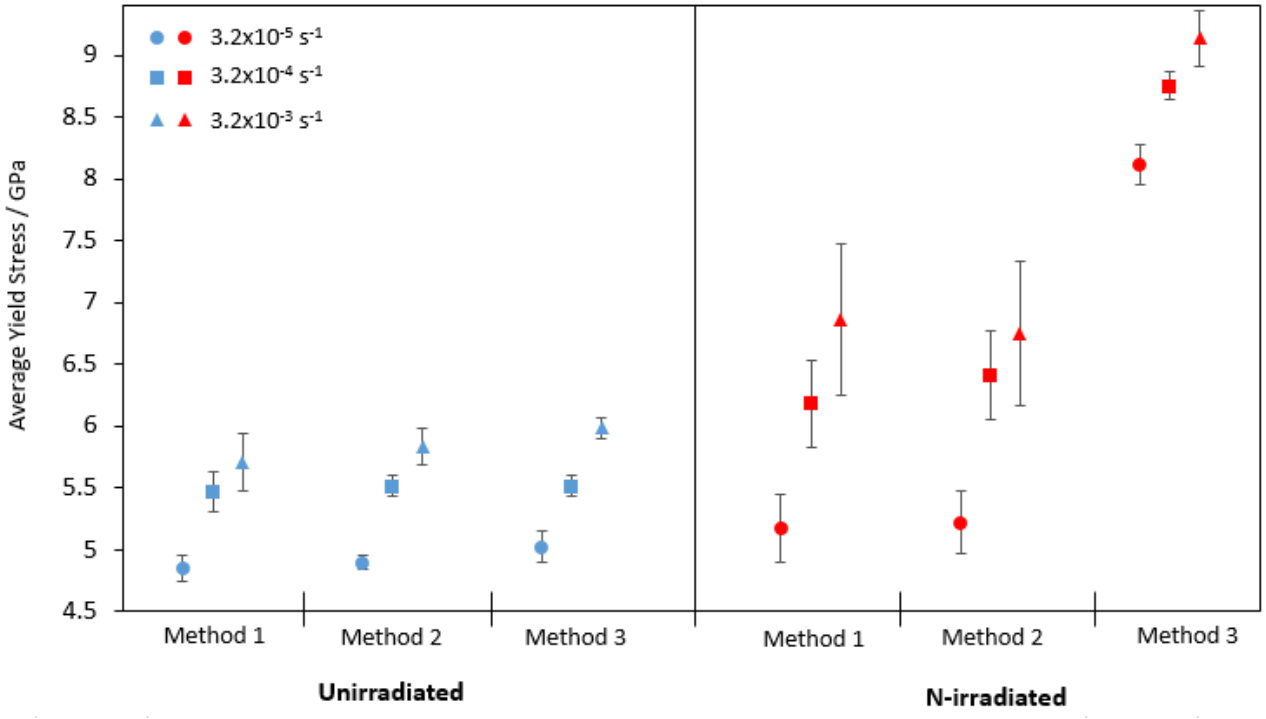


Figure 4.11: *Average yield stresses from Table 4.3 (extracted from the ISS curves in Figure 4.10 using the three yield stress analysis methods detailed in Section 4.2.3). Average values were calculated from between 4 – 7 successful indents as shown in Figure 4.10. Error bars show ± 1 standard deviation.*

Hardness values were calculated from the ISS curves shown in Figure 4.10 at 8 % strain (shown in Table 4.4) for direct comparison with the measurements made using a Berkovich tip in Section 4.2.1. The increase in hardness after irradiation at the slow, medium and fast strain rates was 48 % (2.41 GPa), 56% (3.03 GPa) and 56 % (3.22 GPa) respectively.

Table 4.4: *Hardness values for both SX and NISX at slow, medium and fast strain rates calculated at a strain of 8 % strain for comparison with Berkovich nanoindentation.*

Indentation strain rate / s^{-1}	Sample	Hardness / GPa	Standard deviation / GPa
3.2×10^{-5}	Unirradiated	4.99	0.083
3.2×10^{-4}	Unirradiated	5.41	0.062
3.2×10^{-3}	Unirradiated	5.79	0.099
3.2×10^{-5}	N-irradiated	7.40	0.162
3.2×10^{-4}	N-irradiated	8.44	0.068
3.2×10^{-3}	N-irradiated	9.01	0.092

4.3 Discussion

A combination of Berkovich and spherical nanoindentation has been used to better understand the effect of strain rates on the mechanical response of single crystal tungsten and neutron-irradiated single crystal tungsten (final composition W - 1.20 ± 0.11 at.% Re - 0.11 ± 0.05 at.% Os - 0.03 ± 0.01 at.% Ta). As described in Section 3.2, the irradiated sample was bombarded by neutrons as part of the Extremat-II campaign in 2008.[30,76,89]

Berkovich indentation is used to probe the hardness and modulus of the unirradiated and neutron-irradiated tungsten samples. A self-similar indenter produces a constant averaged plastic strain of typically 7 – 8 % across the test volume (Section 2.3.3) whilst introducing variations in strain over shorter distances for shallow indents. The Nix-Gao strain gradient model widely used to explain the ISE is based on the assumption that the volume of material displaced by the indenter at the surface is accommodated by the presence of geometrically-necessary dislocations (GNDs), in addition to the statistically stored dislocations (SSDs) usually produced during uniform straining. This results in an extra hardening component which becomes larger with a decrease in depth.[47,42]

Spherical nanoindentation is employed to produce indentation stress-strain (ISS) curves as a surrogate for uniaxial testing, of which a significant benefit is the gradual transition from the activation

of elastic to plastic deformation in a manner analogous to a uniaxial test. However, given the differences in the deformation processes, the indentation stress has been used to generate representative stress-strain curves (instead of converting indentation hardness measurements to uniaxial yield stresses), and there is a change in average strain over the course of each test as the contact radius increases with penetration depth. The stress field generated within the small volume of material under the indenter enables the investigation of how strain rate, irradiation and tip size affect the ISS response of the samples. In some cases, the much smaller test volume compared to tensile tests also means that discrete dislocation level pop-in events are seen rather than a gradual smooth transition between elastic to plastic deformation.

Another limitation of spherical nanoindentation is the difficulty in ensuring successful indenter-sample contact. Initial contact is highly sensitive to tip curvature, surface topology, velocity of indenter approach, friction between the indenter and sample surface, amongst other influences, causing difficulties in efficient data collection. As a result, over a third of the tests conducted on the two samples failed to run subsequent to poor surface contact.

There were also difficulties in extracting yield stress (YS) values arising from large pop-ins, particularly in the unirradiated sample, as well as differences in work hardening between the two samples, meaning that several evaluation methods were required. Similar difficulties in determining the YS from tungsten using small spherical tips have been reported in literature, requiring the comparison of several indentation strength measurements along the ISS curve.[57] The three methods of YS extraction described in 4.2.3 and Figure 4.7 (c) were selected to accommodate for tests during which large pop-ins have obscured reliable determination of the yield point from the curve. This has enabled consistency in the comparison of results between different tip sizes, work hardening rates, and pop-in sizes, resulting in relatively small standard deviations with respect to measurements and providing a high level of confidence in the measurements made.

Representative stress-strain curves from spherical nanoindentation have been compared to the true stress-strain curves produced by uniaxial tests in literature. Leitner *et al*. matched curves of bcc Cr and W (amongst other metals) from spherical indentation to micropillar compression tests by using constraint factors to convert indentation hardness to stress.[58] Using a constant constraint factor of 2.8 as per Tabor's approach led to underestimation of the yield and overestimation of work hardening, whereas a strong likeness was achieved using a variable constraint factor based on four different deformation regimes. Similarly, Chang *et al*. compared true stress-strain curves from macroscopic tensile tests to indentation stress-strain curves (using constraint factors) in a variety of materials;[102] the authors also concluded that there was significant deviation between the representative stress-strain curves and the true stress-strain curves, particularly in the initial portion of the curve for materials with a longer elastic-plastic transition.

Durst *et al*. found that polycrystal Ni exhibits a macroscopic behaviour using a spherical tip of 51 μm, and that the indentation response could be successfully modelled by incorporating macroscopic stress–strain data from either Tabor's approach or finite element simulations. However, with smaller tips and their associated pop-ins, Tabor's continuum concept for the elastic–plastic transition is no longer valid.[60] However, the hardness after pop-in can be modelled using Taylor's dislocation hardening approach, thus a combined Tabor and Taylor approach can enable modelling of the size dependence of hardness.

Given that the ISS curves shown in this study are produced from tips less than 10 μm in radius, their physical shape is not directly analagous to true stress–strain curves from macroscopic uniaxial tests. Nonetheless, the results do indicate that spherical indentation can be successfully used to examine elastic loading and hardening behaviour, in addition to generating yield stress values despite the presence of pop-ins. It is worth highlighting that the use of tips larger than 10 μm could allow a more simple procedure for extracting yield stresses and further information on the elastic-plastic transition behaviour.

4.3.1 Effect of Strain Rate

Unirradiated and neutron-irradiated single crystal tungsten were tested using nominally 5 µm and 10 µm tips at strain rates of 3.2 x 10^{-3} s^{-1}, 3.2 x 10^{-4} s^{-1} and 3.2 x 10^{-5} s^{-1} (Figure 4.7 and Figure 4.10). Using the spherical tip calibration and experimental method described in Sections 4.2.1 and 3.4, a true constant strain rate was achieved for the majority of each test reported in this work; slight deviations arose from the presence of both pop-ins and a minor method artifact which was visible only in the 5 µm tip results (Figure 4.5 (b)).[58,55]

The results from both tips consistently show that there is a rate dependence in both samples, manifested as an increase in hardening or yield stress with strain rate, regardless of which YS analysis method was used. The increase in hardness measured with the 5 µm tip at 8 % strain for comparison with Berkovich indentation after irradiation was 31 % (1.53 GPa), 33 % (1.99 GPa) and 40 % (2.44 GPa) respectively at the slow, medium and fast strain rates. Using the 10 µm tip, the increase in hardness after irradiation at the slow, medium and fast strain rates was 48 % (2.41 GPa), 56% (3.03 GPa) and 55 % (3.22 GPa) respectively.

Furthermore, Figure 4.7 (g, h) and Figure 4.10 (g, h) demonstrate that although the curves are shifted to higher indentation stresses at faster strain rates, the shape of the ISS curves remains the same for each sample. This indicates that the work hardening behaviour remains consistent as a function of strain when strain rate is controlled properly.

The effect of strain rate on yield stress highlights the importance of reporting strain rates when producing stress-strain curves from nanoindentation in order to provide an accurate representation of the mechanical properties. Additionally, robust spherical tip calibration and potential tuning of the nanoindenter's proportional-integral-derivative (PID) device is needed to maintain the correct strain rate for spherical tips, instead of using the standard pyramidal strain-rate profiles on nanoindenters.

The evolution of plastic deformation must therefore be determined from rate-controlled tests in spherical indentation, particularly in rate-sensitive materials such as tungsten. Maintaining a near-

constant indentation strain rate can be achieved by controlling the radius and area function of the sphere, and using the time derivative of the resulting indentation strain, such as in this study (described in Section 3.4.1). Single crystal tungsten in particular has a higher strain rate sensitivity than ultra-fine grained tungsten at room temperature arising from the thermally activated slip motion of screw dislocations, which are controlled via the kink-pair mechanism.[72,70] It is important to note that the fastest spherical indentation strain rate used in this work was 3.2 x 10^{-3} s^{-1}, but strain rates of up to 3 s^{-1} for disruptions and 8 s^{-1} for ELMs are predicted inside the DEMO reactor.[5] The limitations in indenter control using the G200 Nanoindenter in this study are evident at the fastest strain rate of 3.2 x 10^{-3} s^{-1}, for which greater margins of error in the ISS and thus yield stress results can be observed.

Interestingly, Abernethy *et al*. reported similar values of strain rate sensitivity using Berkovich nanoindentation strain-rate jump (SRJ) tests for both single crystal tungsten and neutron-irradiated single crystal tungsten samples (0.038 and 0.030 respectively), with the latter being the same neutron-irradiated specimen examined in this study.[76] The corresponding activation volumes for dislocation motion were 4.6 b^3 and 5.6 b^3, despite the inclusion of transmutation elements in the irradiated sample. These values have been demonstrated to indicate that kink-pair formation is the controlling mechanism for the brittle-ductile transition both before and after irradiation.

The hardness results given in Table 4.1 and Table 4.4 for SX and NISX for both tip sizes were analysed using Equations 2.5 and 2.6 to determine the spherical nanoindentation strain rate sensitivity (SRS), *m*, and activation volume, *V*, which is normalised by unit volume b^3 where *b* is the Burgers vector of W (0.274 nm). A graph of hardness vs strain rate is displayed in Figure 4.12, with an error of one standard deviation shown for each data point. A plot of log hardness ($\ln H$) vs log strain rate ($\ln \dot{\varepsilon}$) is shown in Figure 4.13, with the gradient being equal to *m*; the resulting values of *m* and *V* are displayed in Table 4.5. The error (Δ) in $\ln H$ (defined as $\frac{\Delta H}{H}$ given $\Delta H \ll H$) ranges from 0.011 to 0.043 using the 5 µm tip, and 0.008 to 0.021 using the 10 µm tip. $\Delta \ln H$ was used to plot the maximum and minimum gradients of *m* and calculate its uncertainty, which is equal to the difference between the maximum

and minimum gradients divided by 2. Table 4.5 also shows the Root Mean Square Errors (RMSEs) which measure the fit of the data to the regression lines used to estimate *m*. Although the resulting error in *m* is not large, there is clearly deviation from the gradients, with significant scatter demonstrated in the 5 µm tip data. As described at the start of Section 4.3, over a third of the tests conducted failed due to poor surface contact; therefore, whilst the values reported in this study agree well with literature, further testing would improve the statistical robustness in the values of *m*, and thus *V*, and clarify whether the observed discrepancies between the two tips is valid. The percentage uncertainty in *V* was calculated by combining uncertainties in both *m* and *H*, as per Equation 2.6.

In the unirradiated sample, *m* is 0.0477 and 0.0324 for the 5 µm and 10 µm tips respectively using constant strain rate tests, which is comparable to the value reported by Abernethy *et al* (0.038).[76] It is important to note that constant strain rate (CSR) nanoindentation experiments are also understood to exhibit significantly higher SRS than results than those obtained by the SRJ test.[74] In NISX, the value of *m* is 0.0616 and 0.0427 for the 5 µm and 10 µm tips respectively; the decrease in sensitivity with tip size (also seen in the unirradiated case above) indicates the presence of an indentation size effect.

Overall, the measured SRS using the 5 µm tip is in strong agreement with values reported for CSR tests on single crystal W with $\{001\}$ surface orientation ion-irradiated to 2 dpa by 6.4 MeV Fe^{3+} ions at 573 K by Hasenhuetl *et al.;*[103] dislocation loops of interstitial type were identified as obsstacles to dislocation motion. their values of *m* were 0.0425 and 0.060 before and after irradiation respectively, reflecting the high lattice friction in bcc materials at room temperature whereby deformation is controlled by the motion of screw dislocations.[71]

In this work, the reduction in *V* after irradiation from 3.65 b^3 to 2.12 b^3 for the 5 µm tip, and 5.93 b^3 to 2.89 b^3 for the 10 µm tip, indicates that the thermally-activated movement of kinks is affected by the radiation-induced microstructural obstacles such as dislocations and voids in NISX. The 5 results agree with the decrease in *V* from 5.6 b^3 to 4.6 b^3 published in Abernethy *et al*.'s study comparing the same irradiated sample in this study with a different unirradiated single crystal W sample.[76]

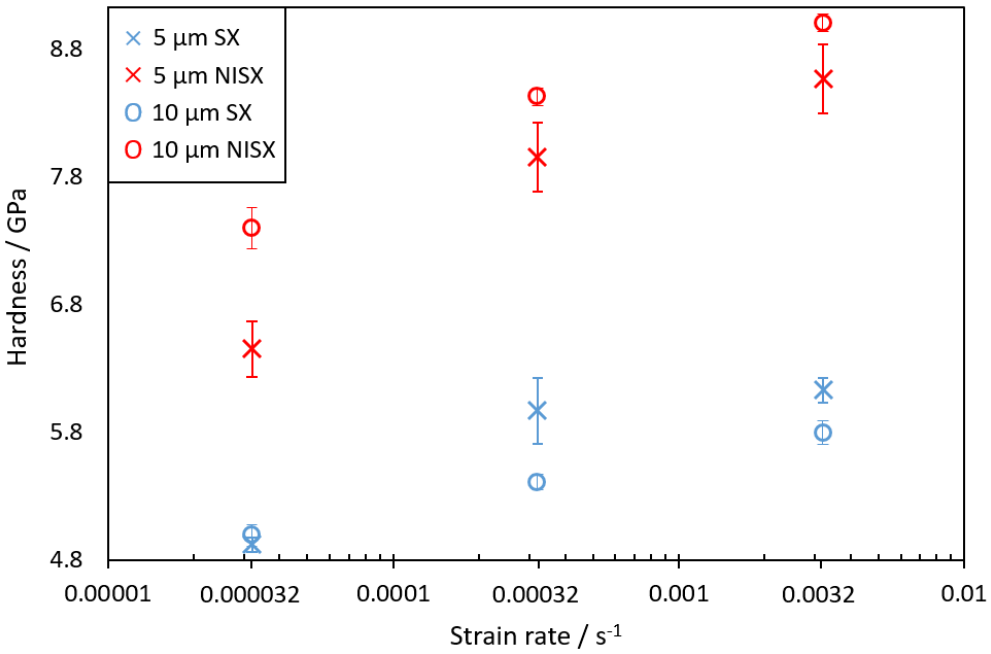


Figure 4.12: *Graph of hardness vs indentation strain rate (on a log scale) for both 5 µm and 10 µm radius spherical indents in unirradiated single crystal tungsten (SX) and neutron-irradiated single crystal tungsten (NISX) at 3.2 x 10^{-3} s^{-1}, 3.2 x 10^{-4} s^{-1} and 3.2 x 10^{-5} s^{-1}. Hardness values were calculated at 0.08 strain for comparison with the constant strain of ~ 8 % during Berkovich nanoindentation. Average values were calculated from between 4 – 9 successful indents as shown in Figure 4.7 and Figure 4.10. Error bars show ± 1 standard deviation.*

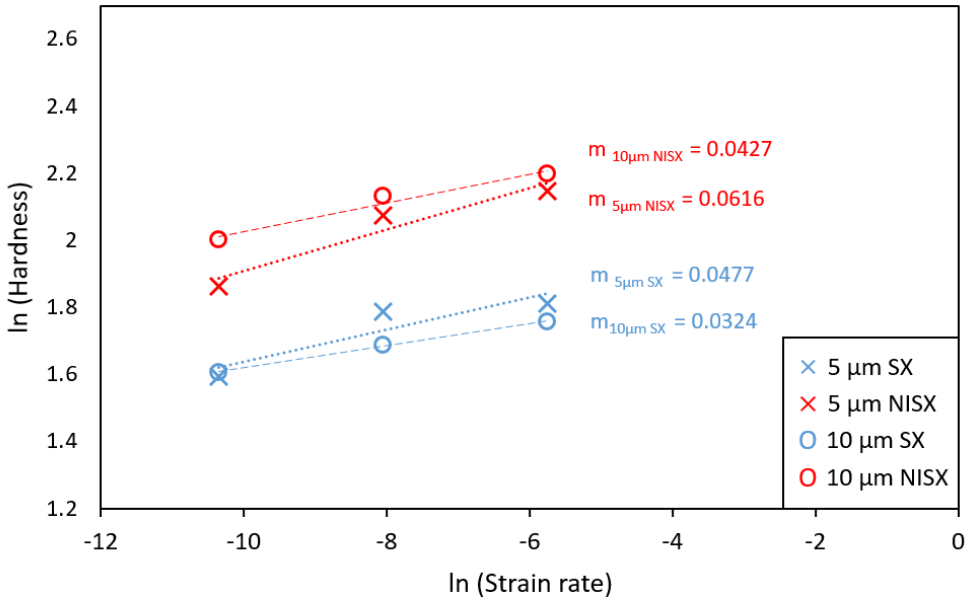


Figure 4.13: *Graph of log hardness vs log strain for 5 µm and 10 µm radius spherical tip indents in SX and NISX at strain rates of 3.2 x 10^{-3} s^{-1}, 3.2 x 10^{-4} s^{-1} and 3.2 x 10^{-5} s^{-1}. m is the strain-rate sensitivity.*

Likewise, the 5 µm results are in strong agreement with the respective activation volumes of 3.5 b^3 and 2.5 b^3 for unirradiated and ion-irradiated tungsten reported by Hasenhuetl *et al.*[103] Although the damage mechanisms in by neutron and ion irradiation are not directly comparable – for example,

the microstructures produced by ion beams contain much fewer voids than those produced by neutrons,[30] and there are no Re/Os clusters due to the lack of transmutation – there is strong alignment between the values of *m* and *V* obtained from this study and by Hasenhuetl *et al*. The similarity in results could be due to the slight increase in damage level and the presence of dislocation loops in the latter study. Nonetheless, this result demonstrates the value in using ion irradiation as a materials selection tool for irradiation environments, given that it provides a strong indication of the mechanical property changes arising from neutron irradiation at similar damage levels.

Table 4.5: *Spherical nanoindentation strain-rate sensitivity, m, and activation volume, V, calculated for both SX and NISX using 5 µm and 10 µm radius spherical tips for constant strain rate tests. The hardness for each material and tip condition was taken from the medium strain rate of 3.2 x 10^{-4} s^{-1}.*

Nominal tip size / µm	Sample	m	Root mean square error (RMSE) in m	V / m^3	V / b^3
5	Unirradiated	0.0477 ± 0.006	0.039	7.51 x 10^{-29} ± 17%	3.65
5	N-irradiated	0.0616 ± 0.014	0.032	4.36 x 10^{-29} ± 26%	2.12
10	Unirradiated	0.0324 ± 0.007	0.003	1.22 x 10^{-29} ± 23%	5.93
10	N-irradiated	0.0427± 0.006	0.015	5.93 x 10^{-29} ± 16%	2.89

4.3.2 Effect of Irradiation

The results in Sections 4.1 and 4.2 show that radiation-induced hardening is exhibited in the single crystal tungsten following neutron irradiation. The Berkovich nanoindentation results show a 2.06 GPa increase in hardness after irradiation between 250 – 500 nm, or a 2.2 GPa difference at 500 nm which matches the value reported using the same irradiated sample reported by Abernethy *et al*. at the same depth;[76] this is also comparable to other hardening results observed in neutron irradiated single crystal tungsten at similar temperatures.[104,96]

The Berkovich ISE was slightly less pronounced in the irradiated sample due to a smaller internal length scale caused by radiation-induced defects. It should be noted that the hardening from neutron irradiation is studied in single crystal W, which has a reduced hardness compared to polycrystalline W samples which often have a higher dislocation density. The lack of grain boundaries and dislocations

in the single crystal cause a deficiency of sinks for the radiation-induced defects, resulting in higher irradiation hardening than polycrystalline sheets and bars which contain grain boundaries and pre-existing dislocations; these provide effective defect sinks for trapping and recombination.[105]

The spherical indentation hardness values calculated at 8 % strain (Table 4.1 and Table 4.4) show a clear hardness increase after irradiation to 1.67 dpa at 900 °C in the HFR at Petten, ranging from 1.53 – 2.44 GPa (31 – 40 % hardening) for the 5 µm radius tip, and 2.41 – 3.22 GPa (48 – 55 % hardening) for the 10 µm radius tip, as the strain rate was increased from 3.2×10^{-5} s^{-1} to 3.2×10^{-3} s^{-1}. Das *et al.* reported a similar hardness increase of 13 % measured with a spherical indenter of ~ 5 µm radius, in self-ion irradiated tungsten to a damage level of 1 dpa; indentation was performed in grains with a surface normal of ⟨001⟩, although is it not clear which strain rate the tests were performed at.[88]

In addition to supporting Abernethy *et al.*'s Berkovich results on the same irradiated sample,[76] the Berkovich SX and NISX hardness measurements performed in this study at 5.0×10^{-2} s^{-1} (6.04 GPa and 8.10 GPa respectively) match the 5 µm tip spherical hardness results from 3.2×10^{-4} s^{-1} most closely (5.97 GPa and 7.96 GPa correspondingly). Conversely, the 3.34 GPa increase seen in tungsten following neutron irradiation to 1.54 dpa at 750 °C reported by Tanno *et al.*[106] matches mostly closely with the 3.22 GPa hardening observed using the 10 µm tip at the fastest strain rate of 3.2×10^{-3} s^{-1} in this study.

Interestingly, Hu *et al.* measured a significantly higher difference in hardening (5.78 GPa) in single crystal W neutron-irradiated to 1.62 dpa in the High Flux Isotope Reactor (HFIR), USA.[107] Large voids, dislocation loops, W-Re-Os precipitates were observed, which act as strong barriers to dislocation motion and dominate the radiation-induced hardening in the material.

This discrepancy could be a result of Tanno *et al.*'s irradiation being performed in JOYO in Japan, a fast test reactor, which suppresses transmutation compared to HFIR;[106] in addition, the observed irradiation defect microstructures only consisted of dislocation loops and voids, and not W-Re-Os precipitates. Neutron energy spectra can vary between different reactors and experiments, with the neutron energy spectrum from fission reactors such as the HFIR containing a high fraction of thermal

neutrons,[108] causing a greater ratio of transmutation products to damage (in dpa) than one would expect in a fusion reactor such as DEMO. This is due to the presence of 14 MeV neutrons, which have a lower capture cross section than thermal neutrons.[109] Large needle-shaped Re/Os precipitates of up to several hundred nanometers long have also been observed in W irradiated in the HFIR,[110] compared with the W-Re-Os precipitates in this study's sample, NISX, being 10-20 nm in size.[96] The Re content is also ~ 10 at. % Re compared to 1.2 at. % Re in this sample (detailed in Section 3.2).

The spherical ISS curves show that the irradiated sample exhibits a much higher indentation YS than the unirradiated one across all three evaluation methods, in addition to higher hardening rates. The curves obtained from both tips in the irradiated sample, displayed in Figure 4.14, show significant strain hardening behaviour between 0.02 and 0.06 strain, manifested as a large increase in indentation stress (~ 1.5 – 2.5 GPa) after the elastic region, or pop-in if present. This is followed by slight softening behaviour at 0.08 strain in the 5 µm tip curves, or a plateau region around 0.06 – 0.08 strain in the 10 µm tip curves where a saturation stress is achieved. The difference in the ISS curve shape between tip sizes is contrasting to the matching hardness-strain profiles reported for tip radii of 10 µm, 20 µm and 50 µm in nanocrystalline nickel.[58]

The observed change from work hardening to softening could be due to the formation of dislocation channels with reduced obstacle concentration, as previously reported in other neutron-irradiated bcc metals such as vanadium.[87,111] These cleared channels provide a means for dislocation movement with reduced obstacles, causing a loss of strain hardening.[112] In contrast, the plastic region after the large pop-in in the unirradiated sample is very flat and shows little to no work hardening. The pop-ins are much smaller in the irradiated sample for both tip sizes compared to the unirradiated tungsten, although they are still present in the 5 µm tip results (discussed further in Section 4.3.3).

The maximum indentation stresses for both tips at 3.2 x 10^{-4} s^{-1} are displayed in Table 4.6. These results are in strong agreement with the average Berkovich hardness values of 6.04 GPa in the unirradiated tungsten and 8.10 GPa in the irradiated tungsten measured at 5.0 x 10^{-2} s^{-1} (Section 4.1).

The lack of work hardening seen in the ISS curves for the unirradiated tungsten (Figure 4.14) is expected due to its high purity and lack of defects to inhibit dislocation glide. In addition, the absence of grain boundaries and dislocations combined with the highly anisotropic nature of the sample can result in dislocations punching out in specific crystallographic directions with little to no interaction; plastic zone sizes in single crystal tungsten have been found to range between 10 – 40 times the size of the contact radius.[113]

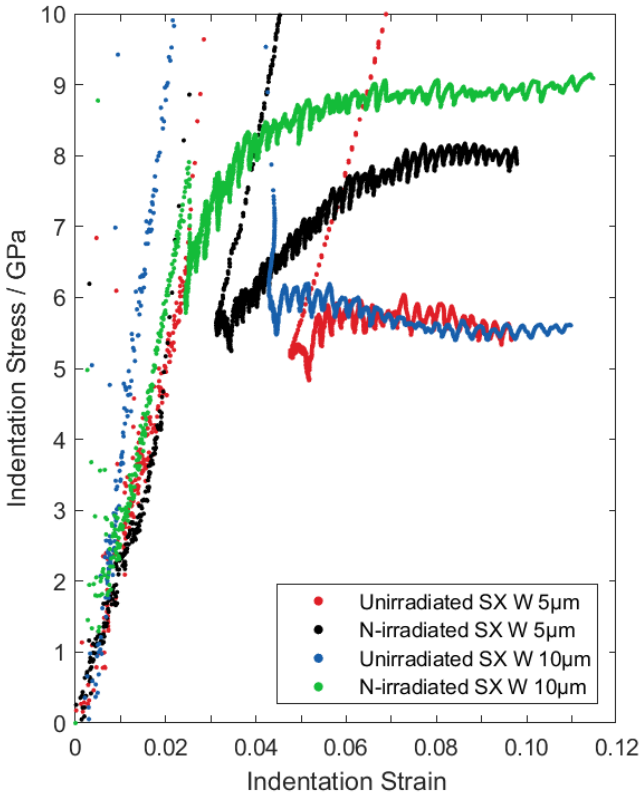


Figure 4.14: *Spherical stress-strain curves for unirradiated single crystal tungsten and neutron-irradiated single crystal tungsten tested with 5 µm tip and 10 µm tips at strain rates of 3.2 x 10^{-4} s^{-1}.*

Table 4.6: *Maximum indentation stress values from ISS curves for both 5 µm and 10 µm radius spherical tips at 3.2 x 10^{-4} s^{-1} in unirradiated and neutron-irradiated single crystal tungsten.*

Nominal tip size / µm	Sample	Maximum indentation stress / GPa
5	Unirradiated	5.7
5	N-irradiated	8.0
10	Unirradiated	6.0
10	N-irradiated	8.9

The ISS curves for the 5 μm tip (calibrated as 3.7 μm) in the unirradiated sample agree well (in terms of shape, pop-in and plastic flow stresses) with the 1 μm[57] and 1.4 μm[56] spherical tip ISS curves reported in electropolished annealed polycrystalline tungsten. Pathak and Kalidindi also highlighted the significant effect of surface finish on nanoindentation results in their work.[56] Preparation using electropolishing is more likely to cause pop-ins, whereas rough mechanical polishing will reduce the occurrence of pop-ins but increase the dislocation density content in the surface of the sample, which produces indentation data from a microstructure that is not representative of the bulk material. Vibro-polishing is seemingly advantageous in producing ISS curves as it introduces only a small amount of dislocations, but they are sufficient to suppress pop-ins and the resulting discontinuity so that the yield stress can be extracted simply and reliably. These observations are consistent with the unirradiated and neutron-irradiated tungsten results in this study, demonstrating that samples with low initial dislocation densities are more susceptible to pop-ins.

The increased YS and strain hardening behaviour in the irradiated sample is consistent with the findings of radiation-induced microstructural defects such as dislocations and voids caused by neutrons (see Section 2.2.3.3).[108,105] Furthermore, in this neutron-irradiated tungsten sample, the microstructure has been observed by APT to contain large voids of ~ 8 nm in diameter which are decorated by Re and Os (demonstrated in Figure 4.15);[30,104] these act as strong barriers to dislocation motion and dominate the radiation-induced hardening in the material.[107] The clusters are comprised of a central Re- and Os-rich core surrounded by a diffuse cloud of Re atoms. Since the Re forms prior to Os in the transmutation process and the analysis was performed after irradiation, it is currently unknown whether the Os is formed inside the Re clusters or transported from the bulk of the material. Nonetheless, the radiation defects provide dislocation sources for activation without the requirement for pop-ins, which are often attributed to dislocation nucleation and mobility.[56] Thus, as soon as a sufficient number of plastic deformation sources are activated, the ISS response of the material returns to the expected curve if pop-ins had not been present.

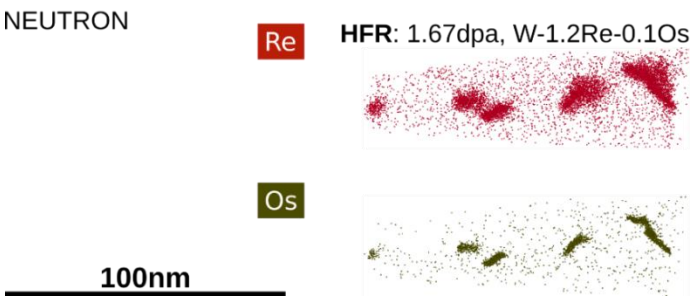


Figure 4.15: *Re and Os atom maps from APT reconstructions of the neutron-irradiated tungsten sample, showing Re atoms as red spheres of radius 0.1 nm and Os atoms as green spheres of 0.1 nm.*[96]

The ISS curves from the neutron-irradiated tungsten are comparable to the stress-strain results obtained from microcantilever beams made in another single crystal sample irradiated in the same Extremat-II campaign and tested using nanoindentation;[97] cantilevers 2B and 3A in Figure 4.16 were loaded to fracture, and the shape of the curve and saturation stresses are comparable to those reported from this work (8.0 – 8.9 GPa reported in Table 4.6), although the definition of strain was determined by cantilever deflection in this case.

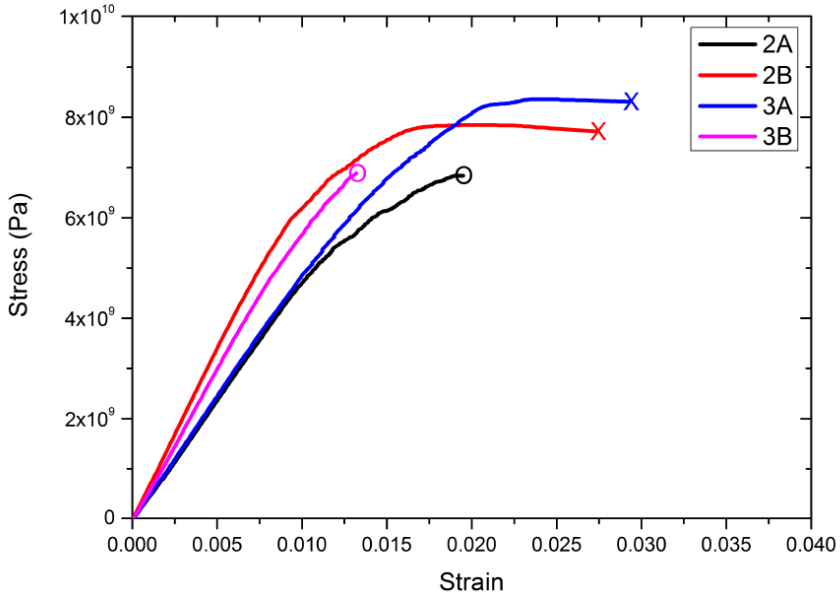


Figure 4.16: *Stress-strain curves from four cantilever beams tested in another neutron-irradiated tungsten sample from the same Extremat-II campaign, calculated using simple beam theory. Beams 2B and 3A fractured (marked with an X) whilst the other two tests were stopped early (marked with an O). The curves for the fractured beams show a significant degree of plastic deformation before fracture occurred.*[97]

At the time of writing, comparison with literature from other spherical ISS stress-strain data sets in neutron-irradiated tungsten is not possible. However, the hardening behaviour and flow stresses from the neutron-irradiated sample in this study (using a strain rate of 3.2 x 10^{-4} s^{-1} and 3.7 µm-

calibrated tip) are comparable with ISS results in He-implanted and W-implanted annealed tungsten (0.4 and 0.5 dpa respectively) obtained with a 1 µm spherical tip by Weaver *et al*.[57] The He-implanted tungsten exhibits higher flow stresses than the self-implanted tungsten, which in turn is slightly higher than that of the neutron-irradiated tungsten (radiation damage level of 1.67 dpa). The difference in the hardening of the implanted samples may be attributed to the He bubbles playing a more dominant role in the mechanical response compared to the dislocation loops in the W-implanted region due to their higher density (8.5×10^{23} m^{-3} compared to 3×10^{23} m^{-3} respectively) and greater barrier strength. Although the voids from ion irradiation tend to be smaller than those formed from neutrons,[96] the density of He bubbles in the He-implanted sample is higher than the density of voids decorated by clusters Re and Os in this study's sample (2.5×10^{21} m^{-3}).[57,89] The barrier strength of the Re-Os precipitates is not currently known. The reported values of indentation YS for the ion-implanted samples (~4 GPa) are similar to those obtained from both the unirradiated and irradiated samples in this study shown in Table 4.5 (5 µm tip, 0.00032 s^{-1} strain rate) from Method 2, involving back-extrapolation of the hardening portion of the flow curve. However, as highlighted in Section 4.3.1, knowledge of the strain rate at which the spherical test was conducted at is needed for direct and reliable comparison between results.

4.3.3 Effect of Tip Size

A further consideration in micromechanical testing using micron and sub-micron scales is the indentation size effect (ISE), where an increase in hardness is observed with decreasing penetration, and is of particular importance at depths below 1 µm.[47] As discussed in Section 2.3.3, the ISE exhibits differently in Berkovich and spherical indentation; unlike sharp indenters, the ISE is dependent on the radius of the sphere rather than penetration depth.[62] An apparent increase in indentation stress / hardness may be observed with a decrease in indenter radius as the continuum approach breaks down, and smaller spheres may be more prone to produce indentation pop-ins. These are discrete displacement or strain bursts (for a load-controlled test) which occur without a significant increase in applied indenter load. Pop-in events are often associated with the onset of plastic deformation or the

difficulty of nucleating and activating dislocation sources within the primary indentation zone, which can relieve the high elastic stresses underneath the tip.[98] Since the indentation zone increases with tip size, using a 10 µm instead of a 5 µm tip (or 7.5 µm and 3.7 µm in this study respectively, following calibration) allows dislocation sources to be activated more easily at a lower indentation depth and load. It should be noted that in single crystal tungsten which has been electropolished, it is likely that the material is homogenous and contains few defects, meaning that the formation of new dislocation structures as well as geometrically necessary dislocations (GNDs) around the tip is required to accommodate it in the material.[47,61] When using small indenter tips, the stress required to generate a source can be large enough to approach the theoretical shear stress of the sample causing the pop-in feature to be visible in ISS curves, particularly if the primary indentation zone at the point of plastic yield is smaller than the length scale of dislocation networks (e.g. in materials with low dislocation densities where thermal activation is required for dislocation nucleation).[114,115]

Across the ISS curves in Figure 4.7 and Figure 4.10, Method 2 provides a reasonable means of marking the elastic-plastic transition despite the presence of pop-ins, although a more accurate value of stress would be better determined using a tip larger than 10 µm.

When comparing the Method 2 YS values and ISS curves at 3.2 x 10^{-4} s^{-1} for the unirradiated tungsten sample in Table 4.2, Table 4.3 and Figure 4.14, it can be observed that the YS obtained with the 10 µm tip is slightly higher than the 5 µm tip, and that the pop-in is noticeably smaller. There is also initially more hardening in the ISS curve, before plateauing to a flow stress comparable to the curve for the 5 µm tip. This may be a result of the 10 µm tip eliciting a harder contact response than the 5 µm tip due to the effects of surface roughness being amplified, given that the surface peaks and troughs are larger in comparison to the smaller tip. Weaver *et al.*[57] also reported a higher indentation YS acquired with a 10 µm indenter in He-implanted tungsten compared with using a 1 µm tip.

As shown in Figure 4.17, the contact radius at indentation yield is 120 nm and 260 nm for the 5 µm and 10 µm tip respectively, leading to corresponding indentation zone sizes of 288 nm and 624

nm using the $2.4a$ estimation by Pathak and Kalidindi.[55] Considering that dislocation cell sizes in the majority of metals are reported to be in the order of 1 µm, it is likely that both tips were not large enough to efficiently generate the dislocations required for strain hardening.

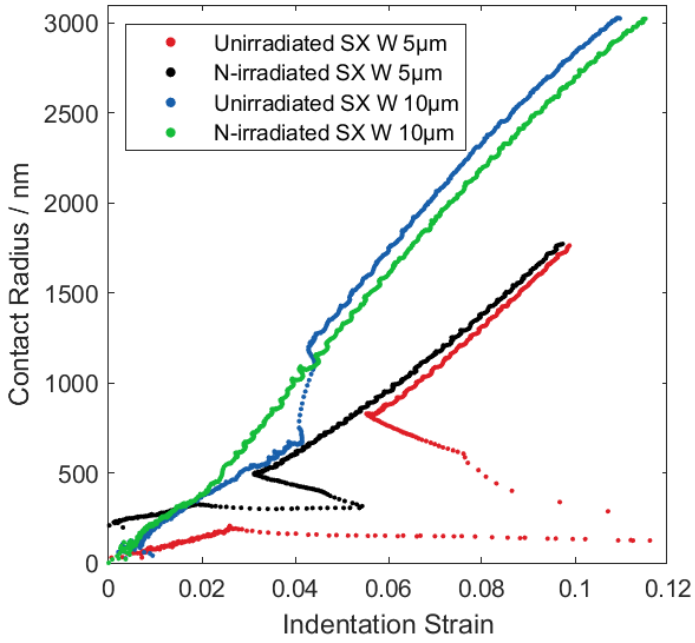


Figure 4.17: *Graph of contact radius (CSM signal) vs indentation strain for 5 µm and 10 µm tips in SX and NISX at a strain rate of 3.2 x 10^{-4} s^{-1}.*

Similarly, for the at 3.2 x 10^{-4} s^{-1} tests in the irradiated sample, the contact radii for the smaller and larger tip during yield are 315 nm and 430 nm (Figure 4.17), resulting in respective indentation zone sizes of 756 nm and 1032 nm respectively. This is consistent with the reduced occurrence and size of pop-ins exhibited in the ISS curves of the irradiated data from the 10 µm tip. Furthermore, the contact radius increases at a faster rate for the larger indenter, resulting in the increased strain hardening rate observed. The relationship between the size of the highly stressed zone beneath the tip and the spacing between dislocations and other defects are reflected in the 1.0 GPa difference in YS between tips in the unirradiated sample, and the 1.7 GPa difference in the irradiated sample. Increasing the initial dislocation density (and thus reducing the dislocation spacing) would produce a similar result to using a larger indenter radius.[115] It is likely that beyond tip sizes of 10 µm, a spherical ISE may be observed whereby lower hardness or indentation stress values to be obtained with tips of a greater radius, as this has been reported previously by other authors.[62]

It can also be observed that for the 5 µm tip, a small method artifact is visible in the load-displacement curve at small displacements (<50 nm) during elastic loading (Figure 4.5). This could be mitigated by selecting a lower initial strain value than 0.02 for the switch between displacement-controlled to strain-rate controlled (using the time derivative of Equation 3.11). Since nanoindentation devices are often load-controlled, using a displacement-controlled and strain-controlled method makes indenter control challenging, and a finite displacement depth must be reached before strain can be calculated. Alternatively, using a larger tip can avoid this artifact, as demonstrated by the 10 µm results. The use of larger tips are also beneficial in avoiding pop-ins, which can obscure yield point and elastic-plastic transition, or different methods of polishing may be chosen to eliminate the presence of pop-ins (as discussed in Section 4.3.2). If electropolishing is required to achieve a smooth surface for further characterisation, such as for high resolution electron backscattered diffraction (HR-EBSD) in this case, then indenter tips of radii greater than 10 µm are recommended.

4.4 Summary

Berkovich and spherical nanoindentation were performed in single crystal tungsten and neutron-irradiated single crystal tungsten (final composition W - 1.20 ± 0.11 at.% Re - 0.11 ± 0.05 at.% Os - 0.03 ± 0.01 at.% Ta). The Berkovich results were in strong agreement with the spherical indentation hardness values calculated at 8 % strain, with the hardness increase after irradiation ranging from 1.53 – 2.44 GPa for the 5 µm radius tip, and 2.41 – 3.22 GPa for the 10 µm radius tip, as the strain rate was increased from 3.2 x 10^{-5} s^{-1} to 3.2 x 10^{-3} s^{-1}. The 5 µm tip spherical hardness results from the medium strain rate of 3.2 x 10^{-4} s^{-1} matched the Berkovich results closely. Furthermore, the irradiation-induced hardening is consistent with other studies in tungsten neutron-irradiated to similar damage levels and with similar transmutation rates, in addition to self-ion irradiated tungsten.

ISS curves were successfully produced from 5 µm and 10 µm spherical tips, giving insight into the elastic loading and hardening behaviour as well as extraction of YS values despite the presence of pop-

ins. However, several methods of yield stress extraction were employed due to the difference in curve shape in the unirradiated and neutron-irradiated samples, as well as the occurrence of pop-ins; the three methods are described in Section 4.2.3 and displayed in Figure 4.7 (c) and (d).

A strain-rate dependence is exhibited by both materials, highlighting the need to use strain rates specific to spherical tips which account for tip imperfections. Lack of adequate strain rate control, particularly for rate-sensitive materials, can lead to inaccurate depictions of the work hardening behaviour in the ISS curves as well as cause discrepancies in spherical nanoindentation results reported. This study involved robust spherical tip calibration and tuning of the nanoindenter's proportional-integral-derivative (PID) device, with the latter being necessary due to the difficulty in implementing a strain-controlled method on a load-controlled device. This method allows calculation of a strain rate calibrated to the radius and area function of the sphere, rather than using the strain rate definition for self-similar tips, which can lead to an increase in strain rate over time.

There was an increase in strain rate sensitivity and reduction in activation volume after irradiation, indicating that the thermally activated motion of screw dislocations at room temperature is affected by the increased pinning caused by radiation-induced microstructural defects.

The YS values from tests at different strain rates in both materials are shown in Table 4.2 and Table 4.3. As one may expect, a higher YS is observed with increase in strain rate, but work hardening behaviour remains consistent as a function of strain, as demonstrated by an upwards shift in the flow portion of the ISS curves. Little work hardening was observed for the available range of strains beyond the pop-in effects in the unirradiated sample using both tip sizes, meaning that YS values from Methods 2 and 3 were very similar (between 4.2 GPa to 6.0 GPa), depending on the strain rate and tip size. The absence of work hardening and presence of large pop-ins in the sample are likely a result of the lack of defects in the high purity single crystal tungsten, causing dislocations to be nucleated in a burst, as well as enabling dislocation glide and channelling.

The ISS curves show that the irradiated sample exhibits a much higher indentation YS (4.5 GPa to 6.8 GPa) than the unirradiated one across all three evaluation methods, in addition to higher hardening rates. Method 2 of extracting YS appeared most effective in determining the transition from elastic to plastic deformation due to the steep gradient of the stress-strain curve during work hardening; this method of back-extrapolation has also been used in several other studies and thus provided a more consistent comparison with results in literature. The steep hardening region is followed by either strain softening or a plateau region dependent on tip size – this may be attributed to dislocation channelling, as seen in neutron irradiated bcc metals.

Higher YS values are determined from the 10 μm tip, possibly due to the 5 μm tip producing a softer contact response than the 10 μm tip arising from the reduced effect of surface roughness with a smaller tip. The contact radius for the 10 μm tip is also shown to increase at a faster rate with indentation strain than the 5 μm tip, explaining the increased strain hardening rate observed.

A smaller pop-in is exhibited with increased tip size, as well as in the irradiated sample compared to the unirradiated one. For small indenter tips, high stresses may be required to generate dislocation sources, particularly in a relatively defect-free sample. Contrastingly, the radiation defects provide abundant dislocation sources for activation without the requirement for pop-ins, which are often attributed to dislocation nucleation and mobility.

A minor method artifact was visible at small displacements (< 50 nm) in the load-displacement curves from the 5 μm tip, but not the 10 μm. This can be avoided by selecting a smaller value of strain for the transition from displacement-controlled to strain-rate controlled – a finite displacement is needed for the strain calculation – or alternatively, tips of 10 μm or larger can be used.

Furthermore, the use of tips larger than 10 μm in radius is recommended for future studies, in order to eliminate the presence of pop-ins and enable a more reliable method of examining yield stress values and elastic-plastic transition behaviour.

5 Characterising Deformation Behaviour in Neutron-Irradiated Tungsten

In this chapter, AFM and EBSD were employed to characterise the topography and deformation behaviour resulting from spherical indentation with nominally 5 µm and 10 µm tips (calibrated to 3.7 µm and 7.5 µm respectively) at three different strain rates, in unirradiated and neutron-irradiated single crystal tungsten samples (labelled 'SX' and 'NISX' respectively).

The AFM results were used to generate line profiles to examine differences in indentation pile-up resulting from strain rate and irradiation, in addition to calculating the volume of the pile-up produced. To assess the underlying deformation which caused the change in surface morphology, HR-EBSD maps were collected and compared between samples and strain rate conditions. This allowed the plastic deformation present to be quantified through the analysis of the elastic strains, lattice rotations and GNDs surrounding the indents by using XEBSD cross-correlation code.[93,94,95]

5.1 Indentation Morphology

In bcc metals such as tungsten, at room temperature it is assumed that deformation is accommodated by the slip of $a/2\ \langle 111 \rangle$ screw dislocations along the $\{110\}$ glide plane, with $\langle 111 \rangle$ being the closest-packed direction.[116,117,118] Das *et al.*[65] reported that spherical nanoindents in unimplanted tungsten showed little orientation dependence in pile-up, whilst larger pile-up morphologies are observed in grains with a surface normal of $\langle 001 \rangle$ compared to grains with normal of $\langle 110 \rangle$ and $\langle 111 \rangle$ orientations following helium-implantation. This has been attributed to a combination of the deformation field being constricted relative to the indent and the occurrence of localised deformation through slip channels, which are formed by dislocations interacting with implantation-induced defects.

As the single crystal tungsten in this study was indented on the (001) surface in both the unirradiated and neutron-irradiated states, pile-up was predicted to occur predominantly along the $\langle 110 \rangle$ directions, with greater pile-up in the irradiated sample.

AFM can produce surface topography maps with nanometre-scale resolution, and therefore probe the indent depth and response of the surrounding material, including the morphology, height and volume of the pile-up induced by indentation.

5.1.1 5 µm Indent Surface Profiles

The AFM surface micrographs and line profile data from the 5 µm tip indents in unirradiated and neutron-irradiated single crystal tungsten are displayed in Figure 5.1 and Figure 5.2 respectively. These maps and line profiles were produced from raw data using tools as per the method described in Section 3.5.

The general shape of the deformation confirmed by AFM consists of four lobes surrounding the central crater left by the indenter. The presence of four-fold symmetry in the pile-up pattern can be observed, although there is some asymmetry visible – particularly in the neutron-irradiated sample – likely resulting from imperfections in the tip or a slight misalignment between the tip and sample during nanoindentation.

Given that both the tip and sample remained in the same orientation for batch testing during nanoindentation and AFM experiments respectively, the height line profiles in this study are compared using a consistent direction rather than an average of multiple profiles taken with different directions, to avoid losing the integrity of the data. The arrow on the map shown in Figure 5.1 (a) denotes the direction in which the line profile has been extracted from the centre of each indent across all data sets. The difference in profiles in relation to direction of extraction is shown in Section 3.5.

Several observations can be noted regarding the behaviour of both the unirradiated and irradiated samples. Pile-up was observed to form in four distinct lobes along the $\langle 110 \rangle$ directions,

corresponding to the four $\langle 111 \rangle$ slip directions on the $\{110\}$ planes. These lobes are separated by regions of minimal pile-up along the $\langle 100 \rangle$ directions.

Table 5.1 contains data from the line profiles extracted from the AFM topography maps. The maximum residual indentation depth corresponds to the maximum depth of the crater following indentation, whilst the maximum pile-up height was averaged between the maximum heights of the two peaks for each curve due to the asymmetry. It is clear that there is an increase in residual indentation depth with strain rate despite programming the test to run to the same total strain of 0.1 with a set total displacement. The lack of consistency in total strain reached and total displacement is reflected in the stress strain curves in Chapter 4, and likely due to the challenging indenter control required to achieve the strain-controlled method of spherical nanoindentation described in Sections 3.4.1 and 4.3.3.

The pile-up height produced by nanoindentation measured by AFM (as displayed in Figure 5.1 and Figure 5.2), increases from 32 to 53 nm in SX and 44 to 110 nm in NISX as the strain rate is increased. Interestingly, regardless of the strain rate applied, the indentation depths consistently proved greater for the unirradiated material in comparison to its neutron-irradiated counterpart. This disparity can be attributed to the unirradiated material exhibiting a lower hardness and reduced tendency to work harden (as reported in Sections 4.2.3 and 4.2.4), indicating fewer short-range barriers to dislocation motion and thus material flow. Given the difference in the residual indentation depth across strain rates, the heights normalised as a function of maximum residual indent depth are shown in Figure 5.2 (c) and (d); generally, this normalised height increases with strain rate, ranging from ~8.6% to ~11.8% for SX, and ~21.8% to ~36.5% for NISX. Therefore, despite the nanoindentation method artifact in total nanoindenter displacement, there is a clear increase in pile-up following irradiation.

Furthermore, given that the total indenter displacement is relatively consistent at a given strain rate across both materials, the difference in pile-up height after irradiation can be quantified at each

strain rate. As shown in Table 5.1, pile-up was 38 % higher for the lowest strain rate and 107 % higher for the higher two strain rates.

The AFM micrograph of the unirradiated material shown in Figure 5.3 (a) shows four distinct plastic lobes, with channels of depressed material extending in the same direction as each lobe. The difference in height between the surface and depressed channels is only 5nm. These channels extend to a length of ~30 µm. However, in Figure 5.3 (b), there are no visible channels extending from the four lobes in the irradiated material.

Table 5.1: *AFM height profile data for indents conducted with a 5 µm spherical tip at different strain rates in unirradiated single crystal tungsten (SX) and neutron-irradiated single crystal tungsten (NISX).*

Material and strain rate conditions	Maximum residual indentation depth / µm	Maximum pile-up height / µm	Increase in pile-up post-irradiation (by strain rate) / %
SX 3.2 x 10^{-3} s^{-1}	-0.446	0.053	-
SX 3.2 x 10^{-4} s^{-1}	-0.364	0.042	-
SX 3.2 x 10^{-5} s^{-1}	-0.331	0.032	-
NISX 3.2 x 10^{-3} s^{-1}	-0.388	0.110	107
NISX 3.2 x 10^{-4} s^{-1}	-0.337	0.087	107
NISX 3.2 x 10^{-5} s^{-1}	-0.205	0.044	38

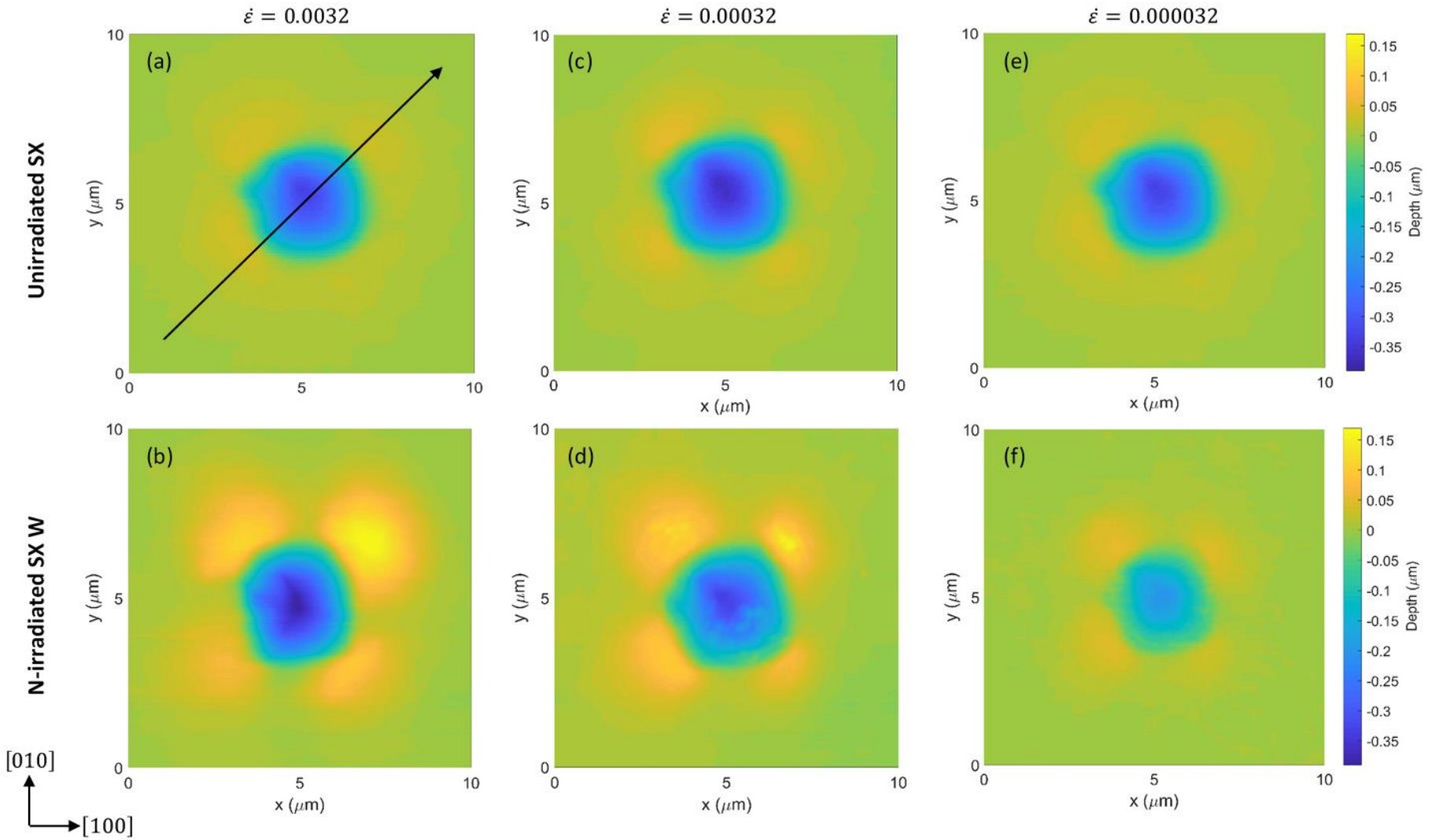


Figure 5.1: *AFM micrographs of spherical indents performed with a 5 µm radius indenter in unirradiated single crystal tungsten* ***(a, c, e)*** *and neutron-irradiated tungsten* ***(b, d, f)*** *at strain rates of 3.2 x 10^{-3} s^{-1}, 3.2 x 10^{-4} s^{-1} and 3.2 x 10^{-5} s^{-1} respectively. The arrow on* ***(a)*** *shows the direction of the line profile extraction.*

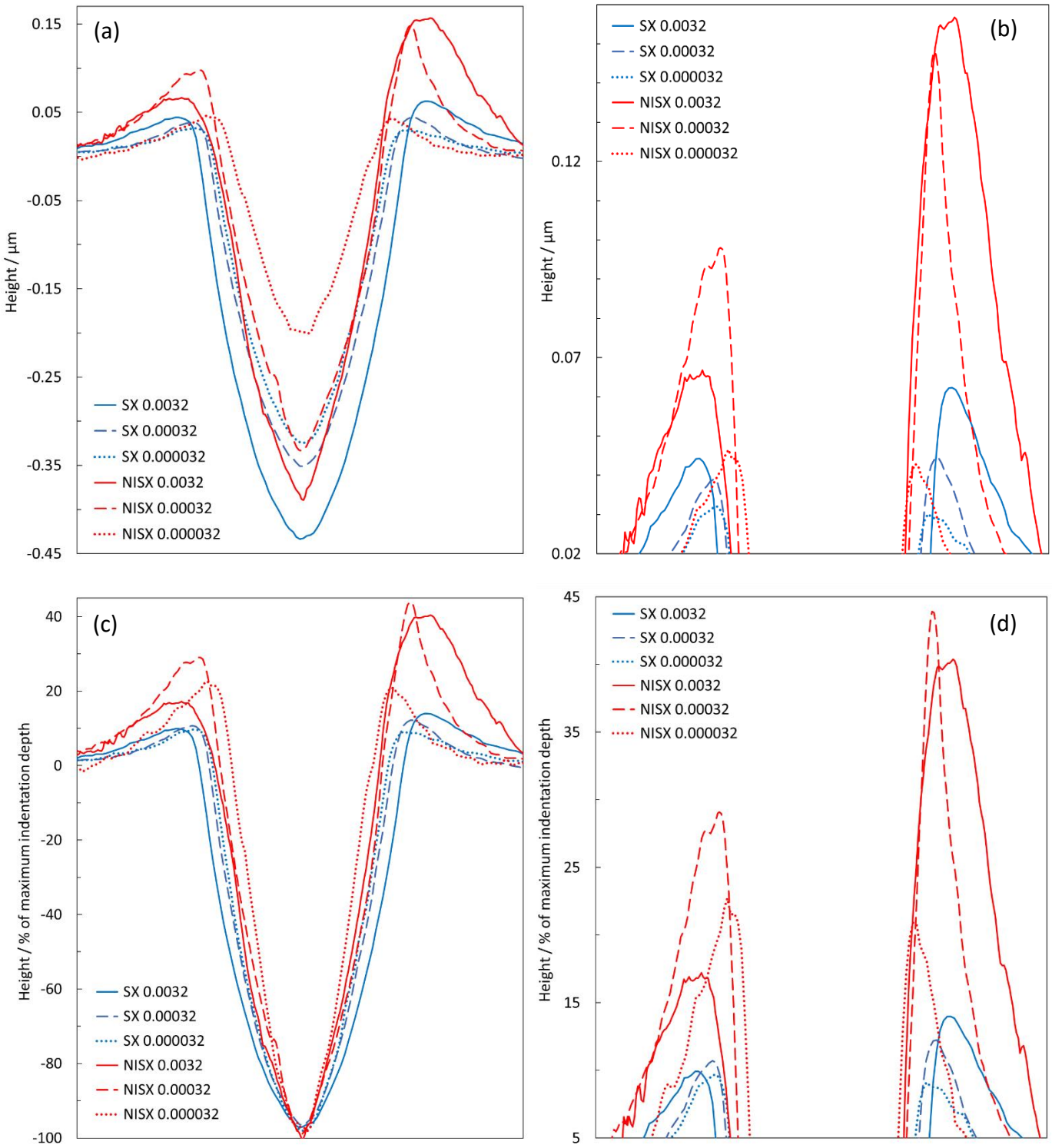


Figure 5.2: (a) *AFM line profiles of spherical indents performed with a 5 µm radius indenter in SX and NISX at strain rates of 3.2 x 10^{-3} s^{-1}, 3.2 x 10^{-4} s^{-1} and 3.2 x 10^{-5} s^{-1} respectively.* ***(b)*** *Magnified view of the pile-up region in the line profiles.* ***(c)*** *Normalised AFM height as a percentage of maximum residual indentation depth.* ***(d)*** *Magnified view of the pile-up region of the normalised height profiles.*

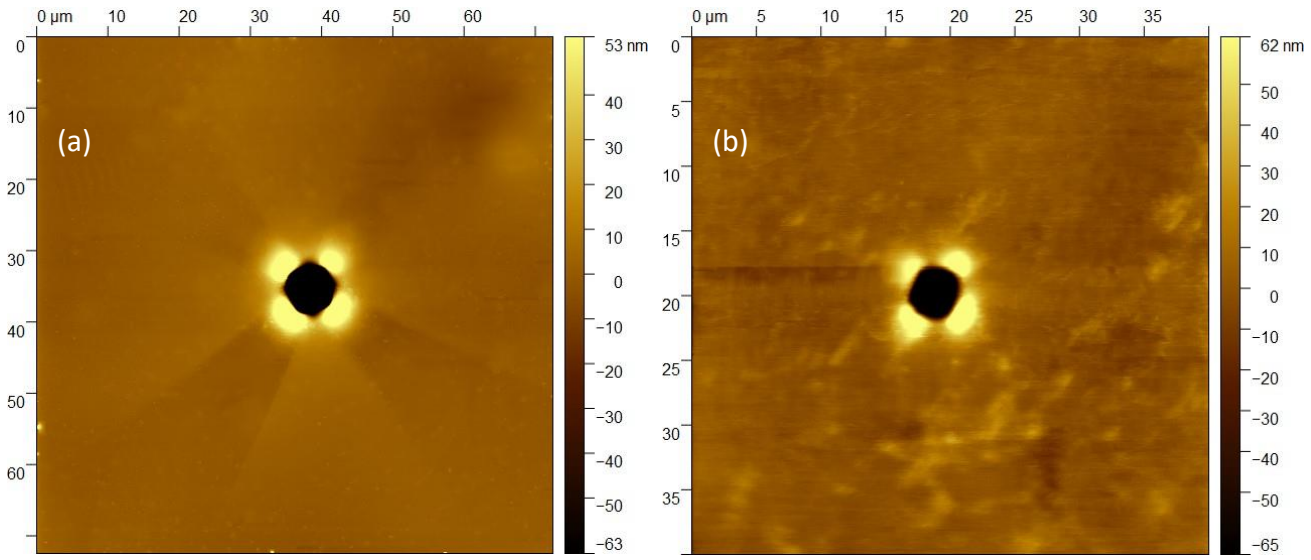


Figure 5.3: *AFM micrographs of an indent measured at 3.2 x 10^{-3} s^{-1} in **(a)** unirradiated single crystal tungsten and **(b)** and neutron-irradiated single crystal tungsten.*

5.1.2 10 µm Indent Surface Profiles

The AFM surface micrographs and line profile data from the 10 µm tip indents in unirradiated and neutron-irradiated single crystal tungsten are displayed in Figure 5.4 and Figure 5.5 respectively. For each material, the general shape of the deformation matches the four lobes seen around the 5 µm indents. Again, slight asymmetry is visible, indicating the presence of tip imperfections and / or minor misalignment between the tip and sample during indentation.

Table 5.2 displays the data from the line profiles extracted from the AFM topography maps according to the same method used in Section 5.1.1 and described in Section 3.5. As is the case for the 5 µm indents, there was an increase in indentation depth with strain rate due to the nanoindentation method. As the total indenter displacement was consistent for a given strain rate across both materials, the difference in pile-up height after irradiation was compared, yielding an increase of 160 %, 156% and 198 % at the slow, medium and fast strain rates respectively.

In addition, heights were normalised as a function of maximum residual indent depth to compare between different total displacements across strain rates, as shown in Figure 5.5 (c) and (d); normalised height increases with strain rate, ranging from ~13.1% to ~14.0% for SX, and ~24.2% to ~27.3% for NISX, indicating a clear increase in pile-up post-irradiation.

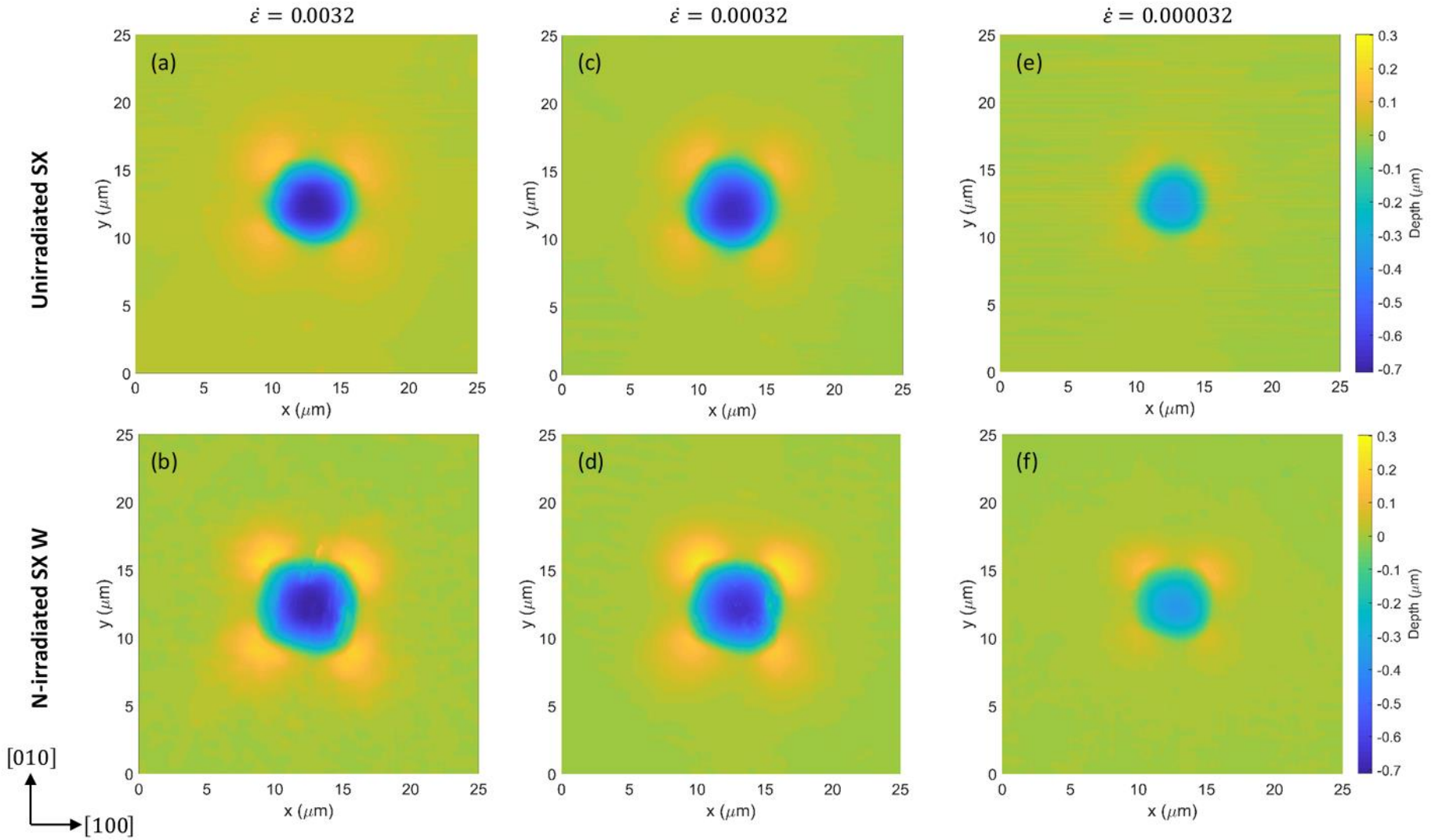


Figure 5.4: *AFM micrographs of spherical indents performed with a 10 µm radius indenter in unirradiated single crystal tungsten* ***(a, c, e)*** *and neutron-irradiated single crystal tungsten* ***(b, d, f)*** *at strain rates of 3.2 x 10^{-3} s^{-1}, 3.2 x 10^{-4} s^{-1} and 3.2 x 10^{-5} s^{-1} respectively. Both samples were indented in the [001] orientation.*

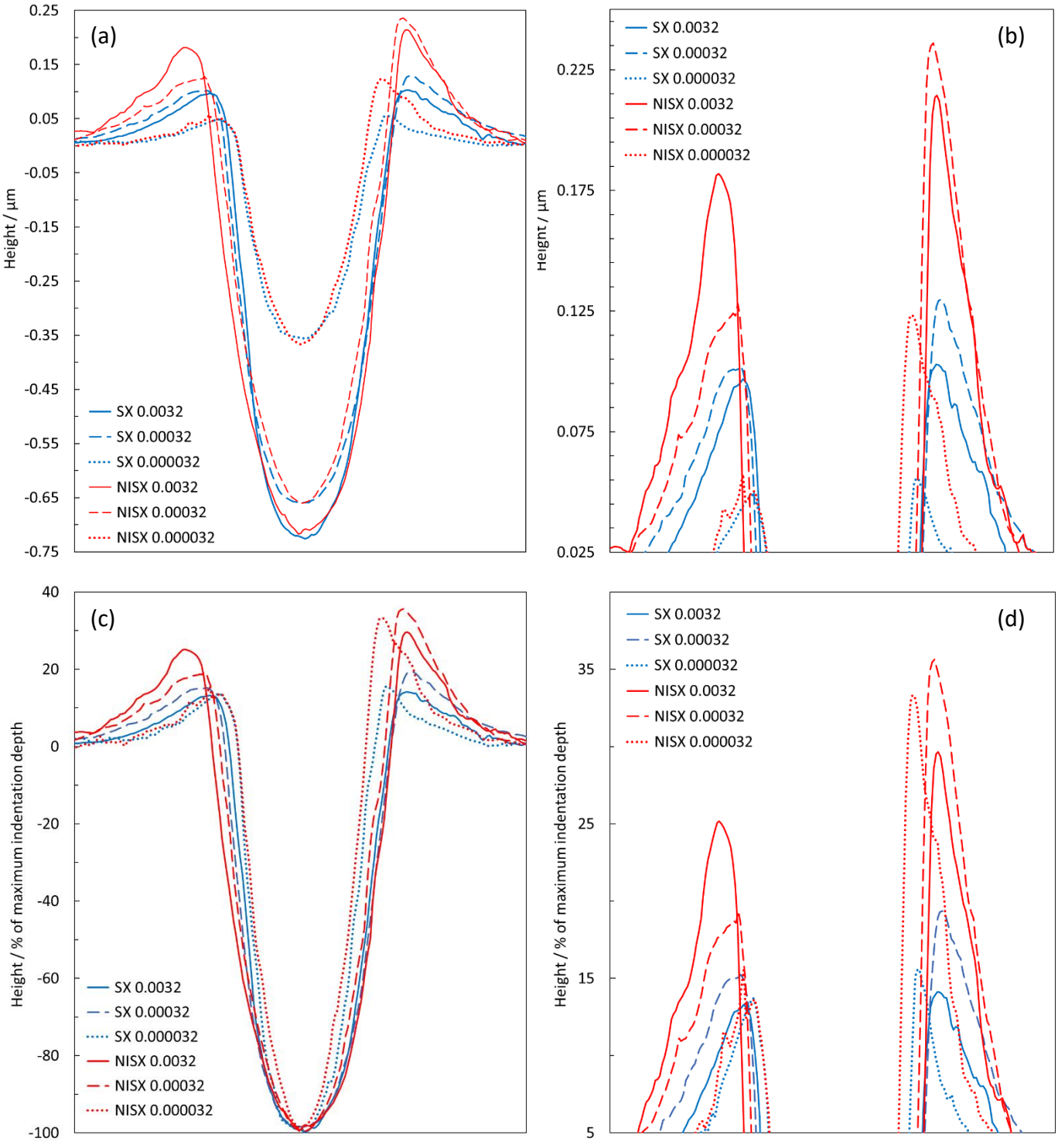


Figure 5.5: (a) *AFM line profiles of spherical indents performed with a 10 µm radius indenter in SX and NISX at strain rates of 3.2 x 10^{-3} s^{-1}, 3.2 x 10^{-4} s^{-1} and 3.2 x 10^{-5} s^{-1} respectively.* ***(b)*** *Magnified view of the pile-up region in the line profiles.* ***(c)*** *Normalised AFM height as a percentage of maximum residual indentation depth.* ***(d)*** *Magnified view of the pile-up region of the normalised height profiles.*

Table 5.2: *AFM height profile data for 10 µm indents at different strain rates in SX and NISX.*

Material and strain rate conditions	Maximum residual indentation depth / µm	Maximum pile-up height / µm	Increase in pile-up post-irradiation (by strain rate) / %
SX 3.2 x 10^{-3} s^{-1}	-0.728	0.100	-
SX 3.2 x 10^{-4} s^{-1}	-0.670	0.115	-
SX 3.2 x 10^{-6} s^{-1}	-0.357	0.052	-
NISX 3.2 x 10^{-3} s^{-1}	-0.723	0.198	98
NISX 3.2 x 10^{-4} s^{-1}	-0.662	0.180	56
NISX 3.2 x 10^{-5} s^{-1}	-0.370	0.083	60

5.1.3 Pile-up Volume

The AFM results were used to calculate the volume of pile-up produced by the spherical nanoindentation experiments using a script written by Dr Luke Hewitt (and based upon code by Mr William Witt). The purpose of the code is to fit a plane to the annulus of the indent and calculate the volume above and below the surface (i.e. in the pile-up and indentation pit respectively) using the number of pixels above and below the plane. The zero point used for the plane was defined by the background removal in Gwyddion as detailed in Section 3.5. The pixel size (i.e. area) is multiplied by the height, and summed across the user-defined volume of calculation. The radius in which all volume calculation data is obtained from is denoted by the edge of the black circle on the 3D view of each indent shown in Figure 5.6. The inner boundary of the pile up zone is assumed to start at the first volume contribution outside the annulus of the indent. The outer boundary of the pile-up zone is defined as the point at which the volume decreases by a user-defined fraction of the volume measured at the inner boundary; typically, the outer boundary was taken at a point where the volume decreased by 2 % compared to the volume measured at the inner boundary point. The user is able to visually confirm the results and re-define the outer boundary of the pile-up zone if the 2 % starting assumption is incorrect. An example of the pile-up zone obtained when the user-defined value is chosen as 12 % is shown in Figure 5.7; one can observe that the pile-up zone displayed reaches far beyond the point

at which the surface height decreases to near-zero, indicating the need for the user to visually check output results and refine the starting assumption for the outer boundary calculation as needed. Failure to do so can artificially affect the ratio of the volume above the surface to the volume below the surface, given that the volume of the indenter pit remains the same.

As described in Sections 5.1.1 and 5.1.2, the maximum residual indentation depth increases with strain rate due to indenter control. Whereas pile-up height could be compared using the line profiles only at the same strain rate, analysing the ratio of the volume above the surface to the volume below provides a consistent way of quantifying pile-up as a function of strain rate and material.

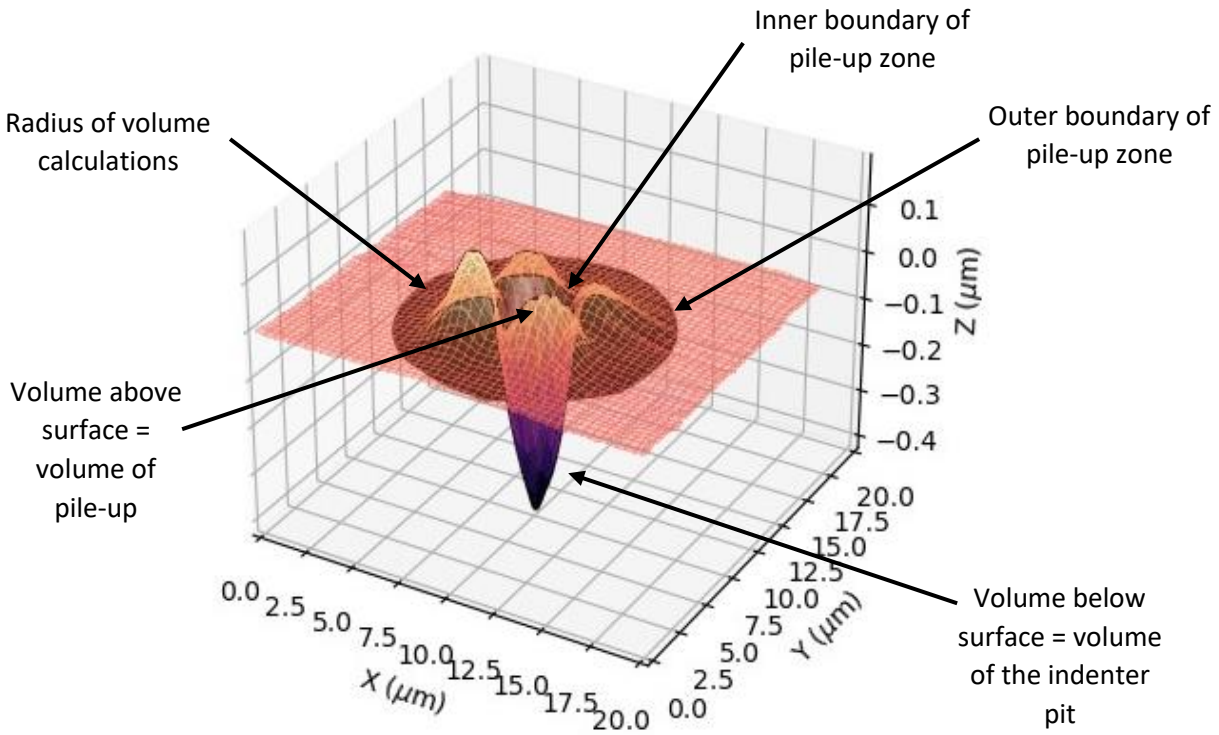


Figure 5.6: *Example of the 3D visual output produced by the script for calculating the volume above and below the surface, representing the volume of the pile-up and indenter trough respectively. The inner and outer boundaries of the pile-up zone denote the area in which pile-up is assumed to occur. In this example, the outer boundary of the pile-up zone is defined as the point at which the volume decreases by 2 % of the volume measured at the inner boundary. The data used for all volume calculations is contained within the radius of the black circle.*

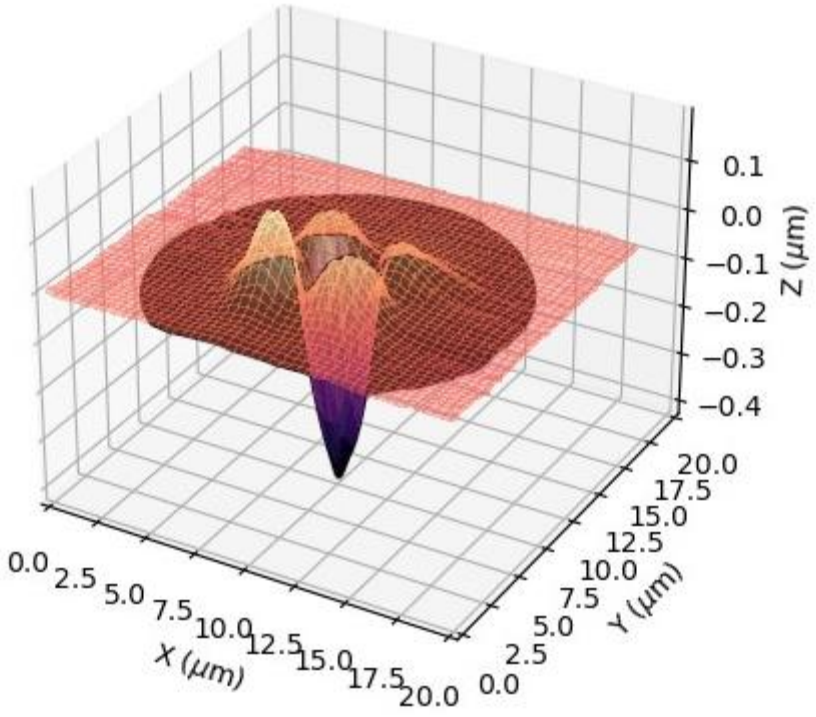


Figure 5.7: *Example of the increased pile-up zone when the outer boundary of the pile-up zone is defined as the point at which the volume decreases by 12 % of the volume measured at the inner boundary instead of 2 %.*

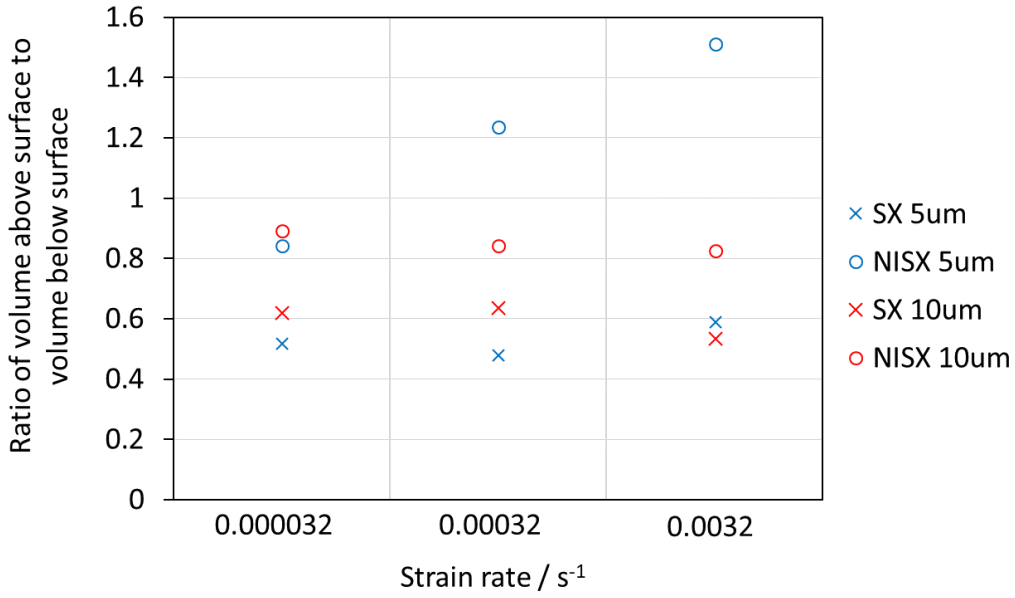


Figure 5.8: *Graph showing the ratio of the volume above the surface to the volume below the surface as a consistent means of comparing the quantity of pile-up with respect to indentation depth for each strain rate in both the SX and NISX samples.*

Figure 5.8 shows the ratio of the volume above the surface to the volume below the surface for SX and NISX across the three strain rates. Notably the ratio of the volume above the surface to volume below is less than 1 for all tests except for the two fastest strain rates in the irradiated sample with the 5 µm tip; this means that there is generally a greater volume in the indentation pit than in the pile-up. This observation can be attributed to elastic deformation, or potentially some of the displaced material could have contributed towards a gentle protrusion of the surface further afield which was not measured by AFM in this study, rather than flowing into the local pile-up region.

For all indents with both 5 µm and 10 µm tips, there is a greater ratio of volume above to volume below in the neutron-irradiated sample compared to unirradiated at the same strain rate, meaning that pile-up is enhanced in the irradiated tungsten. The ratio is roughly constant as a function of strain rate in the unirradiated state with both tip sizes, as well in the irradiated sample using the 10 µm tip. However, for 5 µm indents in the irradiated sample, there is a positive trend in the ratio with strain rate, although this could be due to noise considering each data set was based on one indent.

As displayed in Table 5.3, this corresponds to a relatively consistent increase in the ratio with strain rate for the irradiated material compared to unirradiated for 10 µm indents (between 42 – 44 % increase). The ratio increase for the 5 µm tip indents is considerably more prevalent with strain rate (63 % to 157 % from 3.2 x 10^{-5} s^{-1} to 3.2 x 10^{-3} s^{-1}), which could be a result of the indentation size effect.

Table 5.3: *Graph of the percentage difference in the ratio of volume above the surface to the volume below in the irradiated tungsten compared to unirradiated for all strain rates. This difference was calculated using the volume data for both tips displayed in Figure 5.8*.

Tip size and strain rate conditions	Increase in ratio of volume above to volume below in irradiated vs unirradiated / %
5 µm 3.2 x 10^{-5} s^{-1}	63
5 µm 3.2 x 10^{-4} s^{-1}	158
5 µm 3.2 x 10^{-3} s^{-1}	157
10 µm 3.2 x 10^{-5} s^{-1}	44
10 µm 3.2 x 10^{-4} s^{-1}	8
10 µm 3.2 x 10^{-3} s^{-1}	42

5.2 Characterisation of Deformation Structures

5.2.1 SEM

The SEM micrographs of the 5 µm spherical indents performed at 3.2 x 10^{-4} s^{-1} shown in Figure 5.9 were obtained using SE imaging to capture topography and morphology. As seen in the AFM maps in Figure 5.1, there is a four-fold symmetry in the pile-up pattern around both indents, corresponding to the ⟨110⟩ directions and thus ⟨111⟩ slip directions. In Figure 5.9 (b), traces of slip steps can be seen at the edge of the pile-up lobes in the neutron-irradiated sample, as indicated by the black arrows.

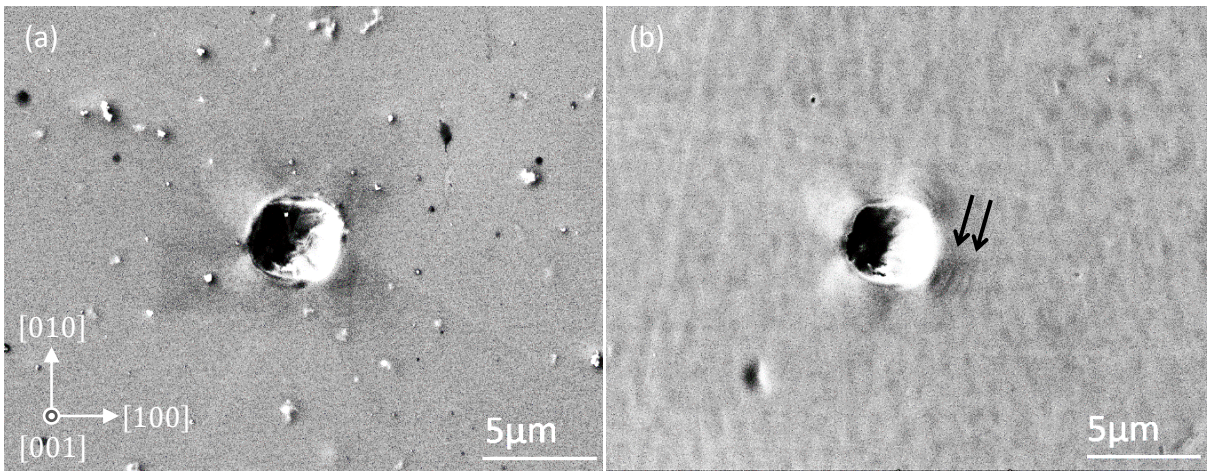


Figure 5.9: *SEM micrographs of 5 µm spherical indents at 3.2 x 10^{-4} s^{-1} in* ***(a)*** *SX and* ***(b)*** *NISX, where the black arrows indicate the presence of slip bands.*

5.2.2 HR-EBSD

In addition to analysing pile-up morphology, plastic deformation behaviour can be further analysed by examining the deformation field around the indents by using HR-EBSD. This technique enables the effect of irradiation and strain rate on the elastic strains (or lattice spacing) and lattice rotations to be explored, in addition to measuring the density of GNDs to quantify the level of plastic deformation present. As described in Section 3.6.1, cross-correlation analysis was performed on the HR-EBSD maps using XEBSD.[93,94,95] Unfortunately the data set for the indent at 3.2 x 10^{-5} s^{-1} in NISX corrupted.

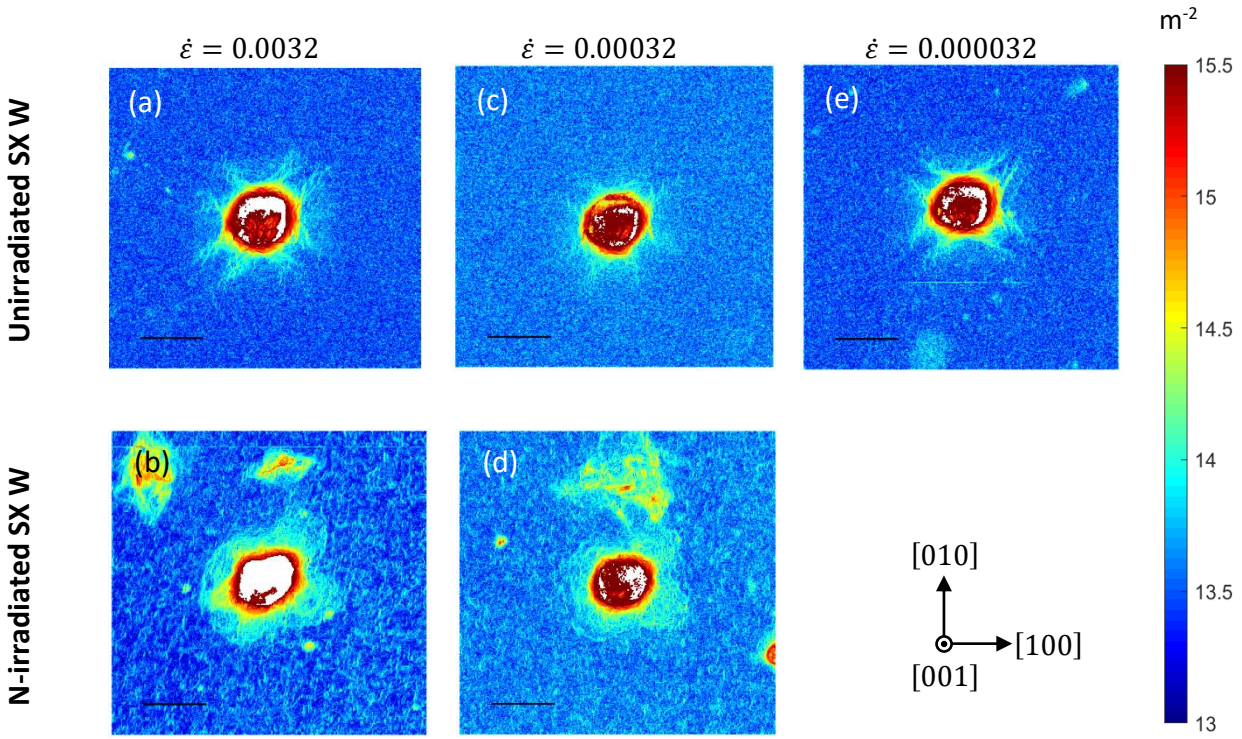


Figure 5.10: *Total GND density (ρ) maps in the XY plane for indents performed with a 5 µm tip in* ***(a, c, e)*** *SX and* ***(b, d)*** *NISX. Colour scale units are in log(ρ) with ρ in m^{-2}. Scale bars correspond to 5 µm.*

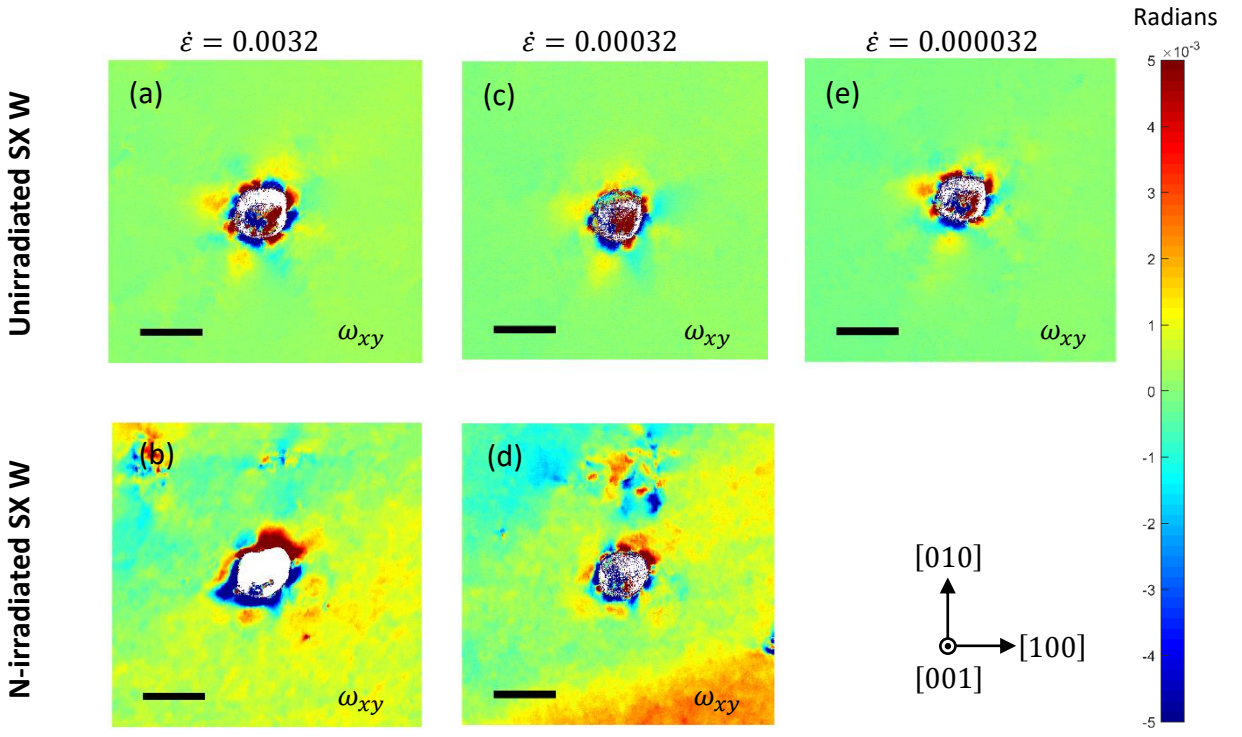


Figure 5.11: *ω_{xy} lattice rotation fields about [001] for 5 µm tip indents in* ***(a, c, e)*** *SX and* ***(b, d)*** *NISX at varying strain rates. Lattice rotations are plotted in radians and scale bars correspond to 5 µm.*

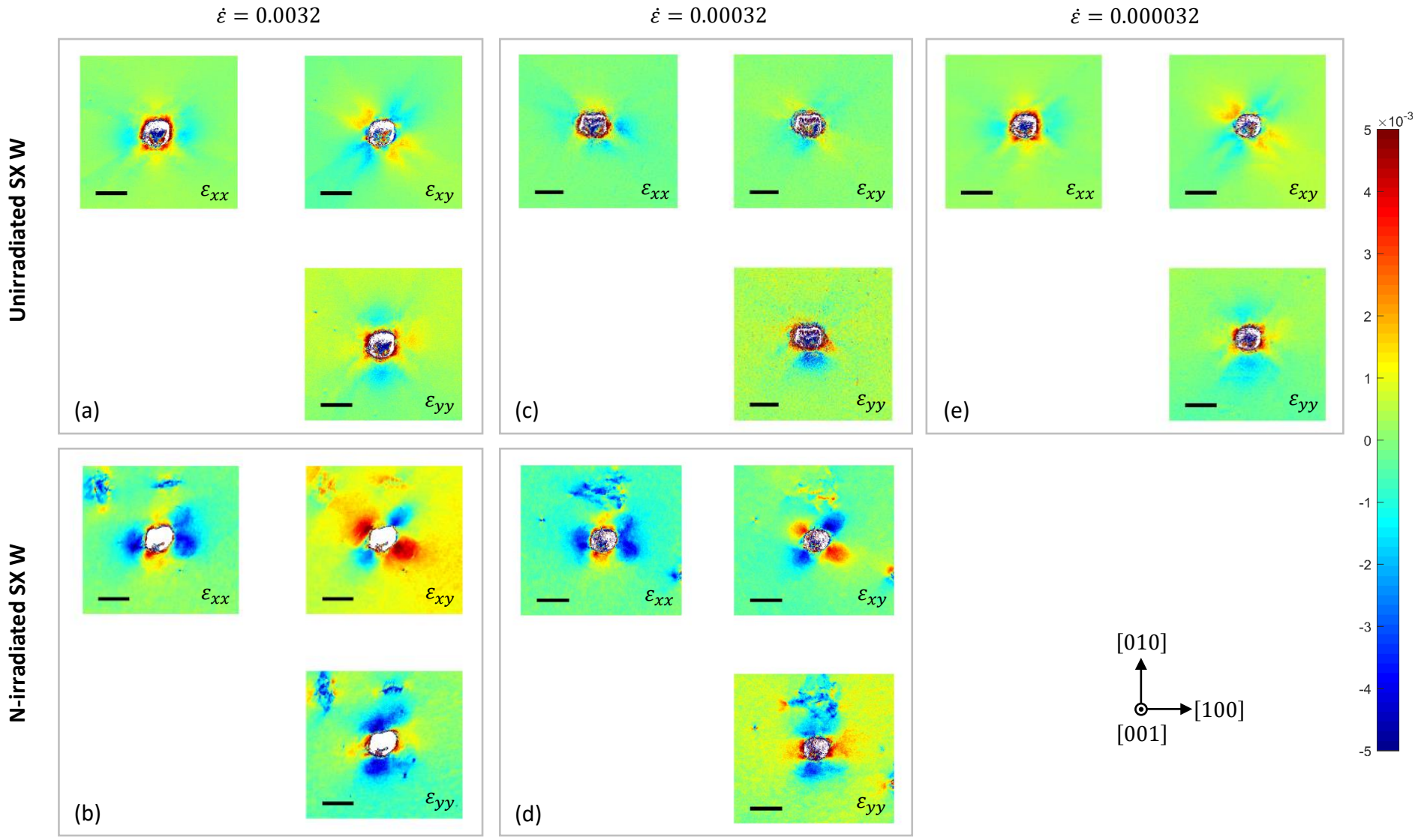


Figure 5.12: *Elastic strains maps for indents performed with a 5 µm tip in* ***(a, c, e)*** *SX and* ***(b, d, f)*** *NISX at varying strain rates. Both samples were indented in the [001] orientation. Scale bars correspond to 5 µm.*

Figure 5.10 shows the GND density (ρ) maps for both SX and NISX. In the unirradiated tungsten, the background beyond the crater area has a consistently low ρ, except for some small imperfections. The pattern in the regions of increased ρ (compared to the background) at the boundary of the indents is similar across all the strain rates and corresponds to the edges of the four lobes. In the neutron-irradiated tungsten, the background outside of the indent pit is less uniform than in the unirradiated sample but also has a low density. Interestingly, the background is interspersed with finer regions of increased density as well larger pockets of significantly higher ρ which could be a result of noise or surface impurities. The higher ρ zones corresponding to the lobes is of similar ρ to those in the unirradiated tungsten (~10^{14} m^{-2}), but they are more pronounced and cover the entirety of the lobes rather than being concentrated at the edges.

The ω_{xy} components for rotations around the z-axis are displayed in Figure 5.11. These in-plane rotations are relatively small for the unirradiated sample with a minor increase as a function of strain rate. The size of the rotations in the area outside of the indent stays relatively constant with strain rate. The rotation fields around the indents in the irradiated material are visibly larger than the unirradiated state, with some greater areas of rotation in beyond the pile-up area which is associated with noise in the data.

The strain maps in Figure 5.12 show clear differences in the residual elastic strain fields around indents in the unirradiated and neutron-irradiated tungsten. For both materials, the ε_{xx} component for normal strain in the x-axis shows balanced compression on the left and right sides of the indent and tension above and below the indents, corresponding to radial compression and tensile hoop (tangential) strain. However, the strain magnitudes are significantly larger in the NISX (± 3 ×10^{-3} to ± 5×10^{-3}, compared to ± 1 ×10^{-3} to ± 2×10^{-3} in SX). There are also several small localised points with significant strain outside of the pile-up zone in the irradiated sample, which could be a result of noise. The ε_{yy} components show the same result but along the y-axis.

The in-plane shear strains shown by the ε_{xy} component shows the shear of the normal strains (corresponding to the radial compression and tensile hoop strain). This is demonstrated by the compression in one axis along the 45° angle of two lobes, and tension in the orthogonal axis. In the unirradiated material there is a slight increase in the strain magnitudes in the lobes as a function of strain rate whilst the background remains consistent. However, the irradiated sample exhibits a more significant increase in both the strain in the lobes as well as in the surrounding area beyond the pile-up. The size of the strain fields around the indents (corresponding to the lobe regions) increases slightly with strain rate for both materials.

5.3 Discussion

5.3.1 Pile-up Morphology

A combination of AFM and HR-EBSD was used to characterise the pile-up morphology and examine plastic deformation resulting from spherical indentation with nominally 5 µm and 10 µm tips in SX and NISX. Pile-up occurred preferentially along the $\langle 110 \rangle$ directions, corresponding to the four $\langle 111 \rangle$ slip directions on the $\{110\}$ planes; this confirms that the deformation process is dominated by activity on the primary slip system $\{110\}\langle 111 \rangle$, producing excess material upon intersection with the surface. Figure 5.1 (b, d, f) and Figure 5.4 (b, d, f) show that for indents in the irradiated material, the residual impression is square in shape (with edges along the $\langle 100 \rangle$ directions) as a result of the orientation-dependence of plasticity.

The four-fold symmetry seen in the AFM and SEM micrographs has been observed previously around nanoindents in (001)-orientated single crystal W and Cu.[65,119] Wang *et al.*[119] further reported the presence of two-fold symmetry in the height profiles for (011)-orientated crystals and six-fold symmetry for the (111) -orientated crystals, indicating that the pile-up patterns are both crystallographic and orientation dependent.

5.3.2 Effect of Irradiation and Strain Rate

Similar values were obtained for the average increase in pile-up height after irradiation across all strain rates using both 5 µm and 10 µm tips (173 % and 179 % respectively). Given the difference in the total indentation displacement across strain rates due to the nanoindentation method, the surface heights were normalised as a function of maximum residual indent depth. This normalised height generally increased with strain rate, ranging from ~8.6 % to ~11.8 % for SX, and ~21.8 % to ~36.5 % for NISX with the 5 µm radius tip; in the 10 µm tip case, normalised heights ranging from ~13.1 % to ~14.0 % for SX, and ~24.2 % to ~27.3 % for NISX, were obtained. These results indicate a clear increase in pile-up post-irradiation, but it is uncertain whether increasing the strain rate had a real effect on the height of the pile-up produced due to the nanoindentation method.

Likewise, there was a greater ratio of the volume of pile up material above the surface to that displaced by the indenter in NISX, confirming an increase in pile-up despite the variation in indentation depth with strain rate. The percentage increase in the ratio after irradiation across the strain rates was ~3 times higher when using the 5 µm tip indenter compared to the 10 µm tip, which indicates the presence of a size effect.

This ratio was smaller than 1 for the majority of the material and strain rate parameters reported (Figure 5.8), except for at the two fastest strain rates in NISX with the 5 µm tip, which could be due to noise considering that each data set was based on AFM from one indent only per strain rate and material condition due to time constraints. It is important to note that some of the displaced material may not have contribute to the four-fold pile-up local to the indent, and instead could have caused a subtle bulging of the surface further afield not observed by the AFM scanning area. Although Figure 5.8 was produced from the AFM measurements for one indent per strain rate and material, the results demonstrated here highlight the potential of the analysis method if further work was performed to understand the changes in pile-up volume, particularly if the total indenter displacement is kept constant across strain rates and materials.

Figure 5.11 and Figure 5.12 show that the magnitude of lattice strains and rotations around the indent in the XY plane increases with irradiation; a slight increase can be observed with strain rate, but the effect is not clear. The increased magnitude of strains and rotations in the irradiated material (± 3 ×10^{-3} to ± 5×10^{-3} in NISX, compared to ± 1 ×10^{-3} to ± 2×10^{-3} in SX) agree with the findings of Das *et al.*,[88] who reported a remarkably similar magnitude of lattice strains and rotations around spherical indents in self-ion irradiated W (1 dpa) and unirradiated W respectively. Furthermore, the authors show that the lattice rotations beneath the indents in the implanted sample, predicted by CPFE, are smaller in magnitude and more confined than in the unimplanted material. The value of ρ measured by HR-EBSD in the lobes around the indents in the 1 dpa sample is between 10^{14} - 10^{15} m^{-2}, which is comparable to the value measured in this thesis in both samples (~10^{14} m^{-2}). Additionally, Yu *et al.*[120] examined self-ion irradiated tungsten using electron channelling contrast imaging (ECCI) and HR-EBSD, revealing the evolution of defect structures from a random distribution of dot-like dislocation loops to long-range, spatially ordered dislocation loops (referred to as 'raft structures') as the dose is increased from 0.1 dpa to 1 dpa. Above 0.32 dpa, a saturation in the strain fluctuations and ρ is reached. This correlates well with the uniformly distributed finer regions of increased ρ interspersed with the background observed in Figure 5.10, for the NISX sample. The consistency in deformation mechanisms observed between this study and the self-ion irradiated studies above indicates that ion irradiation is a useful surrogate to mimic neutron irradiation despite the creation of what is essentially a composite system in ion-irradiated samples.

A more confined plastic zone beneath the spherical indenter was also reported for helium-implanted tungsten using 3D micro-beam Laue diffraction to measure elastic strain in the YZ plane, for which a smaller ε_{xy} shear component, in addition to principal strain components, were measured.[87] This correlates well with studies on behaviour in other irradiated materials using different techniques, such as the case of the indented Fe^{+}-implanted Fe12%Cr alloy examined using cross-sectional TEM, whereby the plastic zone (discernible by a network of dislocations) was visibly suppressed by radiation damage in the irradiated layer.[121] These studies show that whilst surface

observations can provide helpful context for the pile-up phenomena and hardness results in this study, a more comprehensive understanding of the microstructure below the indent can be addressed by cross-sectional characterisation. Nonetheless, the more pronounced lobes and associated increases in the lattice strains and rotations in NISX can be attributed to the constrained deformation zone resulting from evolution of microstructural defects such as the large voids and Re / Os clusters formed during neutron irradiation, both of which are barriers to dislocation movement.[96,89]

Although the presence of pile-up behaviour is usually correlated with materials exhibiting a reduced strain hardening capacity, it is more directly related to the plastic deformation local to the indenter (described in Section 2.3.2). Wang *et al.*[119] have suggested that the pile-up patterns should be interpreted according to local crystallographic criteria rather than global isotropic strain-hardening criteria, as they are a direct result of the localised flow of material occurring from slip in microscopic volumes only. As there is obviously a flow of material to the surface, it is likely that the increased pile-up height in NISX is caused by the restricted growth of the plastic zone beneath the indent. In addition, the formation of dislocation channels has been reported in other neutron-irradiated bcc materials, such as in the case of vanadium where channelling was observed on the $\{112\}$ and $\{110\}$ planes at a damage as low as 0.012 dpa.[111] These cleared channels provide a means for dislocation movement with reduced obstacles, causing a loss of strain hardening.[112] Whilst the barrier strength of the Re-Os precipitates is not currently known, the pile-up and slip steps present (Figure 5.9 (b)) suggest that there could be cleared dislocation channels present local to the indent arising from the annihilation of defects by interaction with the thermally-activated glide of dislocations upon indentation.

Likewise, the SEM image in Figure 5.9 (a) and AFM micrograph of the unirradiated material in Figure 5.3 (a) show four distinct plastic lobes, with channels of depressed material at 5 nm below the rest of the surface; these channels extend to a length of ~30 µm, which is supported by the fact that plastic zone sizes in single crystal tungsten have been observed to reach up to 10 – 40 times the size of the contact radius.[113] This is also consistent with the lack of work hardening seen in the ISS curves

for the unirradiated tungsten in Chapter 4 due to the absence of defects present to inhibit dislocation glide.

Single-crystal W is known to exhibit a pronounced strain rate dependence on hardness at room temperature,[71] where the dominant deformation mechanism is the thermally-activated motion of screw dislocations via the kink-pair mechanism due to the high lattice friction of bcc metals at this temperature. This is reflected in the strain-rate dependency of the stress-strain curves reported in Chapter 4. In this chapter, the ratio of the volume above the surface to the volume below was found to be roughly constant as a function of strain rate for both materials and tip sizes, except for in the case of 5 μm indents in the irradiated sample, where there is an increase in the ratio with strain rate; this could be a measurement artifact resulting from: noise; bulging outside of the field of measurement and pile-up lobes due to tension in the surface; or the enhanced tip asymmetry effects from greater tip displacements using fast strain rates given the constricted deformation zone in NISX. Further rate-controlled spherical indentation studies with strict control of the total indenter displacement would allow comparison of the deformation behaviour at different strain rates to be explored objectively. As a bcc metal, tungsten is rate sensitive, and this effect is accentuated in neutron-irradiated tungsten, as shown by the ISS curves in Chapter 4. In Section 4.3.1, the strain-rate sensitivity was determined from the spherical ISS curves, with values of m = 0.0477 for SX and m = 0.0616 for NISX. The SRS is attributed to the thermally activated glide of screw dislocations, and the barrier to dislocation glide increases with strain rate.[72,70] The activation volume inversely proportional to probability of pinning by statistically stored dislocations (SSDs), and was found to decrease from 3.65 b^3 to 2.12 b^3 after irradiation due to the increased probability of pinning.

5.4 Summary

In this chapter, 5 µm and 10 µm spherical indents in single-crystal W (SX) and neutron-irradiated W (NISX) with $[001]$ out-of-plane orientation were characterised using AFM and HR-EBSD. The objective was to characterise the shape, size and direction of the pile-up morphology induced by nanoindentation and assess the underlying plastic deformation responsible for the observed changes in surface morphology with strain rate and irradiation.

Four-fold symmetry in the pile-up pattern was observed, with distinct lobes along the $\langle 110 \rangle$ directions, corresponding to the four $\langle 111 \rangle$ slip directions on the $\{110\}$ planes. Indentation depth was found to unintentionally increase as a function of strain rate, which may be attributed to the challenging nanoindenter control needed to achieve the strain-controlled spherical nanoindentation method (described further in Sections 3.4.1 and 4.3.3). Even after normalisation, there is a positive trend in pile-up height with strain rate, but it is unlikely that this would be the case if total indenter depth was constant.

AFM revealed that there was a significant increase in pile-up height in NISX compared to SX across all strain rates, despite the change in indent depth. Furthermore, a greater ratio of the volume above the surface to the volume below the surface for NISX – corresponding to the pile-up and indenter trough respectively – provided confirmation that the pile-up was consistently enhanced in the irradiated sample, and can be attributed to a constrained plastic zone beneath the indenter because of radiation-induced defects such as voids and Re/Os-rich clusters in NISX.

The ratio of volume above to volume below was constant for a given strain rate in each material, except for with 5 µm indents in NISX, for which a positive trend with strain rate was seen. The two fastest strain rates also had a greater ratio of volume in the pile-up than indenter pit, which could be due to noise, enhanced tip asymmetry effects at greater displacements within a constricted deformation volume, or some displaced material from the pit not contributing to the four-fold pile-up

local to the indent, and instead causing a gentle protrusion of the surface further afield. Although the volume calculations here were produced from AFM measurements for one indent per strain rate and material, there is potential for the analysis method presented here to add value if further experiments were performed to understand the effect of strain rate and irradiation on pile-up volume, particularly if total indenter displacement is kept constant across strain rates and materials.

Given the observations of pile-up, dislocation channelling is assumed to occur, even in NISX. In the unirradiated sample, this was evidenced by channels of depressed material extending from the lobes along the ⟨110⟩ directions reaching up to 30 μm, whilst slip steps were observed in NISX. Previous observations in other neutron-irradiated bcc metals further suggest that cleared dislocation channels were formed in the neutron-irradiated sample. This localised flow of material is indicative of the reduced strain hardening potential on a local microscopic level, whereas strain hardening is observed on a global level (as observed in the stress-strain curves reported in Chapter 4).

The magnitude of lattice strains and rotations around the indent in the XY plane increases slightly with strain rate in both samples. In NISX, there is also a visible increase in the size, strains and GND density of the lobes around the indent, in addition to the presence of uniformly distributed fine regions of increased density, likely resulting from the defect-riddled microstructure in the sample.

Overall, there was remarkable agreement between this study and observations in unirradiated and self-ion irradiated W in terms of the pile-up pattern around spherical indents, as well as the magnitude and localisation of lattice strains, rotations and GND density. These similarities in deformation behaviour highlight the credibility of using ion irradiation to mimic the damage effects of neutron irradiation.

6 CPFE Modelling of Irradiation Effects in Tungsten

This chapter focuses on the use of crystal plasticity finite element (CPFE) modelling to study the effect of strain rate and neutron-irradiation on the deformation behaviour of single crystal tungsten. The spherical nanoindentation, AFM and HR-EBSD experimental results described in previous chapters have shown a rate dependence in both samples: ISS curves are shifted to higher indentation stresses at faster strain rates and an increase in pile-up with strain rate has been observed. In addition, clear radiation-induced hardening, increased work hardening behaviour and greater pile-up is exhibited in the neutron-irradiated sample.

Four-fold symmetry in the pile-up pattern was observed, with distinct lobes along the ⟨110⟩ directions, corresponding to the four ⟨111⟩ slip directions on the {110} planes. HR-EBSD has shown that as the strain rate is increased, there is not a significant change in GND density nor magnitude of the lattice strains and rotations around the indent in the XY plane, indicating that dislocation glide increased with thermal activation as the strain rate was increased.

Crystal plasticity modelling can allow microstructural-level information such as GND density, lattice rotations and elastic strains to be determined.[78,79] CPFE modelling has been used in this study to simulate spherical nanoindentation in unirradiated and neutron-irradiated tungsten to examine the underlying causes of the changes in deformation behaviour induced by irradiation and strain rate which have been observed through experiments. The simulations also allow the effect of strain rate on pile-up behaviour to be examined using a consistent indenter displacement, given that the total displacement during nanoindentation increased with strain rate due to challenging indenter control.

Building a continuum-level model which is physically-based and can validate experimental results provides a useful tool to understand the behaviour of tungsten in a fusion environment in difficult testing scenarios, such as at very fast strain rates and at high radiation damage levels.

6.1 CPFE Modelling

In crystalline materials, plasticity occurs through crystal glide or slip, whereby the movement of dislocations allows planes of atoms to slide over each other.[122] Experiments have shown that in tungsten, the dominant slip system is $\langle 111 \rangle \{110\}$ at room temperature, with $\langle 111 \rangle$ being the closest-packed direction.[116,117]

The fast (3.2×10^{-3} s^{-1}) and medium (3.2×10^{-4} s^{-1}) strain rate spherical nanoindentation experiments using the nominally 5 µm spherical tip in this thesis were simulated using a 3D strain-gradient CPFE model based on that proposed by Dunne *et al*.[85,86] in which plastic deformation is confined to occur only on crystallographic slip directions. As all of the experiments in this study were performed at room temperature, the CPFE modelling in this thesis considers only the $\langle 111 \rangle \{110\}$ slip systems for tungsten. The modelling in this thesis builds upon the CPFE simulations of nanoindentation in pure tungsten, helium-implanted tungsten, and self-ion implanted tungsten by Suchandrima Das.[123,121,88]

6.1.1 Simulation Set-up

A 3D finite element model was constructed using Abaqus 2016 (Dassault Systèmes, Providence, RI, USA) to simulate the spherical nanoindentation experiments using the nominally 5 µm radius tip (Chapter 4) and inform the characterisation results of these indents using AFM and HR-EBSD, as described in Chapter 5.

The CPFE indentation simulations consisted of a 30×30×30 μm^3 deformable cube and a discrete rigid 3.7 µm radius spherical indenter (calibrated size of the nominally 5 µm radius indenter used) to represent one quarter of the experimental setup, considering the four-fold symmetry of grains with a surface normal of $\langle 001 \rangle$. The 30 µm high simulation block was partitioned into a 3 µm layer on top of 27 µm of material, as shown in shown in Figure 6.1, to achieve finer meshing close to the indented region and optimise the efficiency of the simulation. The boundary conditions imposed on the cube included symmetry on the XZ and YZ surfaces near the indenter and the top surface being indented

was traction free, whilst the remaining XZ, YZ and bottom surfaces were fixed in displacement and rotation. A frictionless 'surface to surface' contact interaction was defined for the interaction between the cube and indenter, as previous studies have demonstrated that the mechanical response between the indenter and sample is nearly independent of friction conditions.[119] The refined finite element mesh of the tungsten cube consisted of 22600, 20-noded, reduced integration 3D quadratic hexahedral elements (C3D20R, using 8 integration points), with an applied edge bias 0.1 to 4 µm, with the smallest elements near the indenter tip within the partition layer.

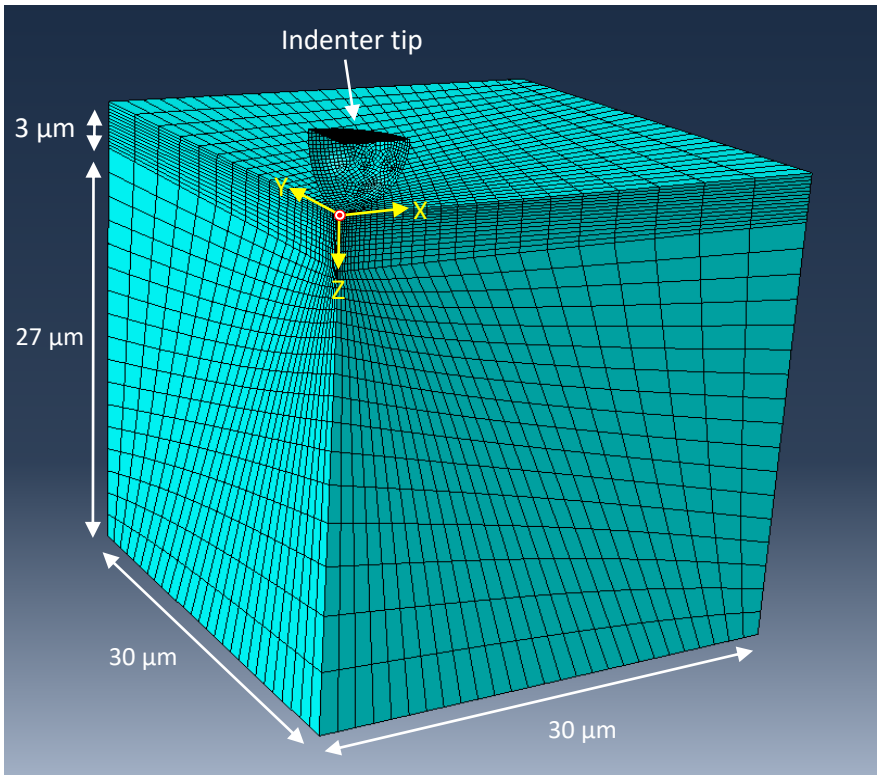


Figure 6.1: *CPFE mesh representing one quarter of the model created in Abaqus to simulation spherical nanoindentation of a tungsten cube with a 3.7 µm radius spherical indenter.*

In order to simulate the experiments, the indenter was subjected to a displacement into the cube in the Z-direction according to the load-displacement curves obtained from nanoindentation. As mentioned in Chapter 5, indentation depth increased as a function of strain rate, but this is likely an artifact resulting from the challenging nanoindenter control needed to achieve the strain-controlled spherical nanoindentation method. This is discussed further in Section 6.2. The respective Z-displacement for the fast and medium strain rate nanoindentation experiments in unirradiated single

crystal tungsten (SX) and neutron-irradiated single crystal tungsten (NISX) are shown in Table 6.1. These displacements were used in the CPFE models to directly simulate the experimental results.

Table 6.1: *Displacement depths from the load-displacement curves of the spherical nanoindentation experiments with a 5 µm radius tip at fast and medium strain rates in both SX and NISX.*

Material	Strain rate / s^{-1}	Maximum displacement depth / nm
SX	3.2×10^{-3}	530
SX	3.2×10^{-4}	430
NISX	3.2×10^{-3}	535
NISX	3.2×10^{-4}	445

The CPFE results were extracted from the surface nodes of the cube and evaluated using a MATLAB script written by Dr Chris Hardie. The script 'concatenates' the array of data outputs from the quarter of the model, building them in the X and Y directions.

6.1.2 CPFE Model

The strain-gradient crystal plasticity model was implemented in an Abaqus user material subroutine (UMAT) reported by Das *et al.*[84,123,121,88] as part of the Tarleton Group's research on Crystal Plasticity at the University of Oxford, and built upon by Dr Nicolo Grilli, Dr Chris Hardie and Dr Eralp Demir. In the UMAT, the mechanical response of the bcc tungsten single crystal under indentation was predicted using a constitutive law incorporating crystallographic slip. A brief description of the constitutive law, originally developed by Dunne *et al.,*[85,86] is provided here.

The multiplicative decomposition of the deformation gradient is obtained by:

$$F = F^e F^p \tag{6.1}$$

where F^e and F^p are the elastic and plastic deformation gradients respectively.

The rate of change of F^p is:

$$\dot{F}^p = L^p F^p \tag{6.2}$$

where L^p is the plastic velocity gradient, which is given by the crystallographic strain rate resulting from dislocation glide on the active slip systems with slip direction s^λ and slip plane normal n^λ as follows:

$$L^p = \sum_{\lambda=1}^{\lambda=12} \dot{\gamma}^\lambda s^\lambda \otimes n^\lambda \tag{6.3}$$

$\dot{\gamma}$ is the crystallographic slip rate on system λ which is given by:

$$\dot{\gamma}^k(\tau^\lambda) = \rho_m b^2 \nu \exp\left(-\frac{\Delta F}{kT}\right) \sinh\left(\frac{(|\tau^\lambda| - \tau_c)V}{kT}\right) \operatorname{sgn}(\tau^\lambda) \tag{6.4}$$

where ρ_m is the density of mobile dislocations, ν is the attempt frequency, b is the magnitude of the Burgers vector, ΔF is the activation energy, k is the Boltzmann constant, T is the absolute temperature, and V is the activation volume. V depends on the spacing between pinning dislocations, l, which is estimated as $\frac{1}{\sqrt{\Psi(\rho_{SSD})}}$, where Ψ represents the probability of pinning determined by the density of statistically stored dislocations (SSD), ρ_{SSD}. τ^λ is the resolved shear stress on a given slip system λ and τ_c is the critical resolved shear stress (CRSS) at any point in the material. When τ^λ is greater than τ_c, slip can occur. Although $\alpha = \rho_m b^2 \nu \exp\left(-\frac{\Delta F}{kT}\right)$ and $\beta = \frac{V}{kT}$ in Equation 6.4 can be treated as fitting constants, they are highly sensitive to changes in their constituent components.

In this CPFE formulation, slip was assumed to occur on the 12 $\langle 111 \rangle \{110\}$ slip systems only, with the slip rate being governed by a physically based constitutive law which considers the thermally activated glide of dislocations through a field of pinning obstacles.[85] τ_c is determined by:

$$\tau_c = \tau_c^0 + C' G b \sqrt{\rho_{GND}} + \tau_s \tag{6.5}$$

τ_c^0, the first term on the right hand side of the equation, is the CRSS of the unirradiated tungsten sample. As the material deforms plastically, the new dislocations (i.e. GNDs) are created to accommodate the resulting lattice curvature.[87,124] The second term accounts for this strain hardening through implementing the Taylor hardening law, whereby τ_c^0 is increased as a function of the evolving GND density throughout the indent, which in turn increases the number of obstacles encountered by

gliding dislocations.[125,124] C' is a geometric hardening factor, G is the shear modulus of tungsten, and ρ_{GND} is the sum of GNDs across all active slip systems. A more in-depth discussion of the GND density calculation via the curl of the plastic deformation gradient tensor can be found in Das *et al.* (2018).[123] GND densities of all 16 dislocation types (12 edge dislocations and 4 screw dislocations) were calculated, with isotropic hardening assumed.

τ_s is a solute hardening parameter (with an initial value of τ_s^0 at t=0) which accounts for the increased resistance to dislocation glide by defects induced by neutron irradiation, causing hardening. For unirradiated tungsten, τ_c is evolved using Equation 6.5 without the τ_s term.

In the irradiated sample, there is a decay in the strength of the radiation-induced defects over time as dislocations cut through them, resulting in the localisation of deformation in channels, and the formation of slip steps.[121] To account for this strain softening, τ_c is decreased at the end of each time increment Δt as a function of the accumulated crystallographic slip, γ:

$$\gamma^{t+\Delta t} = \gamma^t + \sum_{\lambda=1}^{n} \dot{\gamma}^{\lambda} \Delta t \tag{6.6}$$

$$\tau_s^{t+\Delta t} = \tau_s^0 \exp\left(-\frac{\gamma^{t+\Delta t}}{\gamma_s}\right) \tag{6.7}$$

where γ^t and $\gamma^{t+\Delta t}$ are the accumulated slip summed across all slip systems at the start and end of increment Δt, and γ_s is the saturation value of slip strain. Das *et al.* proposed that the rate of defect removal is likely to be proportional to the current defect concentration, resulting in the exponential softening rate given in Equation 6.7.[121]

The parameters τ_c^0 and C' were fitted to the nanoindentation L-D curves, and resulting AFM height profiles and ρ_{GND} and lattice strains measured using HR-EBSD for the unirradiated sample. τ_s^0 and γ_s were fitted to the experimental results of the irradiated sample, with γ_s being chosen to reflect the strain at which the solute strength saturation was reached and transitioned into softening behaviour, as observed in the ISS curves reported in Chapter 4. 0.05 was selected as a general value

across the strain rates modelled. The values of the material parameters used in this CPFE study are detailed in Table 6.2.

Table 6.2: *Mechanical properties for tungsten from literature and CRSS parameters used for fitting load-displacement, morphological and deformation data obtained from nanoindentation, AFM and HR-EBSD experiments.*

Material Property	Value	References
Elastic modulus E	421 GPa	Featherston and Neigbours,[126] Bolef and De Klerk,[127] Ayres *et al.*,[128] Klein and Cardinale[129]
Shear modulus G	164.4 GPa	Featherston and Neigbours,[126] Bolef and De Klerk,[127] Ayres *et al.*,[128] Klein and Cardinale[129]
Poisson's ratio v	0.28	Featherston and Neigbours,[126] Bolef and De Klerk,[127] Ayres *et al.*,[128] Klein and Cardinale[129]
Burgers vector b	2.7×10^{-10} m	Dutta and Dayal[130]
Activation energy ΔF	3.4559×10^{-20} J	Chosen to reduce strain-rate sensitivity (compared to $\dot{\varepsilon}$ above 10^3 s^{-1})[88]
Boltzmann constant k	1.381×10^{-23} J / K	Sweeney *et al.*[131]
Temperature T	298 K	Room temperature assumed during experiments
Attempt frequency ν	1×10^{11} s^{-1}	Sweeney *et al.*[131]
Density of statistically stored dislocations ρ_{SSD}	1×10^{12} m^{-2}	See below*
Density of mobile dislocations ρ_m	1×10^{10} m^{-2}	See below*
Probability of pinning Ψ	0.857×10^{-2}	Value chosen and kept fixed
Critical resolved shear stress τ_c^0	360 MPa	Fitted to experimental data of unirradiated sample
Geometric hardening factor C'	0.2	Fitted to experimental data of unirradiated sample
Initial value of solute hardening from defects τ_s^0	750 MPa	Fitted to experimental data of irradiated sample
Saturation value of slip strain γ_s	0.05	Fitted to experimental data of irradiated sample

** In the GND density maps presented in Chapter 5, the background density was found to be on the order of ~10^{13} m^{-2} by HR-EBSD. For the present CPFE study, it has been assumed that ρ_{SSD} is smaller than the ρ_{GND} estimate, and that ρ_m is at least two orders of magnitude smaller than ρ_{SSD}.*

Plastic strain increments are computed by summing the contribution of the slip rates over the slip systems using symmetric part of the Schmid tensor, $\boldsymbol{S}^{\lambda}$:

$$\Delta\varepsilon_p = sym\left(\sum_{a=1}^{nslip} \dot{\gamma}^{\lambda}\, \boldsymbol{S}^{\lambda}\right)\Delta t \tag{6.8}$$

where $\Delta\varepsilon_p$ is the plastic strain increment. The elastic strain increments, $\Delta\varepsilon_e$, are obtained by subtracting $\Delta\varepsilon_p$ from the total strain increment, $\Delta\varepsilon$, as follows:

$$\Delta\varepsilon_e = \Delta\varepsilon - \Delta\varepsilon_p$$

The elastic strains are converted to a 3 x 3 matrix, ΔE_e:

$$\Delta E_e = \begin{bmatrix} \Delta\varepsilon_{e11} & \Delta\varepsilon_{e12}/2 & \Delta\varepsilon_{e13}/2 \\ \Delta\varepsilon_{e12}/2 & \Delta\varepsilon_{e22} & \Delta\varepsilon_{e23}/2 \\ \Delta\varepsilon_{e13}/2 & \Delta\varepsilon_{e23}/2 & \Delta\varepsilon_{e33} \end{bmatrix} \tag{6.9}$$

The elastic strain increment is transformed to the crystal reference, ΔE_e^c, using the crystal to sample transformation, g:

$$\Delta E_e^c = g\, \Delta\varepsilon_e\, g^T \tag{6.10}$$

The strain increments at the crystal reference are vectorised as follows:

$$\Delta\varepsilon_e^c = \left[\Delta E_{e11}^c \quad \Delta E_{e22}^c \quad \Delta E_{e33}^c \quad 2 * \Delta E_{e12}^c \quad 2 * \Delta E_{e13}^c \quad 2 * \Delta E_{e23}^c\right]^T \tag{6.11}$$

Finally, the strain increments are added to the former elastic strain at the crystal reference:

$$E_e^c = E_e^c(t) + \Delta E_e^c \tag{6.12}$$

As only one quarter of the indentation set-up was modelled, anti-symmetry was applied to the shear strain components.

6.1.3 Mesh Convergence

Mesh refinement and convergence is an important consideration for computational simulations to ensure the results produced are adequate for purpose, with a coarse mesh potentially yielding inaccurate analysis results. The numerical solution produced tends toward a near-constant value as the mesh density is increased, but also requires a greater level of computational resource to achieve this additional level of accuracy. A balance must therefore be struck between achieving the optimum solution and computational time. Mesh convergence is widely considered to be attained when further mesh refinement produces negligible (< 3 – 5 %) change in the solution.

The smallest element size in this study was 100 nm, using an applied edge bias 0.1 to 4 µm. Less than 1 % change in load was achieved in the maximum load under the indenter tip as the smallest element was reduced from 150 nm to 100 nm. However, at 150 nm, although the GND density showed less than 5 % change in value, the GND fields were less defined and boxier compared to the results of the HR-EBSD maps.

Reducing the minimum element size to 50 nm (the same value as the step size during HR-EBSD) was not possible due to the computational memory required. Given that 100 nm was sufficient to achieve less than 1 % change in load and achieve a reasonable match in shape and values of the experimentally-obtained GND density fields, the smallest element size of 100 nm was kept. Achieving further convergence in GND density could require greater computational intensity and not necessarily be achievable for certain models.

6.2 Nanoindentation Method Pile-Up Artifact

As shown in Chapter 4 (Figure 4.7 (g) and (h)), the total strain achieved through spherical nanoindentation using the 3.7 µm radius tip (nominally 5 µm) increases with strain rate. The method performed was intended to reach a total strain of 0.1, which would equate to a final displacement of 525 nm for the geometry of the tip used (as per Equation 3.11). Only the ISS curves measured in both

SX and NISX at the fast strain rate achieve a total strain of 0.1. In addition, Table 6.1 shows that the total indenter displacement for the fast strain rate test was 530 nm, whilst that of the medium strain rate was 430 nm.

However, the total indenter displacement into the surface – and thus maximum residual indentation depth (Table 6.1) – increased as a function of strain rate in the spherical nanoindentation experiments conducted in this study. This has been attributed to the challenging indenter control required to achieve the strain-controlled spherical nanoindentation method used. The maximum pile-up height produced by nanoindentation also increased 32-53 nm in SX and 44-110 nm in NISX respectively as the strain rate was increased from slow (3.2×10^{-5}) to fast (3.2×10^{-3}).

To gain a better understanding of the effect of strain rate on the indentation pile-up, CPFE simulations were performed to 430 nm (the final displacement achieved in the medium strain tests) using both the fast and medium strain rate. The height profile data predicted by modelling is shown in Figure 6.2; a maximum pile-up height of 57 nm and 53 nm are achieved for the medium and fast strain rates respectively.

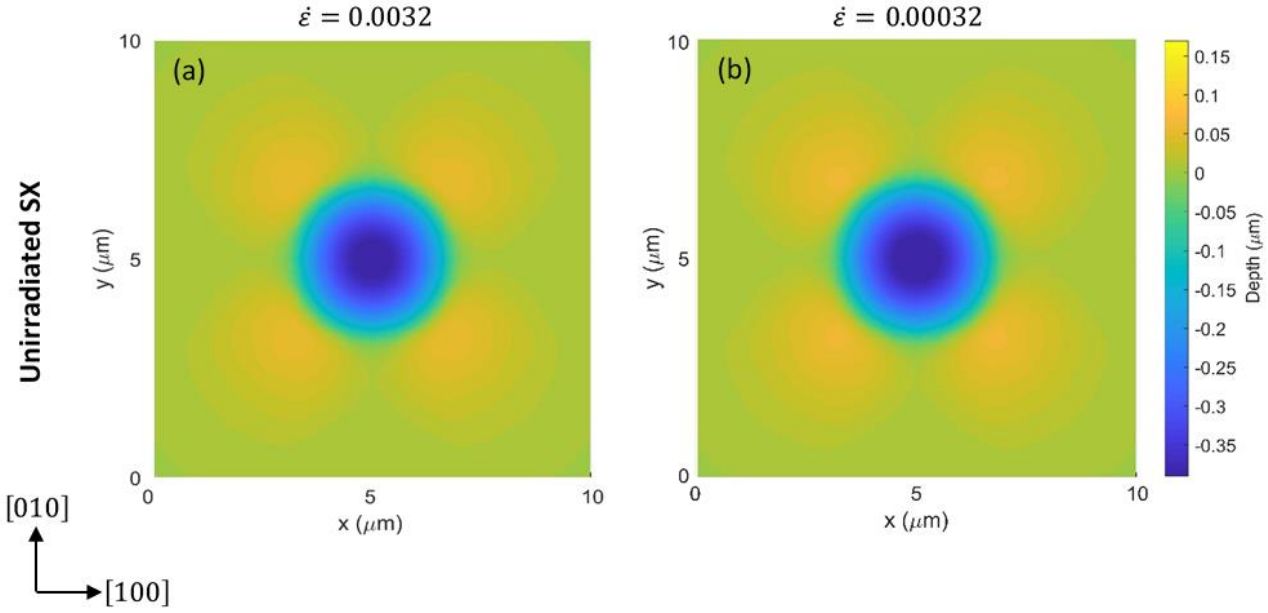


Figure 6.2: *CPFE predictions of height profile data for spherical indents performed in the [001] orientation with a nominally 5 µm radius indenter at (a) fast and (b) medium strain rates, to the same indentation depth of 430 nm.*

This indicates that if the total displacement depth is kept fixed, a very similar amount of pile-up is produced by nanoindentation. There is, however, a change in the indenter load; the load-displacement curves for these indentation simulations in Figure 6.3 show that a maximum load of 57.2 mN was reached using the medium strain rate, compared to a load of 61.7 mN using the fast strain rate.

For the purpose of gaining a better understanding of the spherical nanoindentation experimental results, the simulations discussed in Section 6.3 were performed to the same displacement depth as in the experiments. Nonetheless, it should be noted that if the total displacement is fixed at the same value during experimentation, then the pile-up produced at different strain rates should be constant.

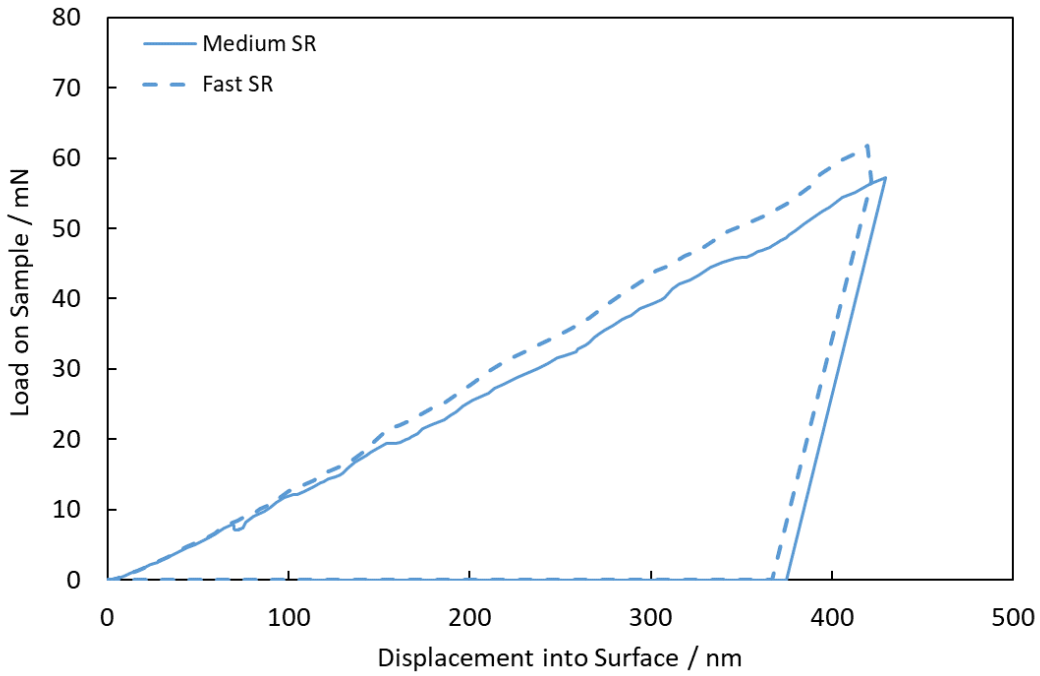


Figure 6.3: *Load-displacement curves predicted by CPFE simulations for spherical nanoindentation at fast and medium strain rates to the same indentation depth of 430 nm.*

6.3 CPFE Results

6.3.1 Load-Displacement Curves

Figure 6.4 shows the load-displacement curves for SX and NISX samples obtained from spherical nanoindentation and the corresponding CPFE simulations in the [001] orientation, at both fast and

medium strain rates. The nanoindentation curves were taken from one measurement due to the pop-ins observed. As discussed in Section 4.3.3, pop-ins are indicative of the onset of plastic deformation and associated nucleation of dislocations when the material is relatively defect-free.[98] Conversely, the microstructure of the neutron-irradiated sample contains radiation-induced defects which allow for easier nucleation of dislocations.

With exception of the pop-ins, there is strong agreement between the CPFE-simulated curves and experimental curves. As shown in Table 6.3, the difference between the peak load achieved by nanoindentation modelling ranges from 0.26 % to 5.98 %. In general, the discrepancy is slightly smaller for the medium strain rates than fast. Despite the simulation correctly predicting the nanoindentation experimental results, it must be noted that the CRSS of SX W, τ_c^0, measured from uniaxial tests ranges from 85–125 MPa over the strain rates considered in this study ($\tau_c^0 = 360$ MPa in the simulations).[132] The increase in load in NISX compared to SX occurs in line with the experiment using 750 MPa for the initial value of solute hardening, τ_s^0, and 0.05 for the saturation value of slip strain, γ_s.

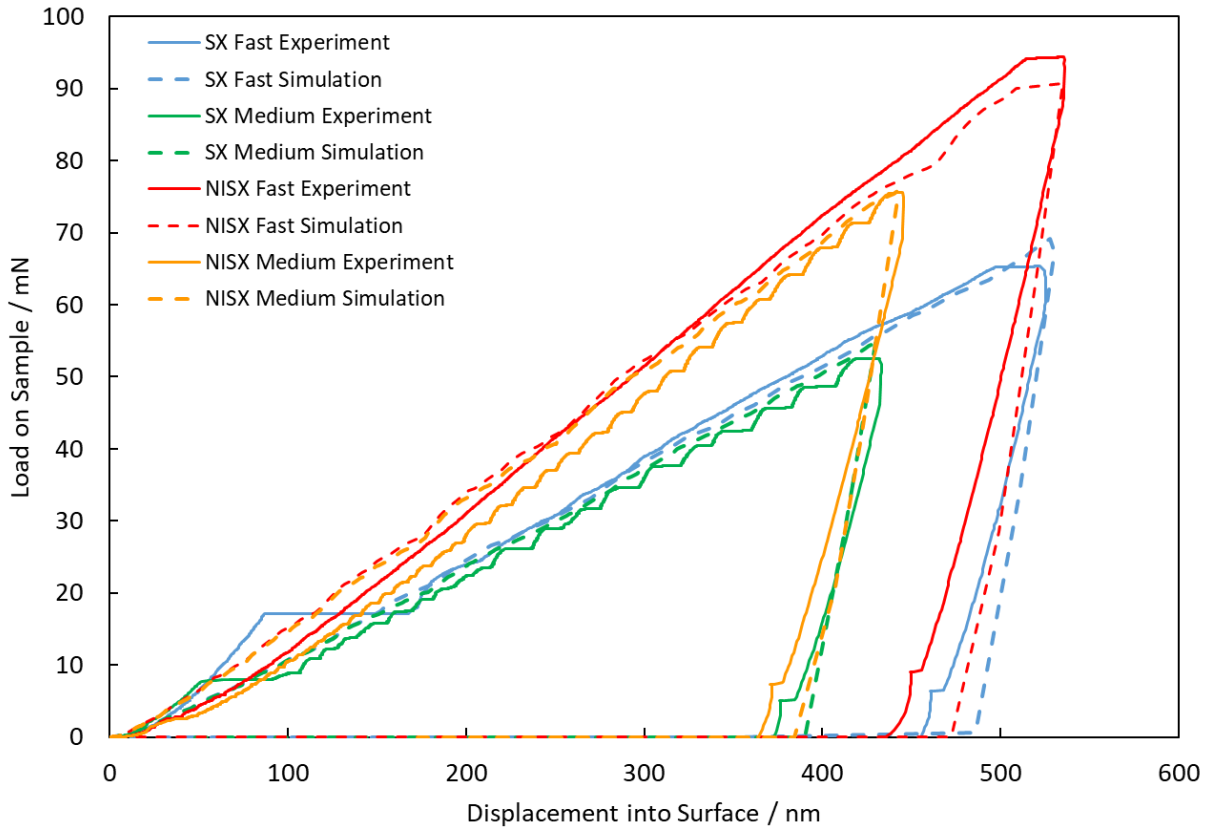


Figure 6.4: *Load-displacement curves for SX and NISX samples obtained from spherical nanoindentation and CPFE simulations at fast and medium strain rates.*

Table 6.3: *Comparison of peak load reached by spherical nanoindentation experiments and CPFE predictions with a 5 µm radius tip at fast and medium strain rates in SX and NISX.*

Material	Strain rate / s^{-1}	Peak load in nanoindentation / mN	Peak load in model / mN	% difference between experiment and model
SX	3.2×10^{-3}	65.2	69.1	5.98
SX	3.2×10^{-4}	52.6	54.7	3.99
NISX	3.2×10^{-3}	94.4	90.7	3.92
NISX	3.2×10^{-4}	75.5	75.7	0.26

6.3.2 Indentation Surface Morphology

The surface height profiles after spherical nanoindentation in the [001] direction as measured by AFM are shown alongside those predicted by CPFE simulations in Figure 6.5. The four-fold symmetry in the pile-up pattern observed from experiment has been well-captured by the model, with regions of increased pile-up along the $\langle 110 \rangle$ directions, consistent with expectation that deformation is confined to the four $\langle 111 \rangle$ slip directions on the $\{110\}$ planes. There is also generally good agreement between the maximum residual pile-up height from nanoindentation and the model (Table 6.4), with CPFE correctly predicting an increase in pile-up height following irradiation, which is attributed to the restricted growth of the plastic zone beneath the indent.

As the spherical nanoindentation method produces the artifact whereby a greater indentation depth, and thus greater pile-up, is produced in the experiment (detailed in Section 6.2), comparison of pile-up height between the strain rates without the same total displacement is not hugely meaningful. Although relatively good quantitative agreement in pile-up height is observed between the CPFE and AFM results, the morphology of the pile-up produced is not quite accurate. In the simulated unirradiated sample, the area covered by the pile-up lobes is slightly too large, whilst in the neutron-irradiated case, the pile-up region is slightly too compact.

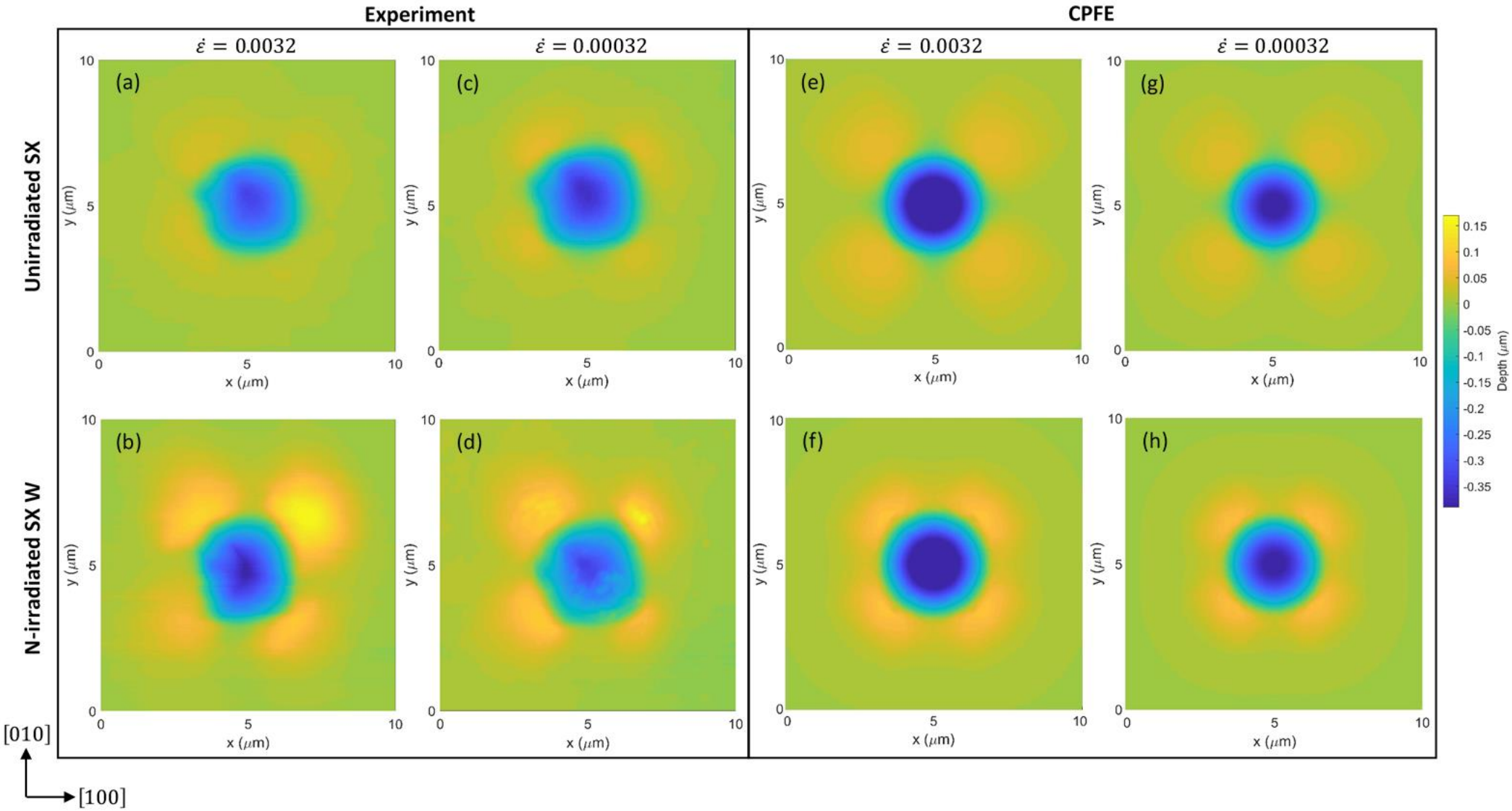


Figure 6.5: *Surface profiles for spherical indents performed with a nominally 5 μm radius indenter at fast and medium strain rates alongside surface height predictions from CPFE calculations. AFM micrographs of indents at fast and medium strain rates are shown respectively for SX in (a) and (c), and for NISX in (b) and (d). CPFE predictions of surface height at fast and medium strain rates are shown respectively for SX in (e) and (g), and for NISX in (f) and (h).*

Table 6.4: *Comparison of maximum pile-up height around spherical indents measured by AFM and predicted by CPFE simulations at fast and medium strain rates in SX and NISX.*

Material	Strain rate / s^{-1}	Maximum pile-up height (AFM) / µm	Maximum pile-up height in model / µm	% difference between experiment and model
SX	3.2×10^{-3}	0.053	0.053	0
SX	3.2×10^{-4}	0.042	0.046	9.52
NISX	3.2×10^{-3}	0.110	0.092	16.36
NISX	3.2×10^{-4}	0.087	0.085	2.30

6.3.3 Elastic Strain Fields

Figure 6.6 (a) – (d) show the ε_{xy} component of the residual elastic strain on the sample surface for SX and NISX as determined by HR-EBSD, which is a measure of the in-plane shear strain around the indent. At the medium strain rate, there is an increase in the strain magnitudes in the lobes from ± 1 $\times10^{-3}$ to ± 2×10^{-3} after irradiation, and from ± 2 $\times10^{-3}$ to ± 4×10^{-3} at the fast strain rate. The size of the strain fields around the indents (corresponding to the lobe regions) increases with strain rate for both materials. Similarly, the CPFE predictions of ε_{xy} in Figure 6.6 (e) – (h) show that there is an increase in the strain localisation as the strain rate is increased, although the magnitude stays fairly constant. As mentioned previously, drawing comparisons between strain rates when the final displacement depth is different is not particularly meaningful.

The magnitude of strain in the lobes for all four maps ranges from ± 1 $\times10^{-3}$ to ± 5×10^{-3}, but the localisation of the lobes in SX is more narrow and elongated compared to NISX, whereas the strain fields are more compact and rounded in the latter material. This change in localisation is not as clear to observe in the HR-EBSD maps, which could be a result of measurement noise or sample cleanliness, or due to the smaller strain magnitudes and localisation in the experiment.

Additionally, in the CPFE calculations, the localisation of strains is too large compared to the experiment for the unirradiated case, although there is relatively good agreement for the irradiated material. The magnitudes of the strains produced in the model are also slightly too large, but a match

in the order of magnitude is achieved. Overall, the predicted pattern and magnitude of negative and positive lobes for the ε_{xy} strain component is consistent with HR-EBSD measurements.

6.3.4 GND Density

The GND density maps measured by HR-EBSD and predicted by CPFE are shown in Figure 6.7. There is strong agreement in the ρ_{GND} distribution as well as quantitatively in the absolute values measured (~10^{14} m^{-2}), through experiments and calculated by CPFE. In SX, the zones of increased density correspond to the edges of the four lobes along the ⟨110⟩, whilst in NISX, the higher density regions cover the entirety of the lobes.

It is clear that in the GND density maps produced by both the experiment and model that the size of the plastic zone surrounding each ident is smaller in the irradiated sample, which is consistent with the surface height profile and elastic strain maps reported in this work.

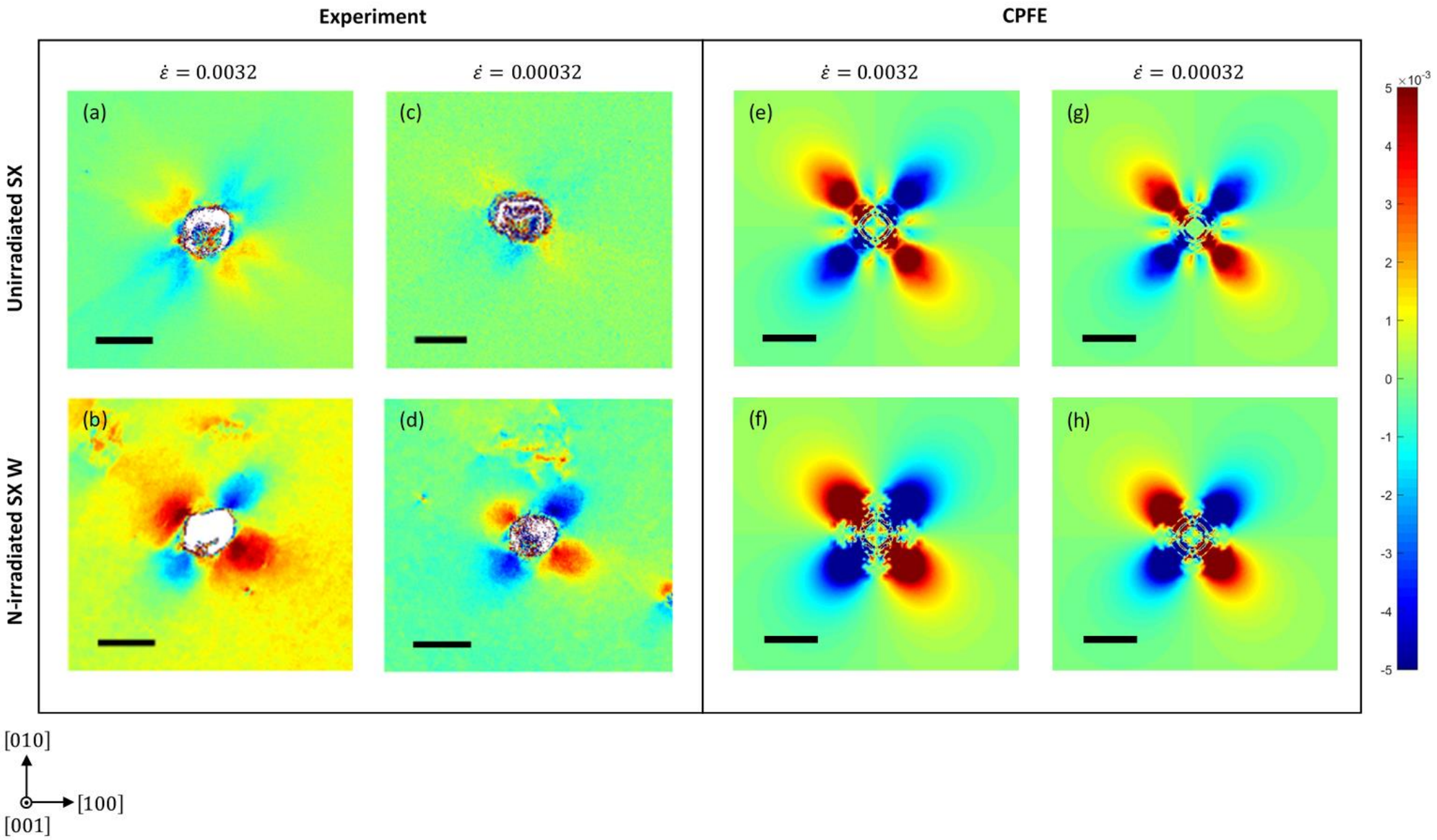


Figure 6.6: *ε_{xy} component of the residual deviatoric lattice strain in the XY plane (sample surface) determined by HR-EBSD for indents performed with a nominally 5 µm radius indenter at fast and medium strain for SX in (a) and (c), and for NISX in (b) and (d). Elastic strain predictions from CPFE calculations at fast and medium strain rates are shown respectively for SX in (e) and (g), and for NISX in (f) and (h). Both samples were indented in the [001] orientation. Scale bars correspond to 5 µm.*

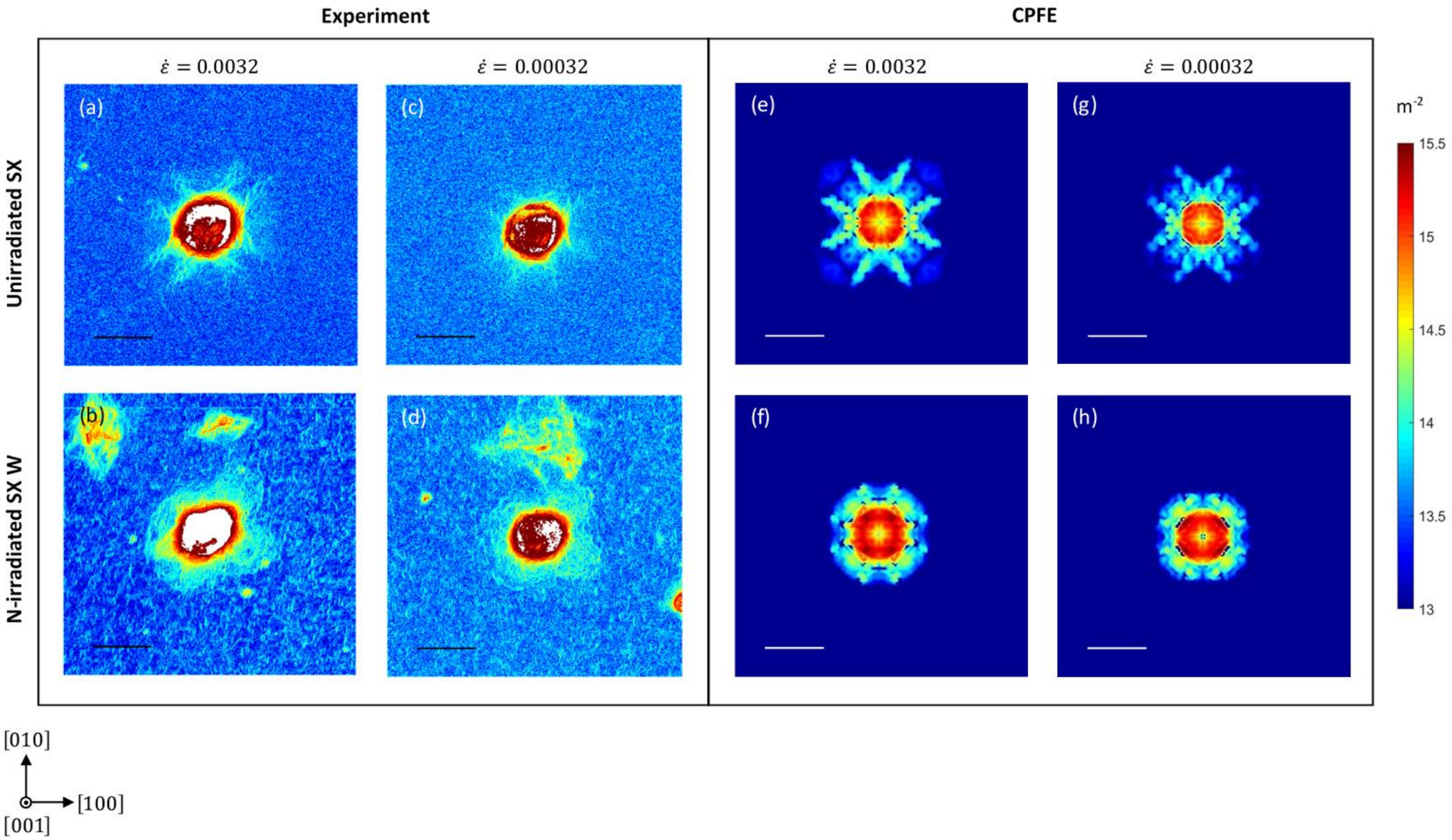


Figure 6.7: *Total GND density (ρ_{GND}) maps determined by HR-EBSD in the XY plane for indents performed with a nominally 5 µm radius indenter at fast and medium strain rates respectively for SX in (a) and (c), and for NISX in (b) and (d). Predictions from CPFE calculations at fast and medium strain rates are shown respectively for SX in (e) and (g), and for NISX in (f) and (h). Colour scale units are in log(ρ_{GND}) with ρ_{GND} in m^{-2}. Scale bars correspond to 5 µm.*

6.4 Discussion

Although the strain-rate sensitivity of spherical indentation stress-strain curves has been studied previously,[58,75] the effect of strain rate on deformation behaviour is not comprehensively understood, particularly in neutron-irradiated tungsten.

A strain-gradient CPFE model was used to simulate the mechanical and deformation behaviour observed from spherical nanoindentation in SX and NISX using tests using a 3.7 µm radius tip (nominally 5 µm) for comparison with the experimental results presented in Chapters 4 and 5. A simulation study of the loading behaviour, pile-up morphology and plastic deformation was performed, with the model employing a physically-based slip law coupled with GND evolution as a strain hardening mechanism.

Excluding the pop-in behaviour, there is a strong match between the simulated load-displacement curves and experimental curves from nanoindentation. The increased peak indentation load in NISX compared to SX occurs as a result of the radiation-induced hardening from defects as reported previously in neutron-irradiated tungsten[76] and ion-implanted tungsten.[81,133] As shown in Table 6.3, good quantitative agreement is achieved, with the difference between the peak load reached by nanoindentation and modelling ranging from 0.26 % to 5.98 %.

It appeared that 750 MPa was the most suitable initial value of solute hardening from defects, τ_s^0, in order to achieve close agreement with the experiment. Using 500 MPa and 600 MPa respectively led to peak loads of 70.4 mN and 72.7 mN at the medium strain rate. Varying the value of γ_s, the saturation value of slip strain, between 0.05 and 0.08 produced negligible effects on the peak load.

In general, there is a smaller mismatch between peak loads at the medium strain rates than fast strain rates, indicating that the thermally activated part of the slip law, α, (Equation 6.4) could benefit from further refinement. Tungsten is strain-rate sensitive, and this is emphasised in neutron-irradiated tungsten, as shown by the ISS curves in Chapter 4. This can be attributed to the thermally activated

motion of screw dislocations (dictated by the Peierls barrier), thus the barrier to dislocation glide increases with strain rate.[72,70] In Section 4.3.1, the strain-rate sensitivity was determined from the spherical ISS curves, with values of m = 0.0477 for SX and m = 0.0616 for NISX.

Similarly, the value of β could also be studied in a more comprehensive manner; β is related to the activation volume, which is dependent on the spacing between pinning dislocations and inversely proportional to probability of pinning by SSDs. V reduced from 3.65 b^3 to 2.12 b^3 after irradiation due to the increased probability of pinning. In this study, the value of V was unchanged across SX and NISX. However, it should be noted the slip law is extremely sensitive to changes in α and β, thus they were kept constant using the values in Table 6.2 as they are constitutive material properties which should be constant for each material.

As discussed in Section 6.2, if the total displacement is fixed at the same value during experimentation, then the pile-up produced at different strain rates should be constant. The increased pile-up as a function of strain rate previously seen in the spherical nanoindentation experiments performed was a result of the rate-controlled method which gave artificially rise to greater total displacement depths at faster strain rates. There is, however, an increased peak load achieved at faster applied strain rates.

The CPFE model correctly predicted the pile-up morphology around indents in SX and NISX according to the AFM surface profiles, with good quantitative agreement in maximum pile-up height. This pile-up pattern has been previously observed by AFM and SEM micrographs around nanoindents in $[001]$-orientated single crystal W and Cu.[65,119] Notably, the four-fold symmetry and increase in pile-up following irradiation also matches well with the surface height profiles measured by AFM and predicted by CPFE simulations for indents in unimplanted and helium-implanted tungsten single crystal in the $[001]$ orientation, as reported by Das *et al*.[121] The simulated and measured GND density values (~10^{14} m^{-2}) are also consistent with those reported in this study.

As is the case with Figure 6.5, the surface profiles published by the authors demonstrate that the pile-up region in the irradiated material is slightly too compact.[121] The same value of solute hardening was used for the helium-induced defects as the neutron radiation-induced defects in this study (750 MPa). Despite leading to strong agreement in load-displacement curves for Das *et al*. in another body of work focused on the same simulations,[65] the size of the region beneath the indenter with increased GND density in cross-section is noticeably larger in the simulation compared to HR-EBSD. One of the challenges in a CPFE study such as this is the fact that a combination of the unirradiated material's CRSS, a geometric hardening factor, slip law parameters, radiation solute hardening and saturation strain can be used to fit the data. Therefore, although strong agreement is achieved for load-displacement curves, pile-up height, and GND density distribution at the indentation surface (XY plane) in this study's simulations, it is vitally important to characterise the cross-section of indents to examine the plastic zone and further optimise the parameters in the CPFE model.

The spatial confinement of the ε_{xy} strain fields calculated by CPFE in NISX compared to SX (Figure 6.6) are consistent with the strains measured by HR-EBSD and can be attributed to the constrained plastic deformation zone arising from the neutron radiation-induced microstuctural defects, such as large voids and Re-Os clusters, which pose barriers to dislocation glide. [96,89] The magnitudes are slightly too high in the simulation for SX although the same order of magnitude is achieved, but quantitative agreement is sought for NISX. A similar observation in the localisation of strain to more compact and less elongated lobes, has been observed in self-ion irradiated tungsten.[70]

The tungsten studies referred to in this section, as well as the current work, have been simulated using a 3D strain-gradient CPFE model based on that proposed by Dunne *et al*.[85,86] whereby plastic deformation is confined to occur only on crystallographic slip directions. Furthermore, the CPFE formulation for the irradiated materials used in this study was based on the hypothesis of increased hardening from radiation-induced defects coupled with the removal of these obstacles by the progressive passage of dislocations over time.[121,65] This leads to slip channels cleared of defects which can accommodate deformation in the plastic zone near the indent through increased material flow,

causing a loss of strain hardening and greater pile-up.[112] The strong agreement of the simulation results in this work indicate that these assumptions are correct, as the deformation behaviour characterised by nanoindentation, HR-EBSD and AFM has been well captured.

The parameters relating to strain-rate sensitivity in the model could benefit from further refinement and understanding, but good quantitative agreement is seen across the fast (3.2×10^{-3} s^{-1}) and medium (3.2×10^{-4} s^{-1}) strain rates simulated. For example, activation energy, ΔF, which is used in the calculation of α in the slip law was chosen to reduce strain-rate sensitivity compared to $\dot{\varepsilon}$ above 10^3 s^{-1}).[88] This assumption can also be considered correct, because it is consistent with the simulation results in Section 6.2 to explore the effect of strain rate when the total displacement is kept constant. As a very similar level of pile-up is produced at both medium and fast strain rates, the effect of strain rate on dislocation glide is minimal. Interestingly, Das *et al*. discovered that the overall effect of irradiation-induced defects on hardness, surface pile-up, and thus glide dislocation mobility, does not change significantly between 0.1 dpa and 1 dpa using self-ion irradiated tunsgten.[70] This indicates that whilst tungsten does show some level of strain-rate sensitivity, dislocation mobility is not highly sensitive to changes in rate and saturates at a given damage level.

6.5 Summary

A CPFE model was used to simulate spherical nanoindentation experiments in unirradiated and neutron-irradiated tungsten to probe the underlying effects of irradiation and strain rate on deformation behaviour observed through AFM and HR-EBSD.

Strong quantitative agreement was obtained for CPFE predictions of load-displacement curves across the fast (3.2×10^{-3} s^{-1}) and medium (3.2×10^{-4} s^{-1}) strain rates in both materials, although discrepancies between error differences across the two strain rates could potentially be refined through further study on the strain-rate sensitivity effects of varying α in the slip law. Likewise, the effect of changing β in the slip law could be explored further, as this value is related to the activation

volume which is dependent on the spacing between pinning dislocations; β was kept constant in this study for SX and NISX.

The pile-up height and subsequent increase after irradiation is consistent between the CPFE and AFM results. Similarly, the four-fold symmetry in the pile-up morphology produced by the model is in strong agreement with experiments and wider literature. In the neutron-irradiated case, the pile-up lobe regions are slightly too compact. One of the challenges of CPFE modelling of this kind is the ability to use the unirradiated material's CRSS, geometric hardening factors, radiation solute hardening, saturation strain or the slip law to fit the data. Thus, parameters which lead to strong agreement with one measure of deformation behaviour at a given condition may not match well with a different strain rate.

Nonetheless, the absolute values and distribution of GND density predicted by the model were in strong agreement with the experiment. Similarly, the correct order of magnitude in the negative and positive in-plane shear strains was predicted, in addition to the formation of a more compact, less elongated strain field in the irradiated sample compared to the unirradiated state.

The pile-up, strain and GND density maps simulations provide evidence for a reduced plastic zone size in the irradiated material, resulting from defect-free channels which provide a means for dislocation movement. The set of parameters fitted to the experimental results were thus successful in simulating the increased pile-up height and constraint of the plastic zone observed experimentally, whilst providing clarity on the subtle rate effects.

In addition, the effect of strain rate on pile-up behaviour was examined using a consistent final indenter displacement and thus strain for a 3.7 µm radius tip (nominally 5 µm), given that the increase in total displacement with strain rate was an artifact of the rate-controlled spherical nanoindentation method. Notably, for a fixed displacement, the pile-up produced at different strain rates should be constant, although a slightly higher peak load was achieved at the faster strain rate. This indicates that the effect of strain rate on dislocation mobility is minimal.

7 Summary, Conclusions and Future Work

The aim of this thesis was to study the effect of strain rate and neutron irradiation damage on the performance of tungsten in a fusion reactor such as DEMO using unirradiated and neutron-irradiated single crystal tungsten samples with [001] out-of-plane orientation (referred to as 'SX' and 'NISX' respectively). The NISX sample was irradiated to 1.67 dpa at 900 °C, with a final composition of W - 1.20 ± 0.11 at.% Re - 0.11 ± 0.05 at.% Os - 0.03 ± 0.01 at.% Ta).

These aims were achieved by studying the stress-strain, hardening and deformation behaviour using a combination of techniques. A summary of the findings in this thesis is detailed below.

7.1 Spherical Indentation Stress-Strain Behaviour

Constant strain rate spherical nanoindentation experiments using tips of 5 µm and 10 µm radius were executed at strain rates of 3.2 x 10^{-3} s^{-1}, 3.2 x 10^{-4} s^{-1} and 3.2 x 10^{-5} s^{-1} ('fast', 'medium' and 'slow'), to examine the indentation stress-strain (ISS) response of SX and NISX. Berkovich nanoindentation was also performed as a baseline measure of hardness, and showed a radiation-induced hardening of 2.2 GPa at 500 nm displacement.

The ISS curves for SX showed an absence of work hardening in addition to the presence of large pop-ins. Pop-ins can result from the lack of defects in a high purity single crystal tungsten sample such as SX, causing dislocations to be nucleated in a burst upon nanoindentation, and enabling subsequent dislocation glide and channelling.

Significant strain hardening was observed for NISX as demonstrated by a steep hardening region in the ISS curves; this can be attributed to the radiation-induced microstructural defects which pose barriers to dislocation motion, such as the transmutation-induced Re-Os precipitates, in addition to dislocations and voids previously reported from studies on the same irradiated sample.[108,105,107] The steep hardening region is followed by a strain softening or plateau region resulting from a decay in

the strength of the defects over time as dislocations cut through them, enabling dislocation channelling to occur, as has been observed in neutron irradiated bcc metals.

Multiple analysis methods were used due to the difference in ISS curve shape for SX and NISX, as well as the presence of pop-ins in both materials, manifested as strain bursts followed by elastic unloading. In SX, the lack of plastic data until strains after the pop-in did not allow the yield stress to be inferred from the point at which the elastic Hertzian response intersects with a straight line through the flow portion of the curve, as described in the work of Zhu et al.[43] 'Method 2' of extracting the YS (involving back-extrapolation of the hardening portion of the flow curve) appeared most effective in determining the transition from elastic to plastic deformation and providing consistent comparison with results in literature which used Zhu's method.

A clear strain rate dependency in the indentation yield stress (YS) was observed. In SX, there was an increase in YS from 4.22 to 5.64 GPa as the strain rate was increased from slow to fast using the 5 µm tip, whilst the YS increased from 4.46 GPa to 5.70 GPa in NISX. Using the 10 µm tip, the YS increased from 4.90 GPa to 5.84 GPa in SX and 5.22 to 6.75 GPa in NISX with an increase in strain rate from slow to fast. Despite the increase in YS with strain rate, the work hardening behaviour remains consistent as a function of strain rate, as demonstrated by an upwards shift in the flow portion of the ISS curves in Chapter 4.

Both tip results showed a definite increase in strain-rate sensitivity, *m*, and reduction in activation volume, *V*, after irradiation. *m* increased from 0.0477 to 0.0616 using the 5 µm tip, and from 0.0324 to 0.0427 using the 10 µm tip, indicating the presence of an indentation size effect. These values of *m* reflect the high lattice friction in bcc materials at room temperature whereby deformation is controlled by the thermally activated motion of screw dislocations via the kink-pair mechanism.[71] The measured SRS using the 5 µm tip is in strong agreement with values reported for CSR tests on single crystal W with $\{001\}$ surface orientation ion-irradiated to 2 dpa.

The reduction in V after irradiation from 3.65 b^3 to 2.12 b^3 for the 5 µm tip, and 5.93 b^3 to 2.89 b^3 for the 10 µm tip, indicates that the dislocation glide is reduced by radiation-induced microstructural obstacles such as dislocations and voids in NISX and the probability of pinning is increased.

There is strong alignment between the values of m and V obtained from this study and those reported on ion-irradiated single crystal to 2 dpa,[103] although the damage mechanisms caused by neutron and ion irradiation are not directly comparable, particularly as different microstructures are produced and there was no transmutation in the ion-irradiated sample. Even in an ion-irradiated sample of the same composition as NISX, there are smaller Os clusters and voids present compared to the large Re/Os clusters and voids observed in the neutron-irradiated sample.[96] The agreement on the influence of strain rate on mechanical properties can be attributed to a combination of a slightly greater damage level in the ion-irradiated sample as well as the effect of dislocation loops; however, further work is needed to investigate the competing roles of dislocation loops, voids and precipitates. Nonetheless, this result demonstrates the credibility of using ion irradiation as a useful materials selection tool for various irradiation environments owing to the fact that observed mechanical property changes are comparable with those induced by neutrons at comparable damage levels.

The hardness values calculated at 8 % strain in the spherical ISS curves for direct comparison with Berkovich strongly agreed with the Berkovich hardness values. As the strain rate was increased from slow to fast, the increase in hardness ranged from 1.53 GPa to 2.44 GPa for the 5 µm radius tip, and 2.41 GPa to 3.22 GPa for the 10 µm radius tip respectively. The 5 µm tip spherical hardness results from the medium strain rate of 3.2 x 10^{-4} s^{-1} matched the Berkovich results very closely. Furthermore, the irradiation-induced hardening is consistent with other studies in tungsten neutron-irradiated to similar damage levels and with similar transmutation rates, as well as in self-ion irradiated tungsten.

Overall, the spherical indentation used in this work successfully enabled the production of ISS curves, and extraction of yield stresses, work hardening behaviour, strain-rate sensitivity and activation volume. However, this method requires refinement to obtain same total strain and thus

indenter displacement across strain rates to allow a systematic study of the deformation behaviour exhibited in each material. In addition, the use of a larger tip can avoid the presence of large pop-ins in unirradiated tungsten, which can obscure the yield point and elastic-plastic transition. Alternatively, a different method of polishing may be chosen to eliminate the presence of pop-ins; electropolishing was used to achieve a smooth surface for HR-EBSD, but this can be mitigated by using tips of radii greater than 10 µm.

This work has contributed to the understanding of the strain-rate sensitivity, hardening and stress-strain response of neutron-irradiation tungsten, which is significant given that existing studies have generally examined ion-irradiated material due to the safety implications and handling restrictions on radioactive materials inventory. The strong alignment of the results in this study with those reported in literature demonstrates the value in using ion irradiation as a means to simulate the effects of neutron irradiation on materials. It is also important to note that the fastest spherical indentation strain rate used in this work was 3.2×10^{-3} s^{-1}, but strain rates of up to 3 s^{-1} for disruptions and 8 s^{-1} for ELMs are predicted inside the DEMO reactor.[5] The limitations in indenter control are evident at the fastest strain rate through the increased margins of error in the ISS, and thus yield stress, results. Further work can be conducted at strain rates beyond this using dedicated high strain rate nanoindentation testing. Nonetheless, the strain-rate sensitivity of neutron-irradiated tungsten reported here provides an indication of material performance during routine operation, as well as a body of data for extrapolation to extreme strain rates.

7.2 Deformation Mechanisms

The morphology of the pile-up produced by the spherical nanoindentation was examined using AFM. As previously observed in literature, there was a four-fold symmetry in the pile-up pattern, with distinct lobes along the $\langle 110 \rangle$ directions, corresponding to the four $\langle 111 \rangle$ slip directions on the $\{110\}$ planes and confirming that the deformation process is dominated by activity on the primary slip

system $\{110\}\langle 111\rangle$. The pile-up is a direct result of the localised flow of material occurring from slip in microscopic volumes only, indicating reduced strain hardening potential on a local microscopic level; strain hardening is clearly observed on a global level, as evidenced by indentation stress-strain curves reported in this work. The dislocation channelling in SX was evidenced by channels of depressed material extending up to 30 µm from the lobes, whilst slip steps were observed in NISX. Previous observations in other neutron-irradiated bcc metals further imply that cleared dislocation channels were formed in the neutron-irradiated sample.

The maximum residual indentation depth was found to unintentionally increase as a function of strain rate, which may be attributed to the challenging nanoindenter control needed to achieve the strain-controlled spherical nanoindentation method (described further in Sections 3.4.1 and 4.3.3). Even after normalisation, there is a positive trend in pile-up height with strain rate, but it is unlikely that this would be the case if total indenter depth was constant.

There was a significant increase in pile-up height in NISX compared to SX across all strain rates, despite the change in indent depth. Similar values were obtained for the average increase in pile-up height after irradiation across all strain rates using both 5 µm and 10 µm tips (173% and 179% respectively). Given the difference in the total indentation displacement across strain rates due to the nanoindentation method, the surface heights were normalised as a function of maximum residual indent depth. This normalised height measured with the 5 µm radius tip showed a generally positive trend with an increase in strain rate from slow to fast, ranging from 8.6% to 11.8% for SX, and 21.8% to 36.5% for NISX; in the 10 µm tip case, normalised heights ranging from ~13.1% to ~14.0% for SX, and ~24.2% to ~27.3% for NISX, were obtained as the strain rate increased. These results indicate a clear increase in pile-up post-irradiation. A similar phenomenon was previously described for self-ion irradiated tungsten and helium-implanted tungsten examined using HR-EBSD, cross-sectional TEM and CPFE modelling, and was reported to result from the constrained plastic zone beneath the indenter due to radiation-induced defects.

To assess the underlying plastic deformation which caused the change in surface morphology, HR-EBSD maps were collected for the 5 µm and analysed using XEBSD cross-correlation code, enabling the quantification of microstructural-level information, such as the elastic strains, lattice rotations and GNDs surrounding the indents.[93,94,95]

The magnitude of lattice strains and rotations around the indent in the XY plane (on the order of 10^{-3}) showed a clear increase with irradiation, whilst a slight increase observed with strain rate. In both samples, the GND density concentrated around the four lobe regions was ~10^{14} m^{-2} whilst the background GND density was ~10^{13} m^{-2}; however, in SX, the areas of increased density were confined to the edges of the lobes, whereas in NISX, the higher density zones cover the entirety of the lobes.

The strain, rotation, and GND results reported here were remarkably similar to those reported for spherical indents in unirradiated and self-ion irradiated W irradiated to 1 dpa. The increase in the magnitude of the strains and rotations, in addition to GND density and pile-up height examined through experiments show that the deformation behaviour is indeed modified following irradiation. However, the effect of the localisation of strains observed in literature representative of a confined plastic zone in the irradiated sample was not clearly observed.

Nonetheless, the consistency in deformation mechanisms observed between this study and the self-ion irradiated studies above highlight the credibility of using ion irradiation to mimic the damage effects of neutron irradiation, despite the creation of what is essentially a composite system in ion-irradiated samples.

Whilst the deformation behaviour was successfully probed after neutron-irradiation, examining indents performed to the same total indenter displacement would provide an objective and reliable means of comparing deformation behaviour across strain rates. The micromechanical testing and characterisation methods used here have positive implications for the study of the performance of materials in a reactor environment through small test volumes.

7.3 Validation of Results by CPFE Modelling

Strain-gradient CPFE modelling was used to simulate the spherical nanoindentation experiment using a 5 µm radius tip at the fast and medium strain rates in SX and NISX with the aim to achieve enhanced understanding of the changes induced by irradiation and strain-rate observed through experiments. The model employs a physically-based slip law coupled with GND evolution as a strain hardening mechanism. The critical resolved shear stress and geometric hardening factor are fitted to the load-displacement curves, indentation pile-up, in-plane shear strains and GND density measured. In the neutron-irradiated model, an initial value of solute hardening from defects and saturation value of slip strain are fitted to the data from NISX.

Strong quantitative agreement was sought for CPFE-predicted load-displacement curves and pile-up heights across the fast and medium strain rates in both materials. Similarly, the four-fold symmetry in the pile-up morphology produced by the model correlated well with the experiments and wider literature. In addition, the absolute values and distribution of GND density predicted by the model were very similar to those measured through experiments.

The correct order of magnitude in the negative and positive in-plane shear strains was also predicted. Interestingly, the strain fields corresponding to the lobe regions in SX were modelled to be more narrow and elongated in comparison to NISX, whereas the strain fields were more compact and rounded in the irradiated material. This change in localisation is not as clear to observe in the HR-EBSD maps, but is consistent with CPFE modelling and HR-EBSD in self-ion irradiated tungsten. The reduction in the length of the lobes is a clear indicator of the constricted plastic zone following irradiation.

There was a subtle increase in the size of the strain fields and regions of increased density around the indents increased with strain rate for both materials. However, as discussed previously, drawing comparisons between strain rates when the final displacement depth is different is not particularly meaningful. This is supported by further CPFE modelling undertaken to investigate the effect of strain

rate on pile-up behaviour using a consistent final indenter displacement, and thus strain, for the 5 µm radius tip, given that the increase in total displacement with strain rate was an artifact of the rate-controlled spherical nanoindentation method. Notably, for a fixed displacement, the pile-up produced at different strain rates should be constant, although a slightly higher peak load was achieved at the faster strain rate. This indicates that the effect of strain rate on dislocation mobility is minimal and the increased pile-up as a function of strain rate previously seen in the nanoindentation experiments was indeed a result of the rate-controlled method, which gave artificially rise to greater total displacement depths at faster strain rates. It is possible an increase in the magnitude of strains and rotations could be expected with increased strain rate, whereas GND density would be unlikely to change as it is a function of the tip geometry. Nonetheless, the CPFE predictions calculated with a set of parameters fitted to experimental results was successful in capturing the observed increase in pile-up height and constrained plastic zone in NISX with remarkable agreement, and provided clarity on the subtle rate effects.

A further systematic study to optimise the effect of each fitting parameter on the deformation behaviour produced would be beneficial. One of the challenges of CPFE modelling of this kind is the ability to use the unirradiated material's CRSS, geometric hardening factors, radiation solute hardening, saturation strain or the slip law, to fit the data. Thus, parameters which lead to strong agreement with one measure of deformation behaviour at a given condition may not match well with a different strain rate.

The CPFE modelling undertaken in this work successfully reproduced the experimental results observed, and provided clarity on the effect of strain rate on pile-up. The results confirm the presence of a constrained plastic zone in irradiated tungsten, which causes an increase in the pile-up height observed around nanoindents after irradiation, but shows negligible change with strain rate. This is relevant to the testing of mechanical properties using nanoindentation, given that pile-up can cause artifacts such as an overestimation of the hardness and elastic modulus.

7.4 Conclusions

The work in this thesis successfully investigated the effect of strain rate and neutron damage on tungsten in a fusion reactor by using a combination of micromechanical testing and characterisation techniques.

This study delivered insights into the strain hardening and yield behaviour of unirradiated and neutron-irradiated single crystal tungsten and their respective dependence on strain rate. Notably, the strain-rate sensitivity increased after irradiation, which is also reflected in a greater upwards shift in the indentation stress-strain curves with applied strain rate in comparison to the unirradiated sample. The work hardening phenomena, or lack thereof in the unirradiated sample, reflected the complex, defect-riddled microstructure of Re-Os precipitates, voids and dislocation loops in the neutron-irradiated tungsten.

Characterisation of the surface pile-up morphology, strain localisation and GND density revealed a significant increase in the pile-up height in the four lobes around the indent after irradiation, indicating the presence of a constrained plastic zone influenced by radiation-induced defects and increased material flow towards the surface.

Due to the challenging control in the rate-controlled spherical nanoindentation method, the total indenter displacement increased with strain rate, despite being programmed to end at the same total strain. The pile-up heights normalised as a function of maximum residual indentation depth showed a positive correlation with strain rate, but further refinement of the method would allow a more accurate and reliable method of characterising the deformation behaviour produced from nanoindentation. CPFE modelling results confirmed an increase in the pile-up height after irradiation due to the confinement of the plastic zone in the irradiated sample, but shows negligible change with strain rate.

Importantly, CPFE modelling using a set of parameters fitted to the experimental results successfully captured the observed increase in pile-up height and constraint of the plastic zone with remarkable agreement, and provided clarity on the subtle rate effects.

The strong similarities between the radiation-induced hardening and deformation in this study compared to those observed from ion-irradiated samples gives credence to ion irradiation in emulating the effects of neutron irradiation, despite the different damage mechanisms produced. Furthermore, this work emphasises the benefits of using micromechanical testing and reduced volumes of active material to study strain rate effects in potential plasma-facing components and indicate the quality of material performance in a fusion reactor.

7.5 Future Work

There is an opportunity to build on the work outlined in this thesis through completion of the following activities:

- In order to reduce the effect of pop-ins on the ISS curves and better explore the elastic-plastic transition, a larger spherical tip could be used. This would also enable a higher success rate through avoiding difficulties in PID control, thus improving statistical robustness.
- Further work to refine the spherical indentation method (and indenter control) to enable tests to finish at same depth regardless of strain rate would allow a better comparison of pile-up as well as the ratio of volume above the surface to the volume below the surface.
- Conducting strain rate testing at the higher strain rates expected during ELMs and plasma disruption events. High strain rate nanoindentation based on piezoelectric displacement actuation has been reported to achieve up to ballistic strain rates (10^3 s^{-1});[134] alternatively, increasing the data acquisition rate of a conventional nanoindenter into the 100 kHz range can also increase achievable strain rates by several orders of magnitude.[135]

- Undertaking CPFE simulations at further strain rates (only the fast and medium strain rates were simulated in this work). Comparison between three strain rates would enable further refinement and validation of α and β in Equation 6.4 to reflect the thermal activation and increased pinning probability in the neutron-irradiated sample (i.e. through reduction of V).
- Conducting additional CPFE simulations with a 10 μm radius tip to validate the comparisons drawn between the two tip sizes experimentally.
- Performing transmission Kikuchi diffraction (TKD) to analyse the cross-section of the plastic zone around spherical nanoindents and provide understanding beyond examination of the surface using HR-EBSD (e.g. to observe dislocation networks and plastic zone suppression post-irradiation).

References

1. Chu, S. & Majumdar, A. Opportunities and challenges for a sustainable energy future. *Nature* **488**, 294–303 (2012).

2. Lee, R. The Outlook for Population Growth. *Science* **333**, 569–573 (2011).

3. Ward, D. J., Cook, I., Lechon, Y. & Saez, R. The economic viability of fusion power. *Fusion Eng. Des.* **75**, 1221–1227 (2005).

4. Zinkle, S. J. Fusion materials science: Overview of challenges and recent progress. *Phys. Plasmas* **12**, 058101 (2005).

5. Uytdenhouwen, I., Massaut, V., Linke, J. & Oost, G. Van. Plasma Wall Interaction Phenomena on Tungsten Armour Materials for Fusion Applications. *IYNC 2008 Int. Youth Nucl. Congr. 2008, Interlaken (Switzerland), 21-26 Sep 2008* **Paper XYZ**, (2008).

6. Steiner, D. The Nuclear Performance of Fusion Reactor Blankets. *Nucl. Appl. Technol.* **9**, 83–92 (1970).

7. Zinkle, S. J. & Busby, J. T. Structural materials for fission & fusion energy. *Mater. Today* **12**, 12–19 (2009).

8. Zinkle, S. J. & Snead, L. L. Designing Radiation Resistance in Materials for Fusion Energy. *Annu. Rev. Mater. Res* **44**, 241–267 (2014).

9. Post, R. F. & Ribe, F. L. Fusion Reactors as Future Energy Sources. *Science* **162**, 661–675 (1974).

10. Boozer, A. H. Physics of magnetically confined plasmas. *Rev. Mod. Phys.* **76**, 1071–1141 (2004).

11. Frank W. Clinard, J. Abstract: First wall materials problems in fusion reactors. *J. Vac. Sci. Technol.* **12**, 510 (1975).

12. Bolt, H. *et al.* Materials for the plasma-facing components of fusion reactors. *J. Nucl. Mater.* **329**–**333**, 66–73 (2004).

13. ITER. http://www.iter.org. Available at: https://www.iter.org/iter-image-galleries/technical. (Accessed: 10th August 2019)

14. Merola, M. *et al.* ITER plasma-facing components. *Fusion Eng. Des.* **85**, 2312–2322 (2010).

15. Thomser, C. *et al.* Plasma facing materials for the jet iter-like wall. *Fusion Sci. Technol.* **62**, 1–8 (2012).

16. Abernethy, R. G. Predicting the performance of tungsten in a fusion environment: a literature review. *Energy Mater.* **33**, 388–399 (2016).

17. Roth, J. *et al.* Recent analysis of key plasma wall interactions issues for ITER. *J. Nucl. Mater.* **390**–**391**, 1–9 (2009).

18. Giannattasio, A., Yao, Z., Tarleton, E. & Roberts, S. G. Brittle-ductile transitions in

polycrystalline tungsten. *Philos. Mag.* **90**, 3947–3959 (2010).

19. Rieth, M. *et al.* Recent progress in research on tungsten materials for nuclear fusion applications in Europe. *J. Nucl. Mater.* **432**, 482–500 (2013).

20. Budaev, V. P. Results of high heat flux tests of tungsten divertor targets under plasma heat loads expected in ITER and tokamaks (Review). *Phys. At. Nucl.* **79**, 1137–1162 (2016).

21. Federici, G. *et al.* Plasma – material interactions in current tokamaks and their implications for next step fusion reactors. *Nucl. Fusion* **41**, 1967–2137 (2001).

22. Victoria, M., Baluc, N. & Spätig, P. Structural materials for fusion reactors. *Nucl. Fusion* **41**, 1047–1053 (2002).

23. Gilbert, M. R. & Sublet, J.-C. Neutron-induced transmutation effects in W and W-alloys in a fusion environment. *Nucl. Fusion* **51**, 043005 (2011).

24. Duffy, D. M. Fusion power: a challenge for materials science. *Philos. Trans. A. Math. Phys. Eng. Sci.* **368**, 3315–28 (2010).

25. Gilbert, M. Introduction to nuclear inventory simulations: Activation, transmutation & primary damage. CDT presentation [21/11/17]

26. Schiller, P. The 14 MeV neutron source for the development of fusion reactor materials. *Fusion Eng. Des.* **30**, 191–197 (1995).

27. Marian, J. *et al.* Recent advances in modeling and simulation of the exposure and response of tungsten to fusion energy conditions. *Nucl. Fusion* **57**, 092008 (2017).

28. Armstrong, D. E. J., Yi, X., Marquis, E. A. & Roberts, S. G. Hardening of self ion implanted tungsten and tungsten 5-wt % rhenium. *J. Nucl. Mater.* **432**, 428–436 (2013).

29. Nelson, R. S., Mazey, D. J. & Hudson, J. A. The use of ion accelerators to simulate fast neutron-induced. *J. Nucl. Mater.* **37**, 1–12 (1970).

30. Lloyd, M. J. *et al.* Decoration of voids with rhenium and osmium transmutation products in neutron irradiated single crystal tungsten. *Scr. Mater.* **173**, 96–100 (2019).

31. Hosemann, P., Shin, C. & Kiener, D. Small scale mechanical testing of irradiated materials. *J. Mater. Res.* **30**, 1231–1245 (2015).

32. Armstrong, D. E. J. *et al.* Small-scale characterisation of irradiated nuclear materials: Part II nanoindentation and micro-cantilever testing of ion irradiated nuclear materials. *J. Nucl. Mater.* **462**, 374–381 (2015).

33. Poon, B., Rittel, D. & Ravichandran, G. An analysis of nanoindentation in linearly elastic solids. *Int. J. Solids Struct.* **45**, 6018–6033 (2008).

34. Oliver, W. C. & Pharr, G. M. An improved technique for determining hardness and elastic modulus using load and displacement sensing indentation experiments. *J. Mater. Res.* **7**, 1564–1583 (1992).

35. Pethica, J. B. & Oliver, W. C. Mechanical properties of nanometer volumes of material: use of

the elastic response of small area indentations. in *Thin films: stresses and mechanical properties, Materials Research Society Symposium Proceedings, vol. 130 Pittsburgh, PA* 13–23 (1989).

36. Li, X. & Bhushan, B. A review of nanoindentation continuous stiffness measurement technique and its applications. *Mater. Charact.* **48**, 11–36 (2002).

37. Field, J. S. & Swain, M. V. A simple predictive model for spherical indentation. *J. Mater. Res.* **8**, 297–306 (1993).

38. Cordill, M. J. *et al.* The Nano-Jackhammer effect in probing near-surface mechanical properties. *Int. J. Plast.* **25**, 2045–2058 (2009).

39. Siu, K. W. & Ngan, A. H. W. Oscillation-induced softening in copper and molybdenum from nano- to micro-length scales. *Mater. Sci. Eng. A* **572**, 56–64 (2013).

40. Leitner, A., Maier-Kiener, V. & Kiener, D. Dynamic nanoindentation testing: is there an influence on a material's hardness? *Mater. Res. Lett.* **5**, 486–493 (2017).

41. Lucas, B. N. & Oliver, W. C. Indentation power-law creep of high-purity indium. *Metall. Mater. Trans. A* **30**, 601–610 (1999).

42. Durst, K. & Maier, V. Dynamic nanoindentation testing for studying thermally activated processes from single to nanocrystalline metals. *Curr. Opin. Solid State Mater. Sci.* **19**, 340–353 (2015).

43. Zhu, T. T., Bushby, A. J. & Dunstan, D. J. Size effect in the initiation of plasticity for ceramics in nanoindentation. *J. Mech. Phys. Solids* **56**, 1170–1185 (2008).

44. Alcalá, J., Barone, A. C. & Anglada, M. The influence of plastic hardening on surface deformation modes around Vickers and spherical indents. *Acta Mater.* **48**, 3451–3464 (2000).

45. Hardie, C. D., Roberts, S. G. & Bushby, A. J. Understanding the effects of ion irradiation using nanoindentation techniques. *J. Nucl. Mater.* **462**, 391–401 (2015).

46. Wang, Y., Raabe, D., Klüber, C. & Roters, F. Orientation dependence of nanoindentation pile-up patterns and of nanoindentation microtextures in copper single crystals. *Acta Mater.* **52**, 2229–2238 (2004).

47. Nix, W. D. & Gao, H. Indentation size effects in crystalline materials: A law for strain gradient plasticity. *J. Mech. Phys. Solids* **46**, 411–425 (1998).

48. Brinell, J. Sätt att bestämma kroppars hårdhet jämte några tillämpningar of detsamma. *Tek. Tidskr.* **5**, 69–87 (1900).

49. Meyer, E. Untersuchungen über härteprüfung und härte brinell methoden. *Des Vereines Dtsch. Ingenieure* **52**, 645–654 (1908).

50. Tabor D. *The Hardness of Metals*. (Clarendon Press, 1951).

51. Hertz, H. On the contact of rigid elastic solids. *J. fur die Reine und Angew. Math.* **92**, 156–171 (1882).

52. Harding, J. W. & Sneddon, I. N. The elastic stresses produced by the indentation of the plane surface of a semi-infinite elastic solid by a rigid punch. *Math. Proc. Cambridge Philos. Soc.* **41**, 16–26 (1945).

53. Bushby, A. J. & Jennett, N. M. Determining the area function of spherical indenters for nanoindentation. *Mater. Res. Soc. Symp.* **649**, 1–6 (2000).

54. Bushby, A. J. Nano-Indentation Using Spherical Indenters. *Nondestruct. Test. Eval.* **17**, 213–234 (2001).

55. Kalidindi, S. R. & Pathak, S. Determination of the effective zero-point and the extraction of spherical nanoindentation stress-strain curves. *Acta Mater.* **56**, 3523–3532 (2008).

56. Pathak, S. & Kalidindi, S. R. Spherical nanoindentation stress-strain curves. *Mater. Sci. Eng. R Reports* **91**, 1–36 (2015).

57. Weaver, J. S. *et al.* Quantifying the mechanical effects of He, W and He + W ion irradiation on tungsten with spherical nanoindentation. *J. Mater. Sci.* **53**, 5296–5316 (2018).

58. Leitner, A., Maier-Kiener, V. & Kiener, D. Essential refinements of spherical nanoindentation protocols for the reliable determination of mechanical flow curves. *Mater. Des.* **146**, 69–80 (2018).

59. Lim, Y. Y., Bushby, A. J. & Chaudhri, M. M. Nano and macro indentation studies of polycrystalline copper using spherical indenters. *Mater. Res. Soc. Symp. - Proc.* **522**, 145–150 (1998).

60. Durst, K., Göken, M. & Pharr, G. M. Indentation size effect in spherical and pyramidal indentations. *J. Phys. D. Appl. Phys.* **41**, 074005 (2008).

61. Swadener, J. G., George, E. P. & Pharr, G. M. The correlation of the indentation size effect measured with indenters of various shapes. *J. Mech. Phys. Solids* **50**, 681–694 (2002).

62. Pharr, G. M., Herbert, E. G. & Gao, Y. The indentation size effect: A critical examination of experimental observations and mechanistic interpretations. *Annu. Rev. Mater. Res.* **40**, 271–292 (2010).

63. Cackett, A. J., Hardie, C. D., Lim, J. J. H. & Tarleton, E. Spherical indentation of copper: Crystal plasticity vs experiment. *Materialia* **7**, 100368 (2019).

64. Bushby, A. J., Roberts, S. G. & Hardie, C. D. Nanoindentation investigation of ion-irradiated Fe-Cr alloys using spherical indenters. *J. Mater. Res.* **27**, 85–90 (2012).

65. Das, S., Yu, H., Tarleton, E. & Hofmann, F. Orientation-dependent indentation response of helium-implanted tungsten. *Appl. Phys. Lett.* **114**, 221905 (2019).

66. Greer, J. R. & De Hosson, J. T. M. Plasticity in small-sized metallic systems: Intrinsic versus extrinsic size effect. *Prog. Mater. Sci.* **56**, 654–724 (2011).

67. Schneider, A. S. *et al.* Correlation between critical temperature and strength of small-scale bcc pillars. *Phys. Rev. Lett.* **103**, 1–4 (2009).

68. Wei, Q., Cheng, S., Ramesh, K. T. & Ma, E. Effect of nanocrystalline and ultrafine grain sizes on

the strain rate sensitivity and activation volume: Fcc versus bcc metals. *Mater. Sci. Eng. A* **381**, 71–79 (2004).

69. Wei, Q. Strain rate effects in the ultrafine grain and nanocrystalline regimes-influence on some constitutive responses. *J. Mater. Sci.* **42**, 1709–1727 (2007).

70. Maier, V., Schunk, C., Göken, M. & Durst, K. Microstructure-dependent deformation behaviour of bcc-metals - Indentation size effect and strain rate sensitivity. *Philos. Mag.* **95**, 1766–1779 (2015).

71. Maier, V., Hohenwarter, A., Pippan, R. & Kiener, D. Thermally activated deformation processes in body-centered cubic Cr - How microstructure influences strain-rate sensitivity. *Scr. Mater.* **106**, 42–45 (2015).

72. Brunner, D. Comparison of flow-stress measurements on high-purity tungsten single crystals with the kink-pair theory. *Materials Transactions, JIM* **41**, 152–160 (2000).

73. Hart, E. W. Theory of the tensile test. *Acta Metall.* **15**, 351–355 (1967).

74. Maier, V. *et al.* Nanoindentation strain-rate jump tests for determining the local strain-rate sensitivity in nanocrystalline Ni and ultrafine-grained Al. *J. Mater. Res.* **26**, 1421–1430 (2011).

75. Feldner, P., Merle, B. & Göken, M. Determination of the strain-rate sensitivity of ultrafine-grained materials by spherical nanoindentation. *J. Mater. Res.* **32**, 1466–1473 (2017).

76. Abernethy, R. G. *et al.* Effects of neutron irradiation on the brittle to ductile transition in single crystal tungsten. *J. Nucl. Mater.* **527**, 151799 (2019).

77. Dunne, F. P. E. & Petrinic, N. *Introduction to Computational Plasticity*. (Oxford University Press, 2004).

78. Dunne, F. P. E. Fatigue crack nucleation: Mechanistic modelling across the length scales. *Curr. Opin. Solid State Mater. Sci.* **18**, 170–179 (2014).

79. Kartal, M. E., Kiwanuka, R. & Dunne, F. P. E. Determination of sub-surface stresses at inclusions in single crystal superalloy using HR-EBSD, crystal plasticity and inverse eigenstrain analysis. *Int. J. Solids Struct.* **67**–**68**, 27–39 (2015).

80. Beck, C. E. *et al.* Correcting for contact area changes in nanoindentation using surface acoustic waves. *Scr. Mater.* **128**, 83–86 (2017).

81. Armstrong, D. E. J., Wilkinson, A. J. & Roberts, S. G. Mechanical properties of ion-implanted tungsten-5 wt% tantalum. *Phys. Scr. T* 14076 (2011).

82. Pharr, G., Tsui, T., Bolshakov, A. & Oliver, W. Effects of Residual Stress on the Measurement of Hardness and Elastic Modulus using Nanoindentation. *Mater. Res. Soc. Symp. - Proc.* **338**, 127 (1994).

83. Kuksenko, V., Roberts, S. & Tarleton, E. The hardness and modulus of polycrystalline beryllium from nano-indentation. *Int. J. Plast.* **116**, 62–80 (2019).

84. Das, S., Yu, H., Tarleton, E. & Hofmann, F. Hardening and Strain Localisation in Helium-Ion-Implanted Tungsten. *arXiv* (2018).

85. Dunne, F. P. E., Rugg, D. & Walker, A. Lengthscale-dependent, elastically anisotropic, physically-based hcp crystal plasticity: Application to cold-dwell fatigue in Ti alloys. *Int. J. Plast.* **23**, 1061–1083 (2007).

86. Dunne, F. P. E., Kiwanuka, R. & Wilkinson, A. J. Crystal plasticity analysis of micro-deformation, lattice rotation and geometrically necessary dislocation density. *Proc. R. Soc. A Math. Phys. Eng. Sci.* **468**, 2509–2531 (2012).

87. Das, S. *et al.* The effect of helium implantation on the deformation behaviour of tungsten: X-ray micro-diffraction and nanoindentation. *Scr. Mater.* **146**, 335–339 (2018).

88. Das, S., Yu, H., Mizohata, K., Tarleton, E. & Hofmann, F. Modified deformation behaviour of self-ion irradiated tungsten: A combined nano-indentation, HR-EBSD and crystal plasticity study. *Int. J. Plast.* **135**, 102817 (2020).

89. Klimenkov, M. *et al.* Effect of neutron irradiation on the microstructure of tungsten. *Nucl. Mater. Energy* **9**, 480–483 (2016).

90. Huang, C. H., Gilbert, M. R. & Marian, J. Simulating irradiation hardening in tungsten under fast neutron irradiation including Re production by transmutation. *J. Nucl. Mater.* **499**, 204–215 (2018).

91. Binnig, G., Quate, C. & Gerber, C. Atomic Force Microscope. *Phys. Rev. Lett.* **56**, 930 (1986).

92. Cackett, A. J. Size effects in dislocation-mediated plasticity in copper alloys with different microstructural length-scales. (Queen Mary University of London, 2020).

93. Wilkinson, A. J., Meaden, G. & Dingley, D. J. High-resolution elastic strain measurement from electron backscatter diffraction patterns: New levels of sensitivity. *Ultramicroscopy* **106**, 307–313 (2006).

94. Britton, T. B. & Wilkinson, A. J. Measurement of residual elastic strain and lattice rotations with high resolution electron backscatter diffraction. *Ultramicroscopy* **111**, 1395–1404 (2011).

95. Britton, T. B. & Wilkinson, A. J. High resolution electron backscatter diffraction measurements of elastic strain variations in the presence of larger lattice rotations. *Ultramicroscopy* **114**, 82–95 (2012).

96. Lloyd, M. J., Haley, J., Jim, B. *et al.* Microstructural Evolution and Transmutation in Tungsten under Ion and Neutron Irradiation. *Materialia* **33**, 101991 (2024).

97. Gibson, J. S. K. L. Mechanical Behaviour of Irradiated Tungsten for Fusion Power (2015).

98. Syed Asif, S. A. & Pethica, J. B. Nanoindentation creep of single-crystal tungsten and gallium arsenide. *Philos. Mag. A* **76**, 1105–1118 (1997).

99. Levenberg, K. A Method for the Solution of Certain Non-Linear Problems in Least Squares. *Q. Appl. Math.* **2**, 164–168 (1944).

100. Marquardt, D. W. An Algorithm for Least-squares Estimation of Nonlinear Parameters. *J. Soc. Ind. Appl. Math.* **11**, (1963).

101. Moseson, A. J., Basu, S. & Barsoum, M. W. Determination of the effective zero point of contact for spherical nanoindentation. *J. Mater. Res.* **23**, 204–209 (2008).

102. Chang, C., Garrido, M. A., Ruiz-Hervias, J., Zhang, Z. & Zhang, L. Le. Representative Stress-Strain Curve by Spherical Indentation on Elastic-Plastic Materials. *Adv. Mater. Sci. Eng.* **2018**, (2018).

103. Hasenhuetl, E., Kasada, R., Zhang, Z., Yabuuchi, K. & Kimura, A. Ion-irradiation effect on strain rate sensitivity of nanoindentation hardness of W single crystal. *Mater. Trans.* **58**, 580–586 (2017).

104. Fukuda, M. *et al.* Neutron energy spectrum influence on irradiation hardening and microstructural development of tungsten. *J. Nucl. Mater.* **479**, 249–254 (2016).

105. Papadakis, D. *et al.* Neutron irradiation effects in different tungsten microstructures. *Phys. Scr.* **96**, (2021).

106. Tanno, T. *et al.* Effects of transmutation elements on neutron irradiation hardening of tungsten. *Mater. Trans.* **48**, 2399–2402 (2007).

107. Hu, X. *et al.* Irradiation hardening of pure tungsten exposed to neutron irradiation. *J. Nucl. Mater.* **480**, 235–243 (2016).

108. Hasegawa, A., Fukuda, M., Yabuuchi, K. & Nogami, S. Neutron irradiation effects on the microstructural development of tungsten and tungsten alloys. *J. Nucl. Mater.* **471**, 175–183 (2016).

109. Gilbert, M. R., Sublet, J.-C. & Forrest, R. A. Handbook of activation, transmutation, and radiation damage properties of the elements simulated using FISPACT-II & TENDL-2014. *CCFE-R* **(15)26**, 1–696 (2015).

110. Edmondson, P. D., Gault, B. & Gilbert, M. R. An atom probe tomography and inventory calculation examination of second phase precipitates in neutron irradiated single crystal tungsten. *Nucl. Fusion* **60**, 126013 (2020).

111. Hashimoto, N., Byun, T. S., Farrell, K. & Zinkle, S. J. Deformation microstructure of neutron-irradiated pure polycrystalline metals. *J. Nucl. Mater.* **329**–**333**, 947–952 (2004).

112. Rice, P. M. & Zinkle, S. J. Temperature dependence of microstructure in low dose neutron irradiated V-4Cr-4Ti. *J. Nucl. Mater.* 1414–1419 (1998).

113. Riding, M. Understanding Dislocation Structures in BCC Metals. (2020).

114. Sudharshan Phani, P., Johanns, K. E., George, E. P. & Pharr, G. M. A stochastic model for the size dependence of spherical indentation pop-in. *J. Mater. Res.* **28**, 2728–2739 (2013).

115. Shim, S., Bei, H., George, E. P. & Pharr, G. M. A different type of indentation size effect. *Scr. Mater.* **59**, 1095–1098 (2008).

116. Gröger, R., Bailey, A. G. & Vitek, V. Multiscale modeling of plastic deformation of molybdenum and tungsten: I. Atomistic studies of the core structure and glide of $1/2\langle 1\,1\,1\rangle$ screw dislocations at 0 K. *Acta Mater.* **56**, 5401–5411 (2008).

117. Chen, N. K. & Maddin, R. Slip planes and the energy of dislocations in a bodycentered cubic structure. *Acta Metall.* **2**, 49–51 (1954).

118. Srivastava, K., Gröger, R., Weygand, D. & Gumbsch, P. Dislocation motion in tungsten: Atomistic input to discrete dislocation simulations. *Int. J. Plast.* **47**, 126–142 (2013).

119. Wang, Y., Raabe, D., Klüber, C. & Roters, F. Orientation dependence of nanoindentation pile-up patterns and of nanoindentation microtextures in copper single crystals. *Acta Mater.* **52**, 2229–2238 (2004).

120. Yu, H. *et al.* New perspectives on collision cascade damage in self-ion irradiated tungsten from HR-EBSD and ECCI. *J. Nucl. Mater.* **554**, 153074 (2021).

121. Das, S., Yu, H., Tarleton, E. & Hofmann, F. Hardening and Strain Localisation in Helium-Ion-Implanted Tungsten. *Sci. Rep.* **9**, 1–14 (2019).

122. Voyiadjis, G. Z. & Abu Al-Rub, R. K. Thermodynamic based model for the evolution equation of the backstress in cyclic plasticity. *Int. J. Plast.* **19**, 2121–2147 (2003).

123. Das, S., Hofmann, F. & Tarleton, E. Consistent determination of geometrically necessary dislocation density from simulations and experiments. *Int. J. Plast.* **109**, 18–42 (2018).

124. Nye, J. F. Some geometrical relations in dislocated crystals. *Acta Metall.* **1**, 153–162 (1953).

125. Taylor, G. I. The mechanism of plastic deformation of crystals. Part II.—Comparison with observations. *Proc. R. Soc. London. Ser. A, Contain. Pap. a Math. Phys. Character* **145**, 388–404 (1934).

126. Featherston, F. H. & Neighbours, J. R. Elastic constants of tantalum, tungsten, and molybdenum. *Phys. Rev.* **130**, 1324–1333 (1963).

127. Bolef, D. I. & De Klerk, J. Elastic Constants of Single-Crystal Mo and W between 77° and 500°K. *J. Appl. Phys.* **33**, (1962).

128. Ayres, R. A., Shannette, G. W. & Stein, D. F. Elastic constants of tungsten−rhenium alloys from 77 to 298 °K. *J. Appl. Phys.* **46**, 1526–1530 (1975).

129. Klein, C. A. & Cardinale, G. F. Young's modulus and Poisson's ratio of CVD diamond. *Diam. Relat. Mater.* **2**, 918–923 (1993).

130. Dutta, B. N. & Dayal, B. Lattice Constants and Thermal Expansion of Palladium and Tungsten up to 878 °C by X-Ray Method. *Phys. Status Solidi* **3**, 2253–2259 (1963).

131. Sweeney, C. A. *et al.* The role of elastic anisotropy, length scale and crystallographic slip in fatigue crack nucleation. *J. Mech. Phys. Solids* **61**, 1224–1240 (2013).

132. Liang, Z. Y. & Pharr, G. M. Decoupling indentation size and strain rate effects during nanoindentation: A case study in tungsten. *J. Mech. Phys. Solids* **165**, 104935 (2022).

133. Gibson, J. S. K., Roberts, S. G. & Armstrong, D. E. J. High temperature indentation of helium-implanted tungsten. *Mater. Sci. Eng. A* **625**, 380–384 (2015).

134. Guillonneau, G. *et al.* Nanomechanical testing at high strain rates: New instrumentation for

nanoindentation and microcompression. *Mater. Des.* **148**, 39–48 (2018).

135. Phani, P. S. & Oliver, W. C. Ultra high strain rate nanoindentation testing. *Materials (Basel).* **10**, 663 (2017).

136. McCann, M. M. & Corcoran, S. G. Nanoindentation behavior of gold single crystals. in *Materials Research Society Symposium - Proceedings* **795**, 331–337 (2003).